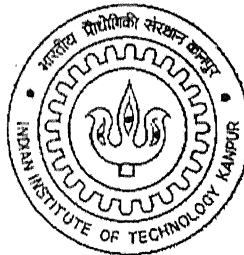


**Momentum and heat transfer from an asymmetrically confined  
circular cylinder in a plane channel**

A thesis submitted  
in partial fulfillment of the requirements  
for the degree of  
Master of Technology

by

**Srinivas Mettu**



to the

**Department of Chemical Engineering  
INDIAN INSTITUTE OF TECHNOLOGY  
KANPUR**  
May, 2005

TH  
CHZ/2005/101  
M 568 m

19 JUL 2005 / CHE  
श्रुतोत्तम कागीनाथ केनकर पुस्तकालय  
भारतीय प्रौद्योगिकी संस्थान कानपुर  
कालिका नं. 152181



A152181

# CERTIFICATE

It is certified that the work contained in the thesis entitled "*Momentum and heat transfer from an asymmetrically confined circular cylinder in a plane channel*" by **Srinivas Mettu**, has been carried out under my supervision and that this work has not been submitted elsewhere for a degree.



May, 2005

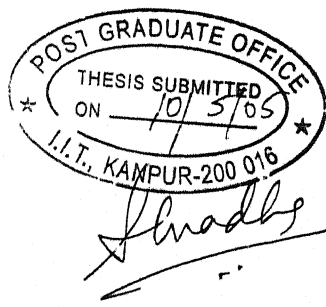
**Dr. Nishith Verma**

Associate Professor

Department of Chemical Engineering

Indian Institute of Technology

Kanpur



## ACKNOWLEDGEMENT

At the very beginning I would like to thank the authority of IIT Kanpur for providing high-class facilities and the ambience necessary to carry out research work. During the research work, my thesis guide Dr. N. Verma has helped me immensely with his ingenious ideas and valuable guidance. I am highly grateful to him for motivating and encouraging me during all the stages of my thesis work. By working under his aegis I have come to know the intricate details of research work. It was my privilege to have worked under him. I am also thankful to Prof. R. P. Chhabra for his kind co-operation and helpful suggestions.

I would like to specially acknowledge the support regarding CFD provided by Ramprakah, Nitin, Dhiman, Sunil Dhole and Nanda Kishore. I shall always cherish the sweet memories attached with my lab mates Sudhakar, Vivek, Ritesh, Kaushal, Nilesh, Shiva Kumar, Rupesh and Abhinandan. They have always helped to maintain a friendly atmosphere in our lab. More than this, they have always been a constant source of inspiration.

The time spent with Anji, Babai, Ravi, Ramana, Simha, Mallesh, Dinesh, Sameer, Akhi, Parimal, Satyam, Pramod, and Nageswara Rao has been a major recreation for me. The memories associated with them will surely be cherished forever. They were always there to give me moral support in every situation in my life here.

At the end I would like to convey my regards to my parents and all other family members for their endless love, encouragement and endurance during my stay at IIT Kanpur. Their silent presence behind my all achievements cannot be properly expressed.

Finally, I am grateful to the almighty for what I am today.

May, 2005

Srinivas Mettu

## ABSTRACT

The flow past a circular cylinder is a fundamentally important problem as it is a good approximation to a large number of problems encountered in engineering applications like heat exchanger tubes, instrumentation technology in Hot-wire anemometry, flow past dividers in polymer processing, piping installations. The fundamental nature of the flow has attracted many investigators who have carried out experimental and numerical investigations to characterize the flow using global parameters like; wake length, separation angle, drag coefficient, lift coefficient, Strouhal number and Nusselt number. Despite significant number of studies carried out over the years on the flow past a circular cylinder in unconfined domain, only few studies are available on the flow past a circular cylinder confined in a plane channel that is rather more appropriate in many practical situations. In addition, the transition of flow past an asymmetrically confined circular cylinder in a plane channel from steady to unsteady flow has not been characterized completely compared to the transition of the flow past a cylinder in unbounded domain.

In this study, the unsteady flow of an incompressible Newtonian fluid past a circular cylinder in unbounded and bounded domains was simulated using a commercially available flow modeling software, FLUENT (version 6.1), which utilizes a finite volume based numerical method to solve the equations of continuity, momentum and energy. In particular, three cases were studied; (i) unsteady momentum transfer from a circular cylinder in unbounded domain (ii) unsteady momentum and heat transfer from an asymmetrically confined circular cylinder in a plane channel, and (iii) three-dimensional transition in the wake of a circular cylinder. In the case of unsteady momentum transfer from a cylinder in unbounded domain, the transition of flow from steady to unsteady is studied with the aid of various momentum upwinding schemes. The important engineering parameters like total drag coefficient, Strouhal number were computed using various upwinding schemes in the range of  $Re$  from 50 to 1000 and compared with the published data wherever possible. In the case of unsteady momentum and heat transfer from an asymmetrically confined cylinder in a plane channel, the transition of the flow from steady to unsteady is characterized as a function of blockage

ratio ( $\beta$ , ratio of the diameter of the cylinder to the channel width) and gap ratio ( $\gamma$ ). The unsteady numerical simulations were carried out for the range of  $Re$  between 10 and 1000 and blockage ratio ( $\beta$ ) from 0.1 to 0.4 using the constant wall temperature boundary condition on the surface of the cylinder. The fluid considered was air with negligible property variation. The effect of blockage ratio ( $\beta$ ) and gap ratio ( $\gamma$ ) on the time averaged drag coefficient, lift coefficient, Strouhal number, and Nusselt number was studied. In the case of three-dimensional flow past a circular cylinder, the transition of the flow from 2-D to 3-D flow was studied.

The critical  $Re$  at which the flow transition takes place from steady to unsteady was found to increase with increase in blockage ratio ( $\beta$ ) for a symmetrically confined cylinder in a plane channel. For fixed blockage ratio, the critical  $Re$  was found to increase with decrease (cylinder moves closer to the wall) in the gap ratio. For fixed  $Re$  and blockage ratio, the time averaged drag coefficient and Strouhal number were found to increase with decrease in gap ratio. The increase in the drag coefficient was found to be more pronounced at low  $Re$ . The amplitude of the oscillations in the lift coefficient was found to increase in the negative direction as the cylinder moved closer to one of the confining walls. The reverse trend was observed when the cylinder was present sufficiently close to the cylinder in which case the amplitude of the oscillations in the lift coefficient increased in positive direction. The effect of increase in blockage ratio on the surface averaged Nusselt number was found to be negligible for blockage ratio below 0.3. The effect of decrease in gap ratio on the surface averaged Nusselt number was also found to be negligible. However, some distortion was found in the local Nusselt number distribution on the surface of the cylinder when the cylinder was present close to one of the confining walls. The transition of the flow past a circular cylinder from 2-D to 3-D was characterized using Strouhal-Reynolds number relation and normalized velocity profiles along the span of the cylinder.

## CONTENTS

	Page Number
<b>List of Figures</b>	i
<b>List of Tables</b>	iv
<b>Nomenclature</b>	vi
<b>1. Introduction.....</b>	1
<b>2. Literature review.....</b>	4
<b>3. Problem statement and formulation .....</b>	16
<b>4. Numerical methodology.....</b>	24
<b>5. Model validation.....</b>	28
<b>6. Results and discussion.....</b>	43
<b>7. Conclusions and scope for the future study.....</b>	106
<b>References</b>	
<b>Appendix</b>	

## LIST OF FIGURES

	Page numbers
3.1 Schematic for 2-D flow past a circular cylinder in unbounded domain.....	22
3.2 Schematic for 3-D flow past a circular cylinder in unbounded domain.....	22
3.3 Schematic for flow past an asymmetrically confined circular cylinder in a plane channel.....	23
5.1 Validation of $C_D$ for unconfined flow in the steady range ( $Re < 50$ ).....	37
5.2 Validation for $\overline{Nu}_w$ in unconfined flow ( $Pr = 0.7441, Re < 50$ ).....	38
5.3 Validation of $\overline{C}_D$ for unconfined flow in the unsteady range. ....	39
5.4 Validation of $St$ for unconfined flow in the unsteady range.....	40
5.5 Validation of $\overline{Nu}_w$ ( $Pr = 0.7441$ ) for $\gamma=1$ (symmetrical) for $\beta = 0.1$ .....	41
5.6 Validation of $\overline{Nu}_w$ ( $Pr = 0.7441$ ) for $\gamma=1$ (symmetrical) for $\beta = 0.2$ .....	42
6.1 Typical mesh configuration used to simulate flow past a circular cylinder in unbounded domain ( $R/r = 140$ ).....	68
6.2 Schematic of the rotation of the circular cylinder.....	69
6.3 $C_D$ and $C_L$ time histories for $Re = 100$ .....	70
6.4 $C_L$ time histories for $Re = 48$ and 50 for second order upwinding scheme.....	71
6.5 Streamline plots for $Re = 46, 48$ , and 50 for second order upwinding scheme....	72
6.6 $C_L$ time history for $Re = 50$ obtained from QUICK scheme.....	73
6.7 Streamline plots for $Re = 50$ at different time steps from QUICK scheme.....	74
6.8 $C_L$ time histories for $Re = 94, 96$ and 100 by first order upwinding scheme .....	75
6.9 $\overline{C}_D$ vs $Re$ calculated from various upwinding schemes.....	76
6.10 $St$ vs $Re$ calculated from various upwinding schemes.....	77
6.11 Typical mesh configuration used to simulate	

flow past a circular cylinder confined in a plane channel.....	78
6.12 Comparison of $Re_C$ and $St$ for various $\beta$ and $\gamma = 1$ (symmetrical).....	79
6.13 Variation of critical $Re$ with $\gamma$ for $\beta = 0.2$ .....	80
6.14 Variation of critical $Re$ with $\beta$ and $\gamma$ .....	81
6.15 Effect of blockage ratio ( $\beta$ ) on $\bar{C}_D$ for $\gamma = 1$ (symmetrical).....	82
6.16 Effect of blockage ratio ( $\beta$ ) on $St$ for $\gamma = 1$ (symmetrical).....	83
6.17 Snapshots of instantaneous vorticity contours at $Re = 200$ for various $\beta$ .....	84
6.18 $C_L$ - $C_D$ periodic trajectories during one period at $Re = 200$ for various $\beta$ and $\gamma = 1$ .....	85
6.19 $C_L$ - $C_D$ trajectory and $C_L$ and $C_D$ time history at $Re = 200$ for $\beta = 0.1$ and $\gamma = 1$ .....	86
6.20 Effect of blockage ratio ( $\beta$ ) on $\bar{Nu}_w$ for $\gamma = 1$ (symmetrical) .....	87
6.21 $C_D$ vs $Re$ as a function of $\beta$ and $\gamma$ .....	88
6.22 $C_{DP}$ vs $Re$ and $C_{DF}$ vs $Re$ as a function of $\gamma$ ( $\beta = 0.1$ and $0.2$ ).....	89
6.23 $C_{DP}$ vs $Re$ and $C_{DF}$ vs $Re$ as a function of $\gamma$ ( $\beta = 0.3$ and $0.4$ ).....	90
6.24 $St$ vs $Re$ as a function of $\beta$ and $\gamma$ .....	91
6.25 Snapshots of instantaneous vorticity contours at $Re = 200$ for various $\beta$ and $\gamma$ .....	92
6.26 $C_L$ - $C_D$ periodic trajectories at $Re = 200$ and $\beta = 0.1$ as a function of $\gamma$ .....	93
6.27 $C_L$ - $C_D$ periodic trajectories at $Re = 200$ and $\beta = 0.2$ as a function of $\gamma$ .....	94
6.28 $C_L$ - $C_D$ periodic trajectories at $Re = 200$ and $\beta = 0.3$ as a function of $\gamma$ .....	95

6.29 $C_L$ - $C_D$ periodic trajectories at $Re = 200$ and $\beta = 0.4$	
as a function of $\gamma$ .....	96
6.30 $\bar{C}_L$ vs $Re$ as a function of $\beta$ and $\gamma$ .....	97
6.31 Unsteady vorticity contours at $Re = 200$ and $\beta = 0.3$ .....	98
6.32 $\bar{Nu}_w$ vs $Re$ as a function of $\beta$ and $\gamma$ .....	99
6.33 Variation of local $Nu_w$ over the surface of the cylinder	
as a function of $\beta$ and $\gamma$ .....	100
6.34 Typical mesh configuration used to simulate	
3-D flow past a circular cylinder .....	101
6.35 $St$ - $Re$ curves for 2-D and 3-D simulations.....	102
6.36 Normalized velocity plots at $Re = 100$ along the span of	
the cylinder at 2d, 5d downstream locations .....	103
6.37 Normalized velocity plots at $Re = 200$ along the span of	
the cylinder at 2d, 5d downstream locations.....	104
6.38 Normalized velocity plots at $Re = 300$ along the span of	
the cylinder at 2d, 5d downstream locations .....	105

## LIST OF TABLES

	Page numbers
5.1 Comparison of $C_D$ values with the published data for the steady flow range .....	32
5.2 Comparison of $\overline{Nu}_w$ ( $Pr = 0.7441$ ) values with the published data for the steady flow range .....	32
5.3 Grid independence test using QUICK scheme for momentum upwinding.....	32
5.4 Comparison of $\overline{C}_D$ values with the published data for the unsteady flow range .....	33
5.5 Comparison of $C_L$ , $St$ values with the published data for the unsteady flow range.....	33
5.6 Comparison of $\overline{C}_D$ , $C_L$ , $St$ values with the experimental and simulation results.....	34
5.7 Comparison of $\overline{C}_D$ and $\overline{Nu}_w$ ( $Pr = 0.7441$ ) values for $\beta = 0.1$ .....	35
5.8 Comparison of $\overline{C}_D$ and $\overline{Nu}_w$ ( $Pr = 0.7441$ ) values for $\beta = 0.2$ .....	35
5.9 Comparison of $\overline{C}_D$ and $\overline{Nu}_w$ ( $Pr = 0.7441$ ) values for $\beta = 0.2$ and $\gamma = 0.375$ .....	36
6.1 The effect of disturbance (rotational speed) on $\overline{C}_D$ , $C_L$ , and $St$ at $Re = 100$ .....	56
6.2 Comparison of critical $Re$ observed from various upwinding schemes.....	56
6.3 Comparison of $\overline{C}_D$ calculated from different upwinding schemes .....	56
6.4 Comparison of $St$ calculated from different upwinding schemes .....	57
6.5 Comparison of $Re_C$ and $St$ values at various blockage ratios .....	57

6.6 Comparison of $Re_C$ values for various $\gamma$ for $\beta = 0.2$ .....	57
6.7 Variation of $Re_C$ with $\beta$ and $\gamma$ .....	58
6.8 Effect of blockage ratio ( $\beta$ ) on $\bar{C}_D$ for $\gamma = 1$ (symmetrical).....	58
6.9 Effect of blockage ratio ( $\beta$ ) on $St$ for $\gamma = 1$ (symmetrical).....	59
6.10 Effect of blockage ratio ( $\beta$ ) on $\bar{Nu}_w$ for $\gamma = 1$ (symmetrical).....	59
6.11 Effect of gap ratio ( $\gamma$ ) on $\bar{C}_D$ for $\beta = 0.1$ .....	60
6.12 Effect of gap ratio ( $\gamma$ ) on $\bar{C}_D$ for $\beta = 0.2$ .....	60
6.13 Effect of gap ratio ( $\gamma$ ) on $\bar{C}_D$ for $\beta = 0.3$ .....	61
6.14 Effect of gap ratio ( $\gamma$ ) on $\bar{C}_D$ for $\beta = 0.4$ .....	61
6.15 Effect of gap ratio ( $\gamma$ ) on $St$ for $\beta = 0.1$ .....	62
6.16 Effect of gap ratio ( $\gamma$ ) on $St$ for $\beta = 0.2$ .....	62
6.17 Effect of gap ratio ( $\gamma$ ) on $St$ for $\beta = 0.3$ .....	63
6.18 Effect of gap ratio ( $\gamma$ ) on $St$ for $\beta = 0.4$ .....	63
6.19 Effect of gap ratio ( $\gamma$ ) on $\bar{Nu}_w$ for $\beta = 0.1$ .....	64
6.20 Effect of gap ratio ( $\gamma$ ) on $\bar{Nu}_w$ for $\beta = 0.2$ .....	64
6.21 Effect of gap ratio ( $\gamma$ ) on $\bar{Nu}_w$ for $\beta = 0.3$ .....	65
6.22 Effect of gap ratio ( $\gamma$ ) on $\bar{Nu}_w$ for $\beta = 0.4$ .....	65
6.23 Grid independence test for 3-D flow past a cylinder in unbounded domain.....	66
6.24 $\bar{C}_D$ and $St$ for 3-D flow past a cylinder using GRID2.....	66
6.25 $\bar{C}_D$ and $St$ for 3-D flow past a cylinder obtained using coarser grid (133,000 cells).....	67

## NOMENCLATURE

$d, D$	Diameter of the cylinder, m
$C_D$	Total drag coefficient (dimensionless)
$\bar{C}_D$	Time averaged drag coefficient (dimensionless), Arithmetic average over 10 cycles
$C_{DF}$	Friction drag coefficient (dimensionless)
$C_{DP}$	Pressure drag coefficient (dimensionless)
$C_L$	Lift coefficient (dimensionless)
$f$	frequency of the oscillation in the lift coefficient, cycle/sec
$St$	Strouhal number, $\frac{fd}{U_\infty}$ or $\frac{fd}{\bar{u}_d}$
$\bar{t}$	$tU_\infty/d$ , Non-dimensional time unit
$Nu_w$	Local Nusselt number over the surface of the cylinder, (dimensionless)
$\bar{Nu}_w$	Average Nusselt number (dimensionless)
$F_D$	Total drag force per unit length of the cylinder, N
$F_L$	Total lift force per unit length of the cylinder, N
$W$	Width of the channel, m
$r$	Radius of the cylinder, m
$R_\infty$	Radius of the outer circular boundary, m
$Re$	Reynolds number, $\frac{dU_\infty\rho}{\mu}$ or $\frac{d\bar{u}_d\rho}{\mu}$
$Pr$	Prandtl number, $\hat{C}p\mu/k$
$Re_c$	Critical Reynolds number
$U_\infty$	Uniform inlet velocity, m/s
$\bar{u}_d$	Average velocity over the cylinder, m/s
$U_{max}$	Maximum velocity in the channel, m/s
$V_x$	x-direction velocity, m/s
$V_y$	y-direction velocity, m/s
$V_z$	z-direction velocity, m/s
$T$	Temperature, $^0\text{K}$
$T_w$	Temperature at the cylinder wall, $^0\text{K}$
$T_\infty$	Free stream temperature, $^0\text{K}$

$\hat{C}_p$  Heat capacity, J/Kg.  $^0\text{K}$

K Thermal conductivity, W/m.  $^0\text{K}$

**Greek Symbols**

$\beta$  Blockage ratio,  $d/H$

$\Delta$  The minimum distance from surface of the cylinder to the nearest wall, m

$\gamma$  Gap ratio,  $\Delta/(H/2-d/2)$

$\mu$  Viscosity of the fluid, Pa.s

$\rho$  Density of the fluid, kg/m<sup>3</sup>

$\theta$  Angle measured from the rear stagnation point, degree

# CHAPTER 1

## INTRODUCTION

### 1.1 Introduction

The flow past a circular cylinder is a classical problem in fluid mechanics as it is a good approximation to a large number of problems encountered in engineering applications like heat exchanger tubes, instrumentation technology in Hot-wire anemometry, flow past dividers in polymer processing, piping installations, electric transmission lines, suspension bridges, and offshore cylindrical drilling rigs. The governing equations of motion, namely Navier-Stokes equations are highly nonlinear in nature and the exact analytical solutions are still not available except few approximate analytical solutions (Stokes, 1851) for flow past a sphere at low Reynolds numbers. Therefore, it has been subjected to numerous experimental as well as numerical investigations [1-55] to understand the dynamics of the flow by calculating the global parameters that characterize the flow, such as wake length, separation angle, drag and lift coefficients, Strouhal number ( $St$ ), and Nusselt number ( $Nu_w$ ).

The flow past a circular cylinder may be divided into different regimes depending on  $Re$ . For  $Re \sim 1$ , the flow is fore and oft symmetric, divides at front stagnation point and reunites smoothly behind the cylinder. As  $Re$  increases above 5, the flow separation takes places on the downstream side with formation of two symmetric vortices, which are stable and remain attached to the cylinder. In this regime, symmetric vortices behind the cylinder elongate farther as  $Re$  increases. Around  $Re = 47$ , a new flow pattern develops in which the oscillation of vortices gives rise to the well-known Von karman vortex street. The discrete vortices are regularly placed behind the cylinder, with the non-dimensional number  $St$  characterizing the frequency of oscillation of the vortices. In this regime the frequency of oscillation ( $St$ ) increases as  $Re$  increases. This regime continues up to  $Re = 180$  at which complex three-dimensional flow structure develops [51].

A large amount of wealthy information [1-55] on the flow past a cylinder has been accumulated over the years because of the ideal nature of the flow, which can be applied to many industrially important applications with little modifications. The above-mentioned flow regimes that exist for the flow past a cylinder in unbounded domain may

change considerably [23] for the flow past a cylinder confined symmetrically in a plane channel. From the literature survey it is evident that the flow past a cylinder confined in a plane channel has received relatively much lesser attention [55,23,39]. Chen et al. [23] have studied the transition of the flow past a circular cylinder confined symmetrically in a plane channel from steady to unsteady using finite element numerical simulations. It was concluded from their study that the flow dynamics differ greatly when the cylinder is confined in a plane channel because of the presence the stationary walls and the stability of the flow is enhanced as the walls approach closer to the cylinder. The critical  $Re$  at which the flow transition takes place from steady to unsteady was found to increase with increasing the blockage ratio ( $\beta$ ).

The flow past a cylinder confined in a plane channel is also affected considerably depending on the situation whether the cylinder is confined symmetrically in the plane channel or confined asymmetrically [24]. In the case of the cylinder confined asymmetrically, the flow dynamics changes significantly because of the presence of the wall close to the cylinder. To ascertain the effect of asymmetry on the transition of the flow, Zovatto and Pedrizzetti [24] have numerically studied the loss of stability of the flow past a circular cylinder confined asymmetrically in a rectangular plane channel for a blockage ratio of 0.2 using a finite element numerical method based on vorticity-streamfunction formulations. It was concluded from their study that the stability is enhanced as the cylinder approaches one of the confining walls. The critical  $Re$  at which the flow transition takes place was found to increase as the cylinder approaches one of the confining walls. The main limitation of their study was that the definition of the asymmetry parameter ( $\gamma$ , gap ratio) was such that it was applicable to only one blockage ratio, which does not allow the comparison of the results with the results for the other blockage ratios. In our study we have defined an asymmetry parameter, gap ratio ( $\gamma$ ), such that it takes a value of 1 when the cylinder is confined symmetrically in the plane channel, whereas it takes a value of zero when the cylinder touches one of the confining walls irrespective of the blockage ratio ( $\beta$ ). We have studied the transition of the flow past a cylinder confined asymmetrically in a plane channel over a wide range of blockage ratio ( $\beta$ ). More importantly, we have also studied the effect of the asymmetric

confinement on the heat transfer characteristics from the cylinder that is more relevant to practical applications.

## 1.2 Objectives

The objectives of this thesis work are as follows:

- 1) Comparison of various momentum upwinding schemes with respect to the transition of the flow past a circular cylinder in unbounded domain from steady to unsteady and the comparison of global parameters like drag coefficient and *Strouhal Number* obtained using these upwinding schemes.
- 2) Characterization of the transition of the flow past a cylinder confined in a plane channel from steady to unsteady as a function of asymmetry ( $\gamma$ , gap ratio) and blockage ratio ( $\beta$ ).
- 3) Study of the effect of asymmetry and blockage ratio on drag coefficient, lift coefficient, *Strouhal number*, and Nusselt number over the range of  $Re$  from 10 to 1000.
- 4) Study of the transition of the flow past a circular cylinder in unbounded domain from 2-D to 3-D.

## CHAPTER 2

### LITERATURE REVIEW

#### 2.1. Steady flow past a circular cylinder:

The first attempt to solve the Navier-Stokes equations for the problem of steady, incompressible, Newtonian flow past a circular cylinder in unconfined domain dates back to Thom [1], who solved the problem by integrating the equations of motions under steady state conditions, for  $Re = 10$  and  $20$ . Subsequent numerical investigations were carried out by Kawaguti [2] and Apelt [3] to solve the same problem for  $Re = 40$ . The time dependent simulations were first carried out by Payne [4] for  $Re = 40, 100$  and the drag values, stream function, iso-vorticity plots were presented. But this study had many limitations. For example, a fixed time step was used in the computations and numerical computations were carried out for a shorter time at which standing vortex was not fully developed. More important, the grid sensitivity analysis was not carried out. In his time dependent numerical simulations, Ingham [5] varied time step as well as mesh sizes to determine the optimum values for  $Re = 100$ . Finer mesh size used by Ingham [5] gave better results compared to Payne's [4]. It was concluded that the mesh size used by Payne [4] was coarse; hence the steady state values were not obtained.

Kawaguti and Jain [6] carried out a systematic numerical study of the flow of an incompressible, Newtonian fluid past a circular cylinder in unconfined domain for  $Re = 1$  to  $100$ . The steady state solutions for  $Re = 10, 20, 30, 40, 50$  were obtained as the limit of unsteady solutions. The radius of the outer circular boundary was fixed at 112 radii of the cylinder to have insignificant effect of boundaries on solutions. The streamlines and iso-vorticity lines were presented for each  $Re$ . The length of standing vortex, separation angle, total drag, surface pressure and vorticity distribution were plotted as functions of time. However, the solutions for  $Re = 60$  and  $100$  did not reach steady state and it was evident from the plot of the length of standing vortex against time for  $Re = 60$  and  $100$  that the shape didn't correspond to steady state flow. It was also opined that the appearance of the region of positive (negative) vorticity just outside the wake could have been caused either by the coarse mesh used by them or by the occurrence of instability

resulting in von Karman vortex street, which appears in the flows at  $Re > 40$ . But the main limitation of their study was that the grid independence test was not carried out.

Hamielec and Rall [7] have extended the study of Kawaguti and Jain [6] up to  $Re = 500$  with a finer mesh size in radial and angular directions. The radius of the outer circular boundary was also varied to study the effect on drag values. The surface vorticity distribution, pressure distribution, streamlines, iso-vorticity lines, drag values and length of standing vortex were presented for various  $Re$  up to 500. It was concluded that the length of standing vortex predicted by Kawaguti and Jain was too high owing to the coarse mesh size used by them. However, the numerical results for  $Re = 500$  were not reliable as the steady state solution was not obtained. In agreement to the observations of Kawaguti and Jain [6], Thoman and Szewczyk [8], the authors have noted that at such a high  $Re$ , one experimentally observes vortex shedding and von Karman vortex street, which are the characteristics of unsteadiness in the flow. In theoretical studies, vortex shedding can only be observed by introducing a small asymmetric disturbance to the flow by various techniques such as, introducing artificial vorticity into the flow field for a small period of time, rotating the cylinder for a short period of time, and making the location of the cylinder slightly eccentric between the two planes.

Takami and Keller have [9] have carried out numerical simulation of the steady, two-dimensional flow past a circular cylinder in infinite domain for  $Re = 1$  to 60. The radius of the outer circular boundary was varied. The boundary conditions at the outer cylinder were applied by matching Imai's [10] asymptotic solution. Streamlines, vorticity plots, drag values and length of standing vortex were presented up to  $Re = 60$ . The linear dependence of length of standing vortex was observed up to  $Re = 60$ .

Dennis and Chang [11] extended the study of Takami and Keller [8] to  $Re = 100$ . The main objective of their study was to produce reliable data on the steady flow past a circular cylinder with respect to the growth of standing vortex and to gain an information on the nature of the theoretical flow limit as  $Re \rightarrow \infty$ . Finite-difference solutions of equations of motion were obtained for  $Re = 5$  to 100 for half domain with symmetric boundary condition. The length of the standing vortex followed linear dependence on  $Re$  with the flow separation taking place at a critical  $Re$  of 7. Streamlines, wake length, drag, angle of separation, surface pressure distribution, vorticity distribution were presented for

$Re = 5, 7, 10, 20, 40, 70, 100$ . Although variation in these parameters with  $Re$  was found to be consistent in their study, the nature of these parameters could not be established with certainty as  $Re \rightarrow \infty$ .

Fornberg [12] has numerically studied the steady viscous flow past a circular cylinder in unconfined domain for  $Re$  from 20 to 300. He has proposed a new technique for the boundary condition at a large distance from the cylinder and an iterative method to eliminate the numerical difficulties encountered in the simulation of flows at  $Re > 100$ . The streamlines, surface pressure distribution, vorticity distribution, separation point, wake length and drag values were presented. The shortening of the wake region with vorticity convected into interior was observed at high  $Re > 260$ . Far away from the cylinder, a simple boundary condition of normal derivatives equated to zero for  $Re < 40$  and a mixed boundary condition for higher  $Re$  gave better results.

D'Alessio and Dennis [13] have proposed a vorticity model for viscous flow past a circular cylinder that is consistent with the boundary layer theory for large  $Re$  and with the asymptotic solution at a large distance from the cylinder for low  $Re$ . Drag values were presented for  $Re = 5, 20, 40$  and  $100$  and were in good agreement with the results of Dennis and Chang [11] and Fornberg [12].

Coutanceau and Bourd [14] have carried out experimental investigation to determine the main feature in the wake of a circular cylinder in uniform cross flow in the range of  $Re$  from 5 to 40 for various blockage ratios  $\lambda$  (ratio of the diameter of the cylinder to the channel) by flow visualization technique. Velocity distribution in the wake of the cylinder, length of the standing vortex, separation angle were plotted against  $Re$  for various blockage ratios ( $\lambda$ ). The length of standing vortex and separation angle were found to decrease with increase in blockage ratio. The upper limit of  $Re$  at which twin vortices are stable and adhere to the cylinder was determined to be 39.5.

Recently, Chakraborty et al. [55] have extensively studied the effect of walls on steady, two-dimensional flow past a circular cylinder confined symmetrically in a plane channel by numerical simulations for  $Re$  between 0.1 and 200 and for blockage ratios ( $\lambda$ ) between 0.05 and 0.65. Total drag, pressure drag, friction drag, ratio of pressure drag to friction drag, the length of recirculation zone and separation angle were plotted against  $Re$  for various blockage ratios. For a fixed value of  $Re$ , total drag was found to increase

with the blockage ratio and for a fixed blockage ratio, drag decreased with increase in  $Re$ . Pressure drag and friction drag followed the trend of total drag where as their ratio increased with increase in  $Re$  for a fixed blockage ratio. The length of recirculation zone and separation angle found to decrease with increase in blockage ratio.

## 2.2. Unsteady flow past a circular cylinder:

The flow past a circular cylinder may be divided into different regimes depending on  $Re$ . For  $Re \sim 1$ , the flow is fore and aft symmetric, divides at front stagnation point and reunites smoothly behind the cylinder. As  $Re$  increases above 5, the flow separation takes places on the downstream side with formation of two symmetric vortices, which are stable and remain attached to the cylinder. In this regime, symmetric vortices behind the cylinder elongate farther as  $Re$  increases. Around  $Re = 47$ , a new flow pattern develops in which the oscillation of vortices gives rise to the well-known Von karman vortex street. The discrete vortices are regularly placed behind the cylinder, with the non-dimensional number  $St$  characterizing the frequency of oscillation of the vortices. In this regime the frequency of oscillation ( $St$ ) increases as  $Re$  increases. This regime continues up to  $Re = 180$  at which complex three-dimensional flow structure develops [51].

Many numerical investigations have been carried out to simulate the unsteady flow past a circular cylinder. The time dependent numerical simulation of the Navier-Stokes equations for the unsteady flow past a circular cylinder in cross flow was first carried out by Payne [4] for  $Re = 40$  and 100, followed by Ingham [5] for  $Re = 100$ . The evolution of flow properties like drag and length of the recirculation zone with time was presented.

Collins and Dennis [15] have numerically studied the flow past an impulsively started circular cylinder by integrating the time dependent Navier-Stokes equations for  $Re = 40, 100, 200$  and 500. The development of various flow properties, namely the length of the recirculation zone, the surface vorticity distribution and separation angle with the time was presented. For  $Re < 100$ , the integration was carried out until the solution reached steady state. For  $Re > 100$ , the integration was terminated well before the solution reached steady state due to the convergence failure. The time at which the integration procedure failed to converge decreased with increase in  $Re$ . This is consistent

with the fact that as  $Re$  increases the transition from steady flow to unsteady flow takes place at much earlier times.

Patel [16] has presented the semi-analytical solutions for the flow past an impulsively started circular cylinder for  $Re = 60, 100, 200, 500, 550$  and  $600$ . A set of coupled parabolic differential equations was obtained by substituting the stream function and vorticity expanded in the finite Fourier series in the Navier-Stokes equations. These equations were then solved numerically using the finite difference method. The growth of the recirculation zone, evolution of drag and surface vorticity distribution was presented for each  $Re$ . For the range  $Re$  investigated in this study, calculations never reached steady state and the length of the wake continued to grow with the appearance of the secondary vortex on the surface of the cylinder for  $Re = 500, 550$ , and  $600$ .

The main limitation of all the above-mentioned numerical simulations was that it was assumed that the flow reached steady state after a long time or the solutions were presented for short times at which flow remained steady. But in the flow at  $Re > 40$ , one experimentally observes Von Karman vortex street which is a characteristic of unsteadiness of the flow. None of the above mentioned authors simulated the vortex shedding from the cylinder for  $Re > 40$ .

Braza et al. [17] have solved the time dependent Navier-Stokes equations for the flow past a circular cylinder in unconfined domain by a finite volume second order accurate scheme and an alternating direction implicit procedure for  $Re = 100, 200$  and  $1000$ . The radius of the outer circular boundary was taken sufficiently large to simulate unbounded flow. They have shown that the flow reaches steady state symmetric pattern after a shorter or longer establishment period even at  $Re = 1000$ , also observed by Martinez (1979) for  $Re = 100$  and  $200$ , attributed to the fact that in case of numerical simulations the destabilizing factors like non-uniform inlet conditions, irregularity of the boundary conditions, vibrations and surface roughness that are present in experimental conditions are absent as the boundary conditions and initial condition are symmetric which lead to the steady symmetric solution of the Navier-Stokes equations. That is why the authors have used a perturbation method to generate vortex shedding from cylinder, which consists of the rotation of the circular cylinder in clockwise direction followed by rotation in anticlockwise direction for about a short period of time and then keeping the

cylinder stationary for the rest of the calculations. The global characteristics of the flow such as the mean drag, evolution of the lift coefficient with time, and mean  $St$  were presented. The oscillation of the pressure and viscous drag was found to be in phase with the oscillation of the total drag and the mean drag for unsteady flow was higher than that for the steady flow. The frequency of the oscillation of stagnation, separation and reattachment angle was in phase with the lift coefficient oscillations while the pressure coefficient was found to oscillate with twice the frequency of lift coefficient oscillations due to the simultaneous contribution of both the alternating vortices. It was shown from their study that the secondary eddies appear in the vicinity of each primary eddy above  $Re = 200$  and have significant presence in the near wake at  $Re = 1000$ .

Jackson [18] has studied the onset of periodic vortex shedding from bluff bodies of various shapes using finite element numerical simulations for two-dimensional laminar flow. Time dependent numerical simulations were not performed but the eigenvalue of the Jacobian matrix that characterizes the transition from steady to periodic flow was calculated by solving the extended systems of equations for locating the symmetry breaking Hopf bifurcation, which is the characteristic of the onset of vortex shedding. The solutions of these equations gave  $St$  and the critical  $Re$  at which the flow became periodic. The critical  $Re$  for the flow past a circular cylinder was determined to be  $\sim 46$  and it was found to be in good agreement with the experimental studies [19,20] as well as with the time dependent numerical simulations [8,21]. The critical  $Re$  for the flow past a flat plate, ellipse and prism shaped bodies was also presented as functions of the angle of orientation with flow. The critical  $Re$  was found to increase with increase in the angle between the minor axis and flow for an ellipse and with increase in the angle of orientation of the flat plate with flow.

Franke et al. [22] have solved the two-dimensional, unsteady Navier-Stokes equations for the flow past a circular as well as square cylinder using a third order accurate discretization scheme QUICK for the range of  $Re \leq 5000$  for the circular cylinder case and  $Re \leq 300$  for the square cylinder case. The main goal of their study was to examine the development of the vortex shedding from the cylinder as the flow velocity was increased from zero to free stream value. In their study flow velocity was increased from zero to the free stream value following a sine function. No disturbance was

introduced to obtain vortex shedding. The vortex shedding was automatically triggered by round-off errors and numerical diffusion. The drag values were in good agreement with the calculations of Braza et al [17] for  $Re$  up to 300. The deviation at higher  $Re$  was attributed to the beginning of the stochastic turbulent fluctuations.

Chen et al. [23] have studied the stability of the flow past a circular cylinder confined symmetrically in a plane channel using numerical simulations. Steady flow past the circular cylinder was perturbed slightly by the rotation of the circular cylinder for a short period of time. The time dependent motion following the rotation was examined to determine the critical  $Re$  at which the perturbation amplified leading to unsteady flow. The critical  $Re$  based on the diameter of the cylinder for a blockage ratio ( $d/H$ ) of 0.2 was found to be 69. Numerical bifurcation studies, similar to those carried out by Jackson [], were carried to determine the critical  $Re$  for various blockage ratios ranging from 0.1 to 0.7 by the calculation of the eigenvalues of the Jacobian matrix of the flow equation. It was showed that stability is lost through a symmetry breaking Hopf bifurcation. The critical  $Re$  was found to increase with increase in blockage up to 0.5 and decrease with the blockage ratio from 0.5 to 0.7.

Zovatto and Pedrizzetti [24] have numerically studied the loss of stability of the flow past a circular cylinder confined asymmetrically in a rectangular plane channel for a blockage ratio of 0.2 using a finite element numerical method based on vorticity-streamfunction formulations. Flow was assumed to start impulsively and at the inlet a parabolic velocity profile was specified. The critical  $Re$  at which the flow became periodic was found to increase as the cylinder approached one of the two confining walls i.e. the vortex shedding from the cylinder was suppressed when the cylinder was closer to one of the walls. When the cylinder was placed symmetrically between the plane walls the wake resembled the unbounded flow with the symmetric wake. However, when the cylinder was closer to one of the walls the wake was asymmetric with a reduced wake vorticity on the side of the wall and elongated wake vorticity on the other side. The cylinder behaved like a surface mounted obstacle when it was very close to the wall. For a fixed  $Re$ , the drag coefficient based on the diameter of the cylinder and the non-dimensional time period of the oscillations was found to increase with the decrease in the gap between the cylinder and the wall. It was concluded that the transition from steady to

unsteady flow is delayed as the cylinder approaches one of the confining walls resulting in the stability of the flow.

### 2.3 Laminar forced convection from a cylinder in cross flow

The heat transfer from a cylinder is of practical significance in Hot-wire anemometry which is a measuring technique widely used in experimental fluid mechanics to obtain information on velocity field. The correlation between heat loss from the wire probe and the velocity of the fluid helps in determining the flow field. It is an indirect measurement technique, which requires calibration against the known flow field.

Many experimental and numerical investigations have been carried out on momentum and heat transfer from a circular cylinder with respect to Hot-wire anemometry. Dennis et al. [25] have carried out numerical study for the heat transfer from a circular cylinder at constant temperature in a steady stream of viscous, incompressible fluid in unconfined domain in the range of  $Re$  from 0.01 to 40 with the assumption of constant fluid properties. The authors have determined the variation of  $\overline{Nu}$  with  $Re$  and compared the values with the experimental results of Collis and Williams [26]. The numerical results were in good agreement with the experimental results. They have also determined the variation of local  $Nu$  over the surface of the cylinder for the range of  $Re$  from 1 to 40.

To resolve the discrepancy between the data of hotwire anemometers and the empirical laws, Hua et al. [27] have theoretically analyzed the heat transfer from a constant temperature circular cylinder in cross flow. The authors assumed two regions: a stationary fluid region close to the cylinder and potential flow region far away from the cylinder. The authors theoretically calculated the heat transfer coefficient for airflow over the cylinder in the range of  $Re$  from 0.01 to  $9 \times 10^5$  and compared the values with the experimental data of Collis and Williams [26] and Cole and Roshko [28]. The results were in good agreement with the experimental data only in the range of  $0.1 < Re < 3 \times 10^4$ . The deviation at higher  $Re$  was attributed to the presence of turbulent boundary layer on the surface of the cylinder and the deviation at lower  $Re$  to the natural convection effects.

Karniadakis [29] has studied the unsteady, forced convection heat transfer from an isolated cylinder up to  $Re = 200$  by numerical simulation of the Navier-Stokes and

energy equations using spectral element method. Simulations were carried out for constant heat flux and constant temperature case with the flow started impulsively. The variation of the length of recirculation zone,  $St$ ,  $\overline{Nu}$ ,  $C_D$  with  $Re$  and the variation of local  $Nu$  over the surface of the cylinder were presented.

Figueiredo et al. [30] have studied the external forced convection from an isothermal circular cylinder, placed at various heights above a plane surface in the range of  $Re = 14 \times 10^3$  to  $40 \times 10^3$ . They have presented the results for the distribution of pressure coefficient around the cylinder, the variation of drag and lift coefficients, the distribution of local  $Nu$  around the cylinder and the variation of  $\overline{Nu}$  with  $Re$  for various cylinder to plate distances (H). It was concluded that the presence of a plane boundary introduces an asymmetry on the pressure and local heat transfer distribution around the cylinder. Both drag and  $Nu$  decrease with decreasing cylinder to plate distance, and the influence of the presence of the wall on the values of drag and  $Nu$  was significant only when  $H/D < 0.4$ .

Shin et al. [31] have studied the steady forced convection heat transfer from a circular cylinder in unconfined domain to propose a unified correlation that is valid for heat transfer from hot cylinder to cold fluid and hot fluid to cold cylinder for  $Re \leq 40$ . They have presented the results for the variation of  $\overline{Nu}$  with  $Re$  for various temperature loadings ( $T_w = 900-300$  K and  $T_a = 200-300$  K) for cold as well as hot cylinder. The variation of fluid properties significantly affected the heat transfer rate to or from the cylinder. As the difference between  $T_w$  and  $T_a$  magnifies, wide scatter of  $Nu$  as a function of  $Re$  is observed due to the property variations. They have also presented a unified correlation for  $Nu$  as a function of  $T_w/T_a$  and verified the results for various cylinder diameters and various free stream velocities.

Lange et al. [32] have studied momentum and heat transfer from a heated cylinder in unconfined domain in the range of  $Re = 0.0001$  to 200 for temperature loadings ( $T_w/T_a$ ) of 1.003-1.5. In this study, in view of very low  $Re$ , the diameters of the cylinder and temperature difference were chosen so as to neglect viscous dissipation and natural convection effects. The results for the variation of  $Nu$ ,  $St$  and  $C_D$  with  $Re$ , with the properties of the fluid evaluated at  $T_w$ ,  $T_f$  and  $T_\infty$  were presented. Drag was found to increase with the increase in temperature loading ( $T_w/T_\infty$ ) with the fluid properties

evaluated at free steam temperature. The increase in drag was found to be significant at lower  $Re$ . When the fluid properties were evaluated at cylinder wall temperature ( $T_w$ ) the increase in drag was found to be significant only when  $Re > 0.1$ . The effect of temperature loading on  $St$  was found to be insignificant. In a later study by Shi et al. [33] has suggested that indeed there is an effect on temperature loading and property variation on  $St$ . The transient density term that was neglected in the previous study of Lange et al [32] was included and the effect of temperature loading, density variation, viscosity variation on  $Nu$ ,  $C_D$ , and  $St$  were presented for  $Re$  from 0.001 to 175. The effect of density and viscosity variation with temperature on  $Nu$ ,  $C_D$ , and  $St$  was found to be significant with more contribution coming from viscosity variation. The density variation showed an apposite effect in steady and unsteady flows and the effect of property variation was significant only at low  $Re \leq 10$ . The separate characteristic temperatures for momentum and heat transfer were identified.

Lange et al. [34] have extended their study to investigate the effect of the presence of wall on heat transfer from the probe of Hot-wire anemometer. In this study the range of  $Re$  used is 0.001-0.1. To simulate the flow conditions near wall, Couette flow velocity distribution is specified at the inlet. The top boundary (wall) was kept at a large distance so as to have no effect on the heat transfer from cylinder. On the bottom boundary (wall closer to cylinder), two types of boundary conditions were specified: a highly conducting wall and an insulating wall, to study the effect of the presence of conducting and non-conducting wall on the heat loss from cylinder. Wall distances (H/D) between 10 and 300 are considered. In the case of highly conducting wall the temperature gradients were high due to the proximity of highly conducting wall. Hence there was an increase in  $Nu$  as the cylinder approached wall. In the case of non-conducting wall, there was a reduction of heat transfer from the cylinder to the wall due to the suppression of diffusive flux. Hence there was a decrease in  $Nu$ .

Shi et al. [35] have studied the effect of thermal conductivity ( $K$ ) of the wall and the shear rate on the heat loss from the cylinder for various wall distances. They have concluded that the presence of wall significantly affects heat transfer rate even when the thermal conductivity of the wall is very low. The wall effect becomes insignificant above  $H/D = 5$ . However, the effect of shear rate becomes significant.

Nakamura et al. [36] have studied the variation of  $Nu$  with flow regimes behind the circular cylinder experimentally. The authors have presented correlations for  $\overline{Nu}$  and  $Nu$  at the rear stagnation point for different flow regimes behind the cylinder: laminar shedding regime ( $Re < 150$ ), three dimensional flow regime ( $300 < Re < 1500$ ) and shear layer transition region ( $3 \times 10^3 < Re < 15 \times 10^3$ ).  $Nu$ , (at rear stagnation point) followed the trend of base suction pressure coefficient, which depends on the flow conditions behind the cylinder. The exponent of  $Re$  in the correlation for mean Nusselt number for three dimensional flow regime was lower than that for the other regimes. This is in accordance with the decrease in local  $Nu$  at rear stagnation point.

Sanitijai et al. [37] have carried out experimental investigation on heat transfer from a circular cylinder to air and ethylene glycol/water mixtures in the range of  $2 \times 10^3 < Re < 9 \times 10^4$  and  $2 \times 10^3 < Pr < 9 \times 10^4$ . The authors have considered flow regimes behind the cylinder and the contribution of heat transfer from front and rear parts of the cylinder separately as the flow structure is different for the two regions. They have concluded from their study that the three regions;  $0^\circ < \theta < 85^\circ$  (growth of laminar boundary layer),  $85^\circ < \theta < 135^\circ$  (reattachment of free shear layer),  $135^\circ < \theta < 180^\circ$  (the periodic vortices), contribute separately to the overall heat transfer from the cylinder. The heat transfer variation in the region of  $135^\circ < \theta < 180^\circ$  also depends on the flow regime behind the cylinder. The authors have presented correlations for the local and overall heat transfer coefficients.

Ahmed and Yovanovich [38] have obtained approximate analytical solutions for forced convection heat transfer from circular cylinders, flat plates and spheres in cross flow. They have proposed a method to predict heat transfer that is obtained by linearization of energy equation and then transforming the linearized energy equation into transient heat conduction equation, which has analytical solutions. The analytical solutions were presented in closed form for wide range of  $Re$  and  $Pr$  and results were in good agreement with the previous experimental results and analytical solutions.

Similarly, Khan et al. [39] have investigated the effect of blockage ratio on fluid flow and heat transfer from a circular cylinder confined in a plane channel for isothermal and isoflux boundary conditions using analytical approach. Correlations were presented for drag coefficient as a function of blockage ratio and  $Re$ , and for heat transfer

coefficient as a function of  $Re$ ,  $Pr$  and blockage ratio. Separate correlations were presented for isothermal and isoflux boundary conditions.  $Nu$  and drag were found to increase with increase in blockage ratio and  $Nu$  for isoflux boundary condition was found to be higher than  $Nu$  for isothermal boundary condition for all blockage ratios.

In light of the above review, it may be concluded that there exist few studies in the literature for the momentum transfer from an asymmetrically confined circular cylinder [24] and heat transfer from a symmetrically confined cylinder [39] in a plane channel. There have been no studies in the literature regarding the heat transfer from an asymmetrically confined cylinder in a plane channel. Therefore, to fill the existing gap, we have studied in the present work the momentum and heat transfer from an asymmetrically confined circular cylinder in a plane channel using FLUENT 6.1.

## CHAPTER 3

### PROBLEM STATEMENT AND FORMULATION

#### 3.1 Two-dimensional iso-thermal flow past a circular cylinder in unbounded domain:

Consider the unsteady 2-D isothermal flow of an incompressible Newtonian fluid past a circular cylinder in unbounded domain, as shown schematically in Figure 3.1. The geometry for 2-D flow in unbounded domain consists of a circular cylinder of radius  $r$ , placed in a circular outer boundary of radius  $R_\infty$ , where  $R_\infty/r = 140$ . The radius of outer circular boundary ( $R_\infty$ ) is taken to be large enough to ensure that the effect of boundaries on the inner cylinder wall is negligible. The left half of the outer circular boundary is taken as velocity inlet and the right half as the outflow.

The objectives of this 2-D study are: (a) to study the transition of flow past a cylinder from steady to unsteady flow, characterized by Von karman vortex street, with the aid of various upwinding schemes available in FLUENT, and (b) to determine the critical  $Re$  at which the flow becomes unsteady using each of the upwinding schemes.

#### 3.2 Three-dimensional iso-thermal flow past a circular cylinder in unbounded domain:

The geometry taken to simulate 3-D isothermal flow past a circular cylinder in unbounded domain, as shown schematically in Figure 3.2, is a rectangular brick of dimensions  $28d$ ,  $16d$  and  $2.25d$  in  $x$ ,  $y$  and  $z$ -directions, respectively, where  $d$  is the diameter of the cylinder. The cylinder is located at  $10d$  and  $18d$  from the inlet and outlet, respectively. The fluid enters at the plane  $ABCD$  with a uniform velocity  $U_\infty$  and leaves at the plane  $EFGH$ .

The main objective of this 3-D study is to examine the transition of flow past a cylinder from 2-D unsteady to 3-D unsteady flow, characterized by the dislocation of alternating vortices i.e. the bending of vortices in  $z$ -direction. The study of heat transfer effects is excluded in 2-D and 3-D study.

### 3.3 Non-isothermal flow past a circular cylinder confined in a plane channel:

In the case of non-isothermal flow past a circular cylinder confined in a plane channel, as shown schematically in Figure 3.3, two plane walls separated by a distance  $H$  confine a circular cylinder of diameter  $d$  whose position is defined by gap ratio,  $\gamma$ , defined as  $\Delta/(H/2-D/2)$  where  $\Delta$  is the minimum distance from the surface of the cylinder to the nearest wall. The value of  $\gamma$  is equal to 1 when the cylinder is placed symmetrically between the plane walls and is equal to zero when the cylinder touches one of the walls. The cylinder is located at  $15d$  and  $40d$  from the inlet and outlet, respectively. The length of the cylinder in  $z$ -direction is assumed to be long enough to have insignificant end effects, implying that there is no flow in  $z$ -direction and no flow variables depend upon  $z$ -coordinate. The fluid (Air,  $Pr = 0.7441$ ) at a temperature of  $T_\infty$  enters at the velocity inlet boundary  $AC$  with a parabolic velocity profile  $U = U_{max} (1-(y/H/2)^2)$  and leaves at the outflow boundary  $BD$ . The confining walls are at free stream temperature ( $T_\infty$ ) whereas the cylinder is at a temperature of  $T_w$ . The effect of variation in density and viscosity is neglected owing to the small temperature difference ( $T_w - T_\infty = 2^\circ K$ ) used in the study.

In this study,  $H$  and  $\gamma$  are varied to study the wall effects on momentum and heat transfer from the cylinder at a constant wall temperature. With respect to momentum transfer, the transition of flow past a cylinder in plane channel from 2-D steady to 2-D unsteady flow is studied. The critical  $Re$  at which the flow becomes unsteady resulting in periodic vortex shedding is also determined for various blockage ratios ( $\beta = d/H$ ) and  $\gamma$ . In addition to this, the effect of  $\beta$  and  $\gamma$  on drag coefficient and  $St$  is studied. With respect to heat transfer from the cylinder, the effects of  $\beta$  and  $\gamma$  on  $\overline{Nu}_w$  are determined.

### 3.4 Governing Equations

A Cartesian coordinate system is chosen. The velocity components in  $x$ ,  $y$  and  $z$  directions are  $V_x$ ,  $V_y$  and  $V_z$  respectively. The velocity components in  $x$ -,  $y$ -,  $z$ -directions for 2-D flow are

$V_x = V_x(x, y)$ ,  $V_y = V_y(x, y)$  and  $V_z = 0$  and the velocity components for 3-D flow are given as

$V_x = V_x(x, y, z)$ ,  $V_y = V_y(x, y, z)$  and  $V_z = V_z(x, y, z)$ .

Under these conditions the continuity equation for an incompressible fluid in 3-D is given as

$$\frac{\partial V_x}{\partial x} + \frac{\partial V_y}{\partial y} + \frac{\partial V_z}{\partial z} = 0 \quad (3.1)$$

and, the corresponding x-, y- and z-components of the Navier-Stokes equations (for constant  $\rho$  and  $\mu$ ) are written as:

$$\rho \left( \frac{\partial V_x}{\partial t} + V_x \frac{\partial V_x}{\partial x} + V_y \frac{\partial V_x}{\partial y} + V_z \frac{\partial V_x}{\partial z} \right) = -\frac{\partial p}{\partial x} + \mu \left( \frac{\partial^2 V_x}{\partial x^2} + \frac{\partial^2 V_x}{\partial y^2} + \frac{\partial^2 V_x}{\partial z^2} \right) \quad (3.2)$$

$$\rho \left( \frac{\partial V_y}{\partial t} + V_x \frac{\partial V_y}{\partial x} + V_y \frac{\partial V_y}{\partial y} + V_z \frac{\partial V_y}{\partial z} \right) = -\frac{\partial p}{\partial y} + \mu \left( \frac{\partial^2 V_y}{\partial x^2} + \frac{\partial^2 V_y}{\partial y^2} + \frac{\partial^2 V_y}{\partial z^2} \right) \quad (3.3)$$

$$\rho \left( \frac{\partial V_z}{\partial t} + V_x \frac{\partial V_z}{\partial x} + V_y \frac{\partial V_z}{\partial y} + V_z \frac{\partial V_z}{\partial z} \right) = -\frac{\partial p}{\partial z} + \mu \left( \frac{\partial^2 V_z}{\partial x^2} + \frac{\partial^2 V_z}{\partial y^2} + \frac{\partial^2 V_z}{\partial z^2} \right) \quad (3.4)$$

Substitution of  $V_z = 0$  in the above equations results in 2-D governing equations.

For non-isothermal flow over the cylinder in plane channel, the 2-D energy equation is

$$\rho C_p \left( \frac{\partial T}{\partial t} + V_x \frac{\partial T}{\partial x} + V_y \frac{\partial T}{\partial y} \right) = k \left( \frac{\partial^2 T}{\partial x^2} + \frac{\partial^2 T}{\partial y^2} \right) \quad (3.5)$$

### 3.5 Boundary conditions:

The following are the boundary conditions for three cases, 2-D isothermal flow in unbounded domain, 3-D isothermal flow in unbounded domain and 2-D non-isothermal flow in a plane channel.

#### 3.5.1 Two-dimensional (2-D) isothermal flow over a cylinder in unconfined domain:

*Inlet boundary:* The fluid is assumed to enter the left half of the outer circular boundary at a uniform velocity  $U_\infty$

$$V_x = U_\infty; V_y = 0 \quad (3.6)$$

*Outflow boundary:* the right half of the outer circular boundary is taken as outflow boundary.

In this case zero diffusion flux for all variables is assumed. This implies that the conditions of the outflow plane are extrapolated from within the domain and have no impact on the upstream flow. This is in consistent with fully developed flow assumption.

*Surface of the cylinder:* At the surface of the cylinder, no slip boundary condition is applied.

$$V_x = 0; V_y = 0 \quad (3.7)$$

### 3.5.2 Three-dimensional (3-D) isothermal flow over a cylinder in unconfined domain:

*Inlet boundary:* The fluid enters the plane  $ABCD$  at a uniform velocity  $U_\infty$

$$V_x = U_\infty; V_y = 0 \text{ and } V_z = 0 \quad (3.8)$$

*Free slip boundaries:* At the planes confining the cylinder in  $y$ -direction,  $ABEF$  and  $CDGH$ , free slip boundary condition is specified. This boundary condition ensures that the change of flow variables at the boundary in  $y$ -direction is negligible.

$$\frac{\partial u_x}{\partial y} = 0, \frac{\partial u_y}{\partial y} = 0, \text{ and } \frac{\partial u_z}{\partial y} = 0 \quad (3.9)$$

*Symmetric boundaries:* At the planes confining the cylinder in  $z$ -direction,  $BFGC$  and  $AEHD$ , symmetric boundary condition is specified. FLUENT assumes a zero flux of all quantities across a symmetry boundary. There is no convective flux across a symmetry plane, i.e. the normal velocity component at the symmetry plane is zero. There is no diffusion flux across a symmetry plane, i.e. the normal gradients of all flow variables are zero at the symmetry plane. The symmetry boundary condition therefore ensures zero normal velocity and zero normal gradients of all variables at the symmetry plane.

*Outflow boundary:* At the plane  $EFGH$ , outflow boundary condition is specified.

*Surface of the cylinder:* At the surface of the cylinder, no slip boundary condition is applied.

$$V_x = 0; V_y = 0 \text{ and } V_z = 0 \quad (3.10)$$

### 3.5.3 Two-dimensional (2-D) non-isothermal flow in a plane channel.

*Inlet boundary at  $AC$ :* The fluid is assumed to enter the inlet with a parabolic velocity profile  $U_x = U_{max}(1-(y/H/2)^2)$  with a free stream temperature of  $T_\infty$ .

$$V_x = U_{max}(1-(y/H/2)^2); V_y = 0 \text{ and } T = T_\infty \quad (3.11)$$

*Outflow boundary at BD:* Zero diffusion flux for all variables is assumed at the outlet boundary.

*Walls AB and CD:* No slip condition with impervious wall is applied at confining walls AB and

CD and these walls are at free stream temperature of  $T_\infty$ .

$$V_x = 0; V_y = 0 \text{ and } T = T_\infty \quad (3.12)$$

*Surface of the cylinder:* At the surface of the cylinder, no slip boundary condition is applied and the cylinder is at a temperature of  $T_w$ .

$$V_x = 0; V_y = 0 \text{ and } T = T_w \quad (3.13)$$

### 3.6 Calculation of drag and lift coefficients

The total drag force exerted by the fluid on the cylinder is the sum of pressure and friction drags. The total drag coefficient (dimensionless) in case of unbounded domain is defined as

$$C_D = \frac{F_D}{\frac{1}{2} \rho u_\infty^2 d} \quad (3.14)$$

where  $F_D$  is the total drag force per unit length of the cylinder.

The lift coefficient (dimensionless) in case of unbounded domain is defined as

$$C_L = \frac{F_L}{\frac{1}{2} \rho u_\infty^2 d} \quad (3.15)$$

where  $F_L$  is the lift force per unit length of the cylinder.

The total drag coefficient in case of a cylinder confined in a plane channel is defined as

$$C_D = \frac{F_D}{\frac{1}{2} \rho \bar{u}_d^2 d} \quad (3.16)$$

where  $\bar{u}_d$  is the average velocity based on the diameter of the cylinder given by

$$\bar{u}_d(\beta, \gamma) = \frac{1}{d} \int_{d_2}^{d_1} u_{\max} \left( 1 - \left( \frac{y}{H/2} \right)^2 \right) dy \quad (3.17)$$

where  $d_1$  and  $d_2$  are y-coordinates of the cylinder and are function of  $\beta$  and  $\gamma$  as given below

$$d_1 = \frac{d}{2\beta} (\gamma(1-\beta) - 1) + d \quad (3.18)$$

$$d_2 = \frac{d}{2\beta} (\gamma(1-\beta) - 1) \quad (3.19)$$

The lift coefficient (dimensionless) in case of confined domain is defined as

$$C_L = \frac{F_L}{\frac{1}{2} \rho \bar{u}_d^2 d} \quad (3.20)$$

### 3.7 Calculation of Strouhal number

The non-dimensional frequency of oscillation of cylinder is defined as Strouhal number.

In case of unbounded domain, Strouhal number is given as

$$St = \frac{f}{\bar{u}_\infty / d} \quad (3.21)$$

Strouhal number in the case of confined domain is given as

$$St = \frac{f}{\bar{u}_d / d} \quad (3.22)$$

where  $f$  is the frequency of oscillation of the lift coefficient of the cylinder or the vortex shedding frequency.

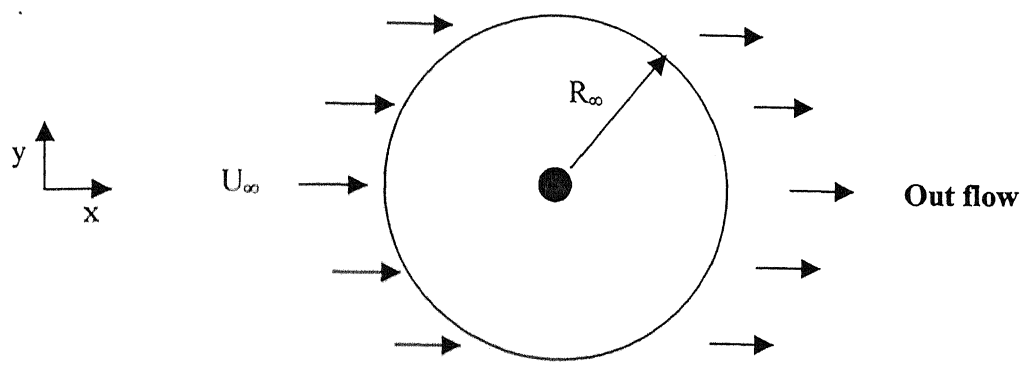


Figure 3.1: Schematic for 2-D flow past a cylinder in unbounded domain ( $R_\infty/r = 140$ )

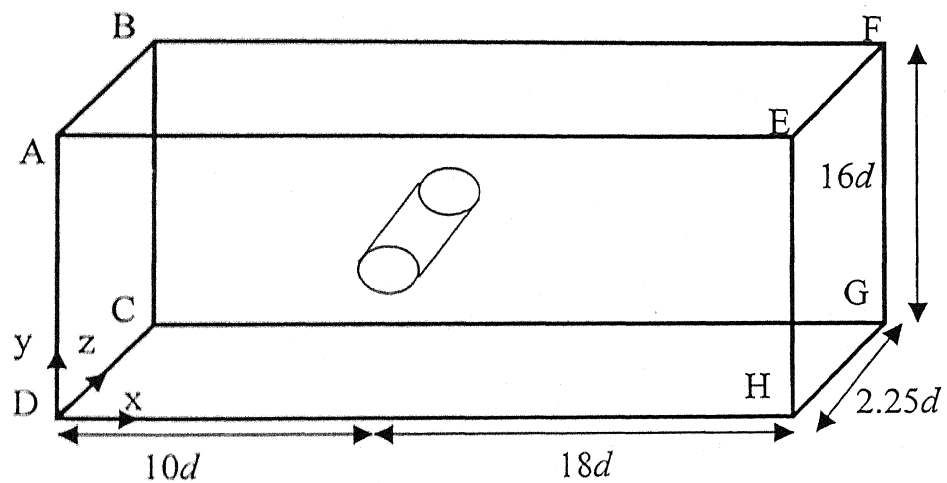


Figure 3.2: Schematic for 3-D flow past a cylinder in unbounded domain

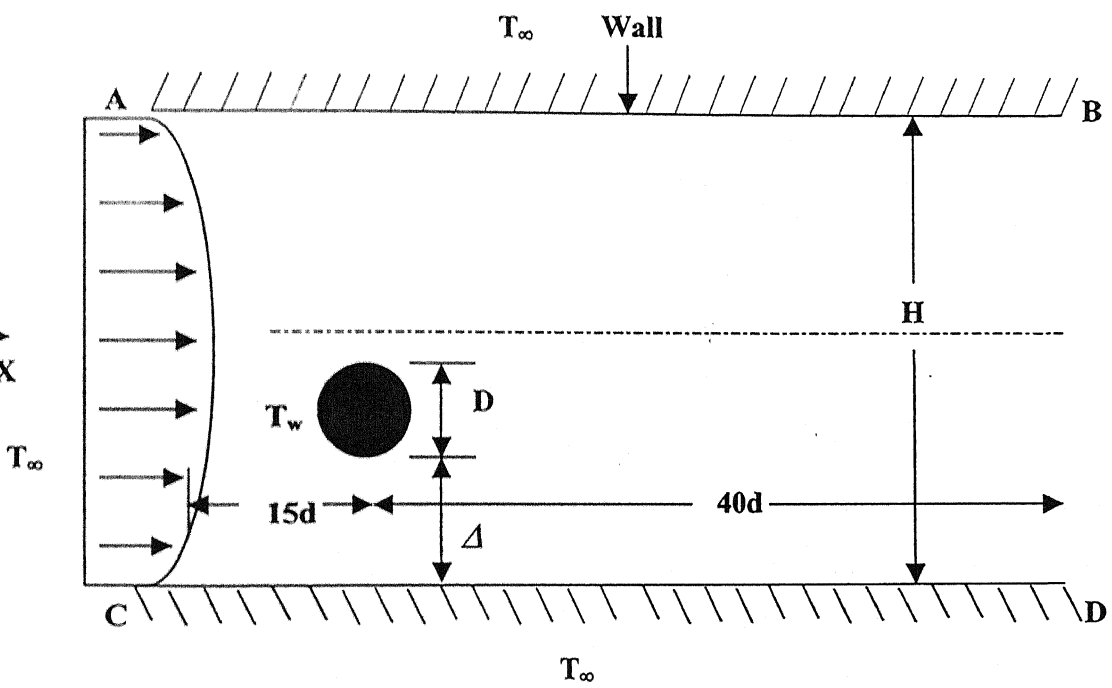


Figure 3.3: Schematic for flow past an asymmetrically confined cylinder in a plane channel

## Chapter 4

### Numerical Methodology

In the present study, a commercial flow modeling software, FLUENT 6.1 has been used to carry out numerical simulations. FLUENT employs a finite volume based numerical method to solve the governing flow and energy equations.

#### 4.1 Finite volume method

The finite volume based method consists of (a) division of the domain into discrete control volumes using a computational grid, (b) integration of the governing equations on the individual control volumes to construct algebraic equations for the discrete dependent variables such as velocities, pressure, temperature, and (c) linearization of the discretized equations and solution of the resultant linear equation system to yield updated values of the dependent variables.

#### 4.2 Grid generation

The first step in the solution of either flow or heat transfer problem using FLUENT is to build the appropriate geometry and divide the geometry into discrete control volumes (grid or cells). In this study, a commercial grid generation software, GAMBIT (in built with FLUENT), is used for the creation of geometry, division of the domain into discrete control volumes, and for the specification of the appropriate boundary conditions on the edges (or faces).

##### 4.2.1 Two-dimensional grid generation

The grid generation procedure for 2-D geometries is summarized as follows:

- The edges are created from the vertices followed by faces from edges.
- The edges are graded using different grading schemes available in GAMBIT, namely: successive ratio, first last ratio, and last first ratio.
- The faces (the computational domain) are meshed using different paving schemes available in GAMBIT, namely: Quadrilateral-Pave and Triangular-Pave scheme.
- Appropriate boundary conditions are specified on the boundaries (edges).

The computational domain in the case of rectangular geometry is divided into discrete control volumes using either of the schemes Quadrilateral-Pave or Triangular-Pave scheme. The combination of these two schemes, Quad-Tri-Pave scheme is used for 2-D circular geometry. The accuracy of any numerical solution depends on the fineness of the grid used for the computation. A non-uniform mesh with finer mesh around the cylinder where the velocity gradients are expected to be high and coarse mesh away from the cylinder is created using successive ratio grading scheme on the edges. The grid sensitivity analysis is carried out by increasing the number of uniform intervals on the surface of the cylinder until the drag coefficient and Nusselt number became insensitive to further mesh refinement.

#### *4.2.2 Three-dimensional grid generation*

The grid generation procedure for 3-D geometries is summarized as follows:

- The volumes are created using readily available geometries such as a cylinder and a rectangular brick. Boolean operations are performed on the volumes to define appropriate computational domain.
- The volume is divided into smaller volumes so as to facilitate finer mesh around the cylinder and coarser mesh away from the cylinder.
- The edges are graded using different grading schemes available in GAMBIT.
- The faces are meshed using Quadrilateral-Pave schemes followed by meshing the volumes using Cooper scheme which creates identical mesh in the third (z) direction.
- Appropriate boundary conditions are specified on the boundaries (faces).

### **4.3 Solution procedure**

After specifying the proper boundary conditions on the edges or faces, the mesh file is exported to FLUENT for simulation purposes. The solution method involves a few steps as outlined below.

#### *4.3.1 Selection of the solver*

FLUENT allows user to choose either of the two numerical solution methods, namely: (a) segregated solver, and (b) coupled solver, to linearize and solve the

discretized governing equations. Both of the solution methods use a finite volume discretization method. However, the approach to linearize and solve the discretized equations is different for both the schemes. In general both the solvers are applied in solving wide variety of fluid flow and heat transfer problems. The segregated solver is specifically used in solving incompressible flows and mildly compressible flows, whereas the coupled solver is specially developed for solving high-speed compressible flows. However, in this study, keeping in view of the incompressible nature of the flow, the segregated solver is used. In this method, the governing equations, namely: the continuity, momentum and energy equations (heat transfer) are solved sequentially i.e. one after the other (one at a time).

#### *4.3.2 Selection of the discretization scheme*

##### *4.3.2.1 Pressure interpolation scheme*

FLUENT uses a collocated grid in which both vectors (velocity and fluxes) and scalar quantities (pressure and temperature) are stored at cell centers. However, in the discretized momentum equation, face values of pressure are required. Therefore, an interpolation scheme for pressure is required to compute the face values of from the adjoining cell values. There are five interpolation schemes available in FLUENT for pressure computation: (i) standard, (ii) linear, (iii) second order, (iv) body-Force weighted and (v) PRESTO. In the present study standard pressure interpolation scheme has been used.

##### *4.3.2.2 Pressure-Velocity coupling*

In segregated solution method, the continuity equation is used as an equation for pressure, even though pressure does not appear explicitly in the discretized continuity equation. Therefore some numerical scheme is required to account for pressure velocity coupling. There are three algorithms available in FLUENT for pressure-velocity coupling: (i) SIMPLE, (ii) SIMPLEC, (iii) PISO. The pressure-velocity coupling scheme pressure-implicit with splitting of operators (PISO) is used for unsteady flows as suggested by FLUENT user manual.

#### 4.3.2.3 Momentum Upwinding

As mentioned earlier, FLUENT uses a collocated grid in which both fluxes and scalar quantities are stored at cell centers. However, for convective terms in the discretised momentum and energy equations, the face values of the dependent variables are required which are interpolated from the cell center values of the adjoining cells. Upwinding means that the face values are derived from cells in the up wind direction relative to the direction of the flow. There are four upwinding schemes available in FLUENT: (i) first order upwind, (ii) second order upwind, (iii) power-law, and (iv) QUICK. In this study second order upwinding scheme is used for both the momentum and energy equations. In this method the cell face values is approximated by expanding through a Taylor series about the cell center value. The comparison of three-upwinding schemes, first order, second order and QUICK is also studied with respect to the transition of flow past a circular cylinder from steady to unsteady flow.

#### 4.3.3 Convergence criteria

In the present study, a convergence criterion of  $1 \times 10^{-09}$  has been applied to the residuals of the continuity, the momentum and energy equation. In the case of steady flows, the iterations are stopped when the solution reaches steady state, whereas in the case of unsteady flows, the iterations are stopped when the oscillations of the lift coefficient reach a periodic steady state.

## CHAPTER 5

### MODEL VALIDATION

In the present study, the momentum and heat transfer from a circular cylinder has been studied using the commercial flow modeling software, FLUENT 6.1. Before solving the problem of interest, the code has been validated with the results reported in the literature. A reliable validation helps in determining the accuracy of the code used and gives the necessary idea about the problem to be solved. In this chapter, the comparison of our results with the published data for the steady and unsteady momentum and heat transfer from a circular cylinder in confined as well as in unconfined domain is presented.

#### 5.1 Momentum and heat transfer from a cylinder in unconfined domain in the steady flow range ( $Re < 50$ )

For the validation of our results with the published data for  $Re < 50$ , a circular geometry with a circular outer boundary located at 112 radii way from the surface of the cylinder is chosen. A grid size of  $90 \times 60$  previously used by Chakraborty et.al [55] is chosen for the computation in this work. The values of  $C_D$  obtained in this study are compared with the published results and are found to be in good agreement, as shown in Table 5.1 and Figure 5.1. The maximum deviation from the literature values is 8.2% at  $Re = 40$ , which is due to the smaller outer boundary ( $r_\infty/r = 29$ ) used by Sucker and Brauer [42]

The validation of heat transfer results for  $\overline{Nu}_w$  ( $Pr = 0.7441$ ) for the flow of air past a circular cylinder in unconfined domain is carried out using a circular geometry, with the outer circular boundary fixed at 1000 radii away from the circular cylinder, keeping in view of the low  $Re$ . The values of  $\overline{Nu}_w$  for the range of  $Re$  between 0.01 and 40 are compared with the published results and are found to be in good agreement as shown in Table 5.2 and Figure 5.2. A maximum deviation of 4.1% from the literature value is observed at  $Re = 40$ , which is within the acceptable accuracy.

## 5.2 Momentum transfer from a cylinder in unconfined domain in the unsteady flow range

The validation of  $\bar{C}_D$  (time average),  $C_L$  and  $St$  for the range of  $Re$  from 50 to 1000 is carried out using a circular geometry, with the outer circular boundary located at 140 radii away from the cylinder. The grid sensitivity analysis is carried out on this geometry, as shown in Table 5.3. It is observed that as the grid size is refined from  $110 \times 120$  to  $120 \times 144$ , the change in the value of  $\bar{C}_D$  is less than 0.24%. Hence, the  $\bar{C}_D$  values obtained using the grid size of  $120 \times 144$  may be treated as grid independent. Therefore, the grid size of  $120 \times 144$  was used as the optimum grid for further computations in this study. In Table 5.4 and Figure 5.3,  $\bar{C}_D$  values computed in this study are compared with those available in the literature. The maximum deviation in  $\bar{C}_D$  from the literature values for  $Re$  below 500 is 5.3%. At  $Re = 1000$ , the deviation in  $\bar{C}_D$  value from that of Braza et al. [17] is 23%. However, the drag value at  $Re = 1000$  is in good agreement with  $\bar{C}_D$  values obtained by Franke et al. [22] and Henderson [40], with a deviation of less than 2.4%. The reason for the large deviation (23%) of  $\bar{C}_D$  value computed by Braza et al. [17] from that of the values reported in the literature is not known.

In Table 5.5,  $C_L$  and  $St$  values are compared with the values reported in the literature. As observed,  $C_L$  is in good agreement with the values obtained by Franke et al [22]. The comparison of  $C_L$  with those obtained by Braza et al. [17] could not be made as the authors have reported r.m.s values of  $C_L$ . It is observed from Table 5.5 that there is a good agreement between the values of  $St$  calculated in the present study and the literature at all  $Re$ , except at  $Re = 1000$ , at which the calculated value is 7.7% higher than the value obtained by Braza et al. [17]. The comparison of  $St$  values with those obtained by Braza et al. [17] and Franke et al. [22] is also shown in Figure 5.4.

The comparison of  $\bar{C}_D$ ,  $C_L$  and  $St$  for  $Re = 50, 100, 200$ , and  $1000$  with various simulation and experimental investigations reported in literature is presented in Table 5.6.  $C_D$  value obtained in this study for  $Re = 50$  is in excellent agreement with the simulation results of Saiki and Biringen [43] and that of the experimental result of Clift et al. [44],

with a maximum deviation of 1.2%. However, at  $Re = 50$  there is a deviation of 23% in  $\bar{C}_D$  value that of Gresho et al. [21]. It is to be noted from Table 5.6 that  $\bar{C}_D$  obtained by Gresho et.al. [21] for  $Re = 100$  and 200 also show a large deviation from the rest of the values reported in the literature, whereas  $\bar{C}_D$  obtained in our study is in good agreement (deviation  $< 2.05\%$ ) with the experimental value of Clift et al. [44] as well as with the simulation results of Kim et al. [47], and Wanderley and Levi [48].  $\bar{C}_D$  reported in the literature at  $Re = 200$  is in the range of 1.24 to 1.76, as shown in the Table 5.6 and  $\bar{C}_D$  obtained in our study is 1.2981, which is within the range.

From Table 5.6,  $St$  value for  $Re = 50$  is observed to be in good agreement with the experimental values of Roshko [45], and Berger and Wille [46]. In the present study, the maximum deviation of  $St$  value from experimental value at  $Re = 50$  is less than 1.6%. The value of  $St$  at  $Re = 100$  is in good agreement with the experimental values of Roshko [45], and Berger and Wille [46], as well as with the simulation results presented in Table 5.6. The maximum deviation at  $Re = 100$  is 7.5% from the simulation result of Rengel and Sphaier [49]. The value of  $St$  at  $Re = 200$  is in good agreement with the experimental as well as simulation results, with a maximum deviation of 9% from the value obtained by Gresho et al. [21]. Finally,  $\bar{C}_D$  and  $St$  values at  $Re = 1000$  are found to be in good agreement with the literature values, with a maximum deviation of 2.4% and 5.3%, respectively.

### 5.3 Momentum and heat transfer from a cylinder confined in a plane channel

In the present thesis, the main objective is to study the momentum and heat transfer characteristics ( $\bar{C}_D$ ,  $St$ , and  $\bar{Nu}_w$ ) from an asymmetrically confined circular cylinder in a plane channel. Before solving the problem of our interest, the results for momentum and heat transfer for an asymmetrically confined circular cylinder in plane channel are validated with the published data of Zovatto and Pedrizzetti [24] for  $\beta = 0.2$  and  $\gamma = 0.375$  and also 1 (symmetrical case). The simulation of flow past a symmetrically confined as well as asymmetrically confined cylinder is carried out using the rectangular geometry with a downstream length of  $40d$  and upstream length of  $15d$ , and with a parabolic velocity specified at the inlet, as shown in Figure 3.3. Referring Table 5.9 for  $\beta = 0.2$  and  $\gamma = 0.375$

the drag values are found to be in good agreement with the results obtained by Zovatto and Pedrizzetti [24]. The maximum deviation in  $\bar{C}_D$  is 5.8% at  $Re = 40$ , which is within the acceptable accuracy.

Since the published data available in the literature for an asymmetrically confined cylinder is limited, the model was also validated with the data of Khan et al [41] for a symmetrically confined cylinder in a plane channel. The comparison of results for  $\bar{C}_D$  and  $\bar{Nu}_w$  with the published data of Khan et al. [41] for  $\beta = 0.1$  and  $0.2$  is shown in Tables 5.7 and 5.8, respectively. The comparison is also described in Figures 5.5 and 5.6. The deviation in  $\bar{C}_D$  for  $\beta = 0.1$  obtained in this study from those obtained by Khan et al. [41] is significantly high with a maximum deviation of 40% at  $Re = 50$ , whereas  $\bar{Nu}_w$  values are in close agreement with a maximum deviation of 4.7% at  $Re = 20$ . The maximum deviation in  $\bar{C}_D$  for  $\beta = 0.2$  is 24% at  $Re = 69$ , whereas the maximum deviation in  $\bar{Nu}_w$  is 9.5% at  $Re = 1000$ . This large deviation in  $\bar{C}_D$  is attributed to the difference in the velocity profile specified at the inlet of the channel and different velocity profile near the cylinder. In the study of Khan et al. [41], a uniform velocity is specified at the inlet and near the cylinder, whereas in our study a parabolic velocity is specified at the inlet and the cylinder is also assumed to experience the parabolic velocity profile. The reference velocity used for the drag calculation in our study is the velocity averaged over the surface of the cylinder, while Khan et al. [41] have used the free stream velocity as the reference value. The above mentioned differences in the two studies have caused deviation in  $\bar{C}_D$ . The drag values for  $\beta = 0.2$  are also found to be in good agreement with those obtained in the study by Zovatto and Pedrizzetti [24], in which case the parabolic velocity is specified at the inlet and the average velocity is used as the reference for the drag calculation.

From these comparisons, it may be concluded that  $\bar{C}_D$  and  $\bar{Nu}_w$  obtained using this code are accurate within 5-10% of the values reported in the literature. The close agreement between the results obtained in this study and the literature gave us the confidence in the code used. Therefore, we have used the same code for studying the momentum and heat transfer characteristics from an asymmetrically confined circular cylinder in a plane channel for various blockage ratios ( $\beta$ ) and gap ratios ( $\gamma$ ).

S.No	$Re$	$C_D$ This work	$C_D$ Chakraborty et al. (2004)*	$C_D$ Kawaguti and Jain (1966)**	$C_D$ Sucker and Brauer (1975)+	$C_D$ D' Alessio and Dennis (1994)++
1	1	10.374	10.445	-	-	-
2	10	2.757	2.803	2.870	-	-
3	20	2.001	2.035	2.090	2.178	1.941
4	30	1.702	1.702	1.760	-	-
5	40	1.499	1.517	1.529	1.633	1.443
6	50	1.392	1.392	1.440	-	-

**Table 5.1: Comparison of  $C_D$  values with the published data for the steady flow range (<sup>\*</sup>  $r_\infty/r = 112$ , <sup>\*\*</sup>  $r_\infty/r = 112$ , <sup>+</sup>  $r_\infty/r = 29$ , <sup>++</sup>  $r_\infty/r = 55$ )**

S.No	$Re$	$\overline{Nu}_w$ This work	$\overline{Nu}_w$ Dennis and Hudson (1968)	$\overline{Nu}_w$ Collis and Williams (1959)	$\overline{Nu}_w$ Lange et al. (1998)
1	0.01	0.308	0.302	0.296	0.29
2	0.1	0.453	0.452	0.439	0.44
3	1	0.819	0.812	-	0.80
4	10	1.890	1.897	-	1.9
5	20	2.540	2.557	-	2.5
6	40	3.337	3.480	-	3.4

**Table 5.2: Comparison of  $\overline{Nu}_w$  ( $Pr = 0.7441$ ) values with the published data for the steady flow range**

S.No	Re	Grid size (90×120) $\overline{C}_D$	Grid size (110×120) $\overline{C}_D$	Grid size (120×144) $\overline{C}_D$
1	20	1.956	1.949	1.948
2	40	1.513	1.513	1.512
3	50	1.390	1.393	1.397
4	100	1.302	1.302	1.305

**Table 5.3: Grid independence test using QUICK scheme for momentum upwinding**

S.No	$Re$	$\bar{C}_D$ This work	$\bar{C}_D$ Braza et al. (1986)	$\bar{C}_D$ Franke et al. (1990)	$\bar{C}_D$ Henderson (1995)	Max % deviation with literature value
1	50	1.393	1.400	1.39	1.412	1.3%
2	100	1.302	1.253	-	1.349	3.9%
3	150	1.289	-	-	1.333	3.3%
4	180	1.293	-	-	1.336	3.3%
5	200	1.298	1.321	1.31	1.341	3.2%
6	250	1.314	1.359	-	1.357	3.2%
7	300	1.329	1.405	1.32	1.376	5.3%
8	500	1.381	-	-	1.448	4.5%
9	1000	1.473	1.198	1.47	1.509	23%

**Table 5.4: Comparison of  $\bar{C}_D$  values with the published data for the unsteady flow range**

S.No	$Re$	$C_L$ This work	$C_L$ Franke et al. (1990)	$St$ This work	$St$ Braza et al. (1986)	$St$ Franke et al. (1990)
1	50	$\pm 0.010$	$\pm 0.0$	0.1212	0.120	0.116
2	100	$\pm 0.269$	-	0.1600	0.165	-
3	150	$\pm 0.455$	-	0.1790	0.181	-
4	180	$\pm 0.537$	-	0.1870	0.185	-
5	200	$\pm 0.599$	$\pm 0.65$	0.1912	0.198	0.194
6	250	$\pm 0.701$	-	0.1990	0.204	-
7	300	$\pm 0.814$	$\pm 0.84$	0.2060	0.209	0.205
8	500	$\pm 1.011$	-	0.2222	-	-
9	1000	$\pm 1.307$	$\pm 1.36$	0.2370	0.22	0.236

**Table 5.5: Comparison of  $C_L$ ,  $St$  values with the published data for the unsteady flow range**

	$Re$	$\bar{C}_D$	$C_L$	$St$
Tseng and Ferziger (2003)	100	1.42	0.29	0.164
Kim et al. (2001)	100	1.33	-	0.165
Saiki and Biringen (1996)	50	1.38	-	0.139
	100	1.26	-	0.171
	200	1.18	-	0.192
Gresho et al. (1984)	50	1.81	-	0.14
	100	1.76	-	0.18
	200	1.76	-	0.21
Clift et al. (1978) (Experimental)	50	1.41	-	-
	100	1.33	-	-
	200	1.24	-	-
Roshko (1953) (Experimental)	50	-	-	0.122
	100	-	-	0.167
Berger and Wille (1972) (Experimental)	50	-	-	0.12-0.13
	100	-	-	0.16-0.17
	200	-	-	0.18-0.19
Meneghini (1993)	100	1.520	0.353	0.162
	200	1.395	0.570	0.195
Herfjord (1995)	100	1.36	0.34	0.168
	200	1.35	0.70	0.196
	1000	1.47	1.45	0.234
Rengel and Sphaier (1999)	100	1.36	0.32	0.173
	200	1.35	0.67	0.203
	1000	1.50	1.70	0.225
Wanderley and Levi (2002)	100	1.33	0.195	0.163
	200	1.32	0.534	0.192
	1000	1.51	1.370	0.235
Present study	50	1.393	0.010	0.121
	100	1.302	0.269	0.160
	200	1.298	0.599	0.191
	1000	1.473	1.307	0.237

**Table 5.6: Comparison of  $\bar{C}_D$ ,  $C_L$ ,  $St$  values with the experimental and simulation results**

S.No	$Re$	$\bar{C}_D$ This work	$\bar{C}_D$ Khan et al. (2004)	$\bar{Nu}_w$ This work	$\bar{Nu}_w$ Khan et al. (2004)
1	20	2.157	2.526	2.526	2.411
2	30	1.780	2.266	2.969	2.953
3	40	1.567	2.112	3.337	3.410
4	50	1.430	2.009	3.660	3.813
5	100	1.296	1.754	5.219	5.392
6	200	1.290	1.577	7.596	7.626
7	300	1.321	1.499	9.493	9.340
8	400	1.338	1.453	11.01	10.78
9	500	1.340	1.422	12.40	12.05
10	1000	1.40	1.344	17.30	17.05

Table 5.7: Comparison of  $\bar{C}_D$  and  $\bar{Nu}_w$  ( $Pr = 0.7441$ ) values for  $\beta = 0.1$

S.No	$Re$	$\bar{C}_D$ This work	$\bar{C}_D$ Zovatto and Pedrizzetti (2001)	$\bar{C}_D$ Khan et al. (2004)	$\bar{Nu}_w$ This work	$\bar{Nu}_w$ Khan et al. (2004)
1	20	2.671	-	2.603	2.667	2.450
2	30	2.142	-	2.337	3.119	3.000
3	40	1.860	-	2.180	3.497	3.464
4	50	1.681	-	2.074	3.830	3.873
5	60	1.556	-	1.996	4.135	4.243
6	69	1.471	1.6	1.941	4.4112	4.550
7	200	1.253	1.3	1.632	7.592	7.747
8	300	1.268	1.2	1.553	9.326	9.489
9	400	1.274	-	1.505	10.91	10.95
10	500	1.324	-	1.473	12.13	12.21
11	1000	1.368	-	1.395	18.98	17.32

Table 5.8: Comparison of  $\bar{C}_D$  and  $\bar{Nu}_w$  ( $Pr = 0.7441$ ) values for  $\beta = 0.2$

S.No	$Re$	$\bar{C}_D$ This work	$\bar{C}_D$ Zovatto and Pedrizzetti (2001)	$\bar{Nu}_w$ This work
1	20	3.150	3.0	2.706
2	40	2.222	2.1	3.609
3	60	1.852	1.8	4.269
4	108	1.481	1.5	5.539
5	200	1.333	1.3	7.615

**Table 5.9: Comparison of  $\bar{C}_D$  and  $\bar{Nu}_w$  ( $Pr = 0.7441$ ) values for  $\beta = 0.2$  and  $\gamma = 0.375$**

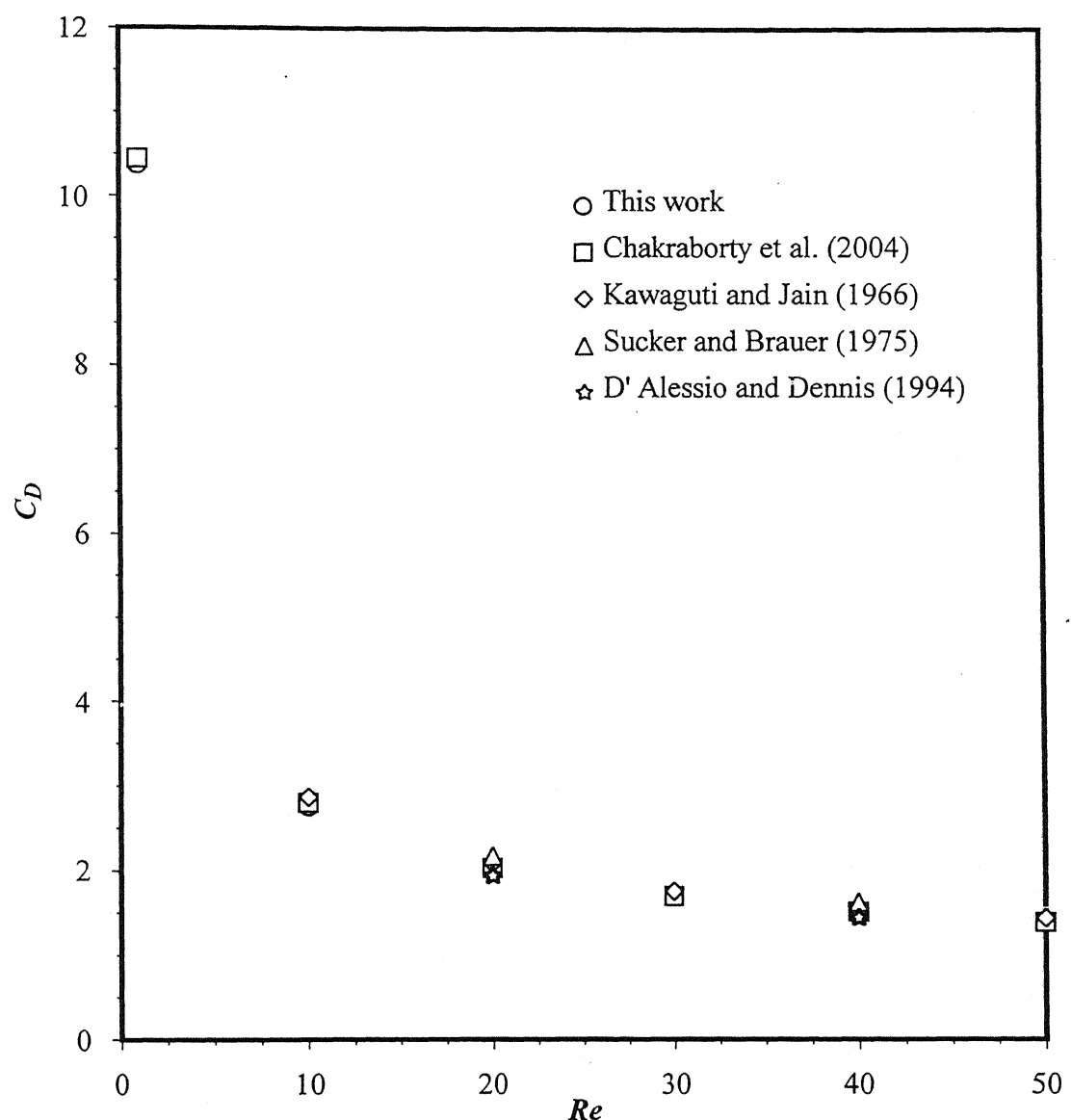


Figure 5.1: Validation of  $C_D$  for unconfined flow in the steady range ( $Re < 50$ )

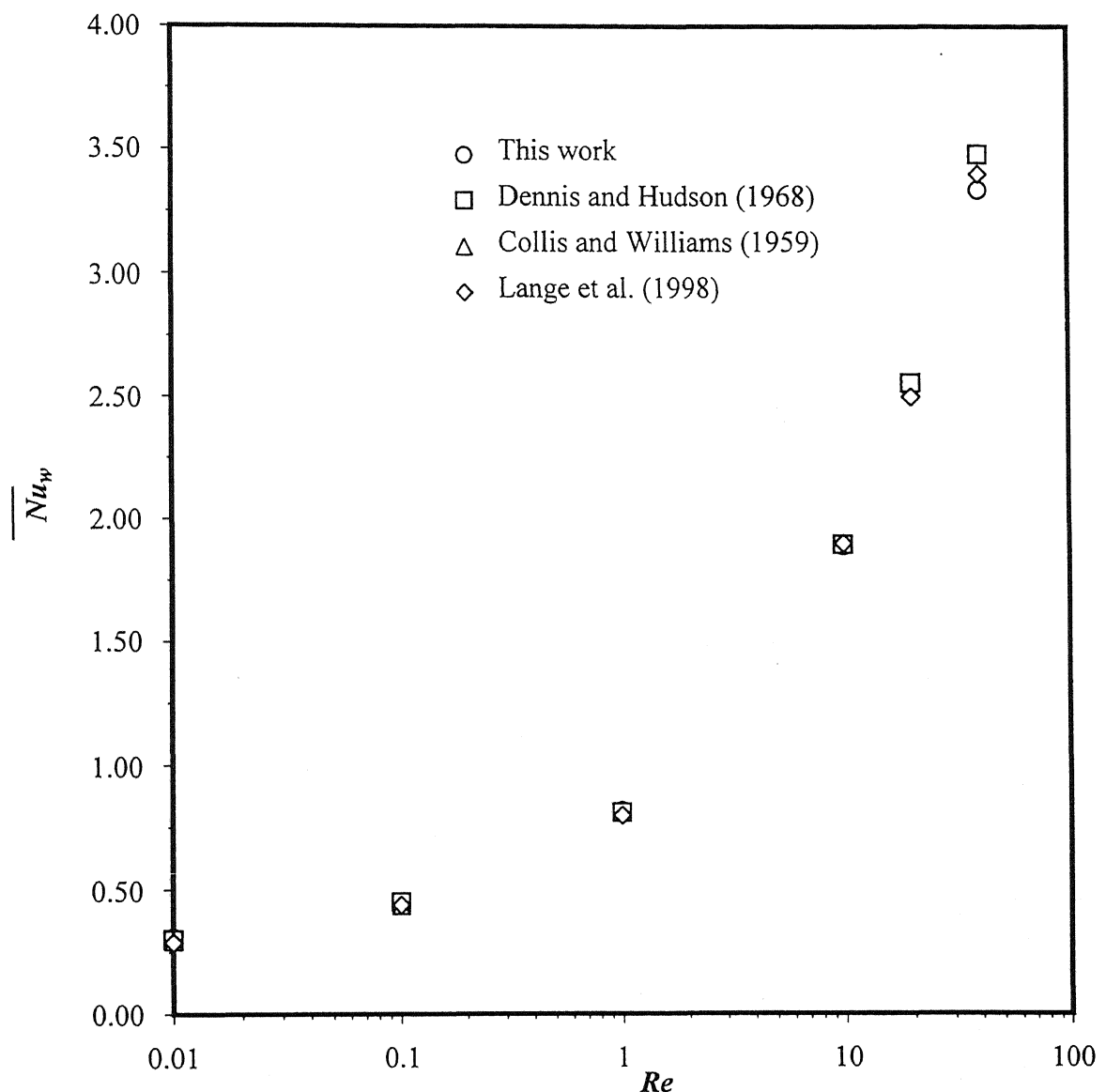


Figure 5.2: Validation for  $\overline{Nu}_w$  in unconfined flow (  $Re < 50$ ,  $Pr = 0.7441$  )

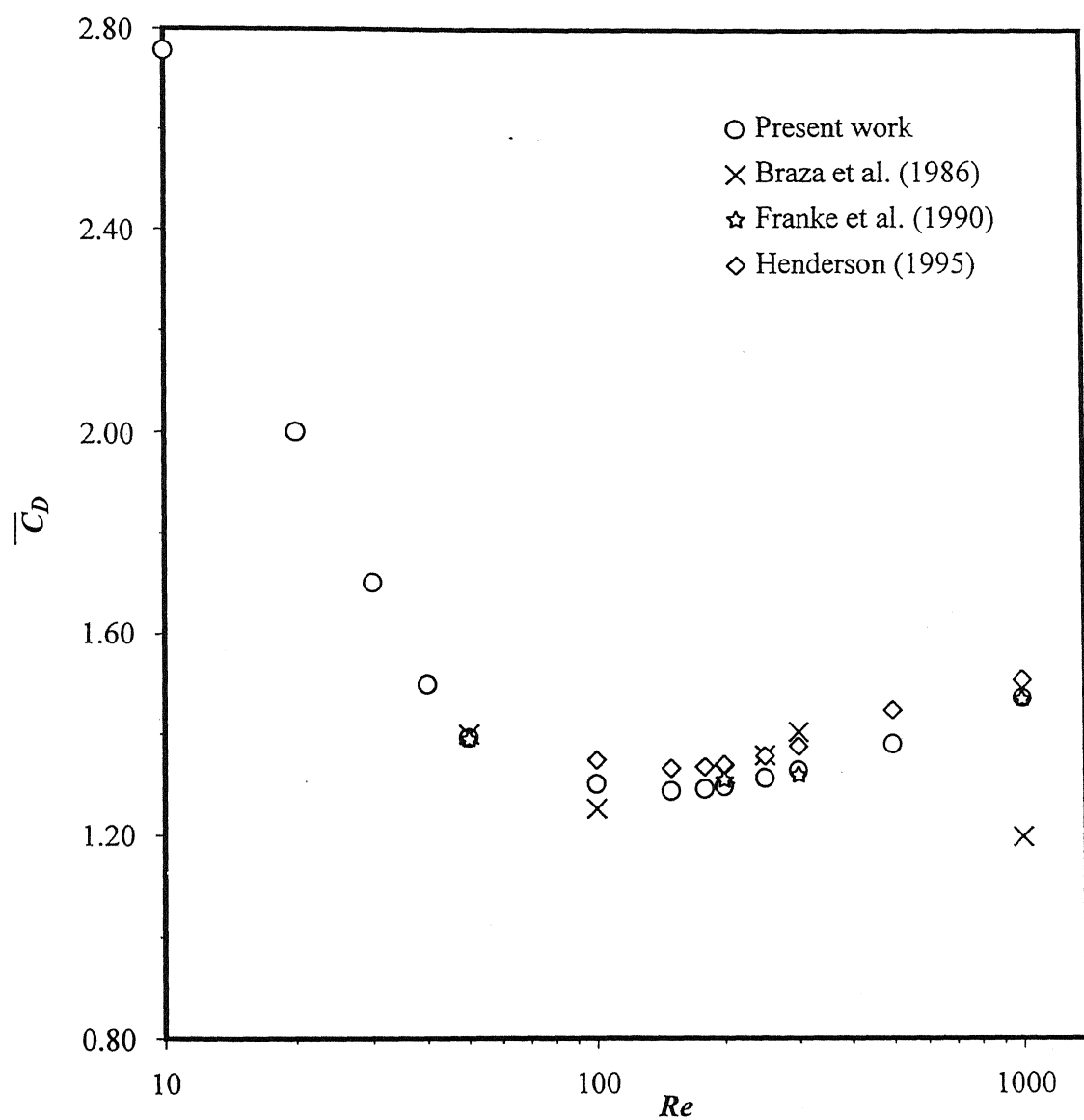


Figure 5.3: Validation of  $\bar{C}_D$  for unconfined flow in the unsteady range ( $R_0/r = 140$ )

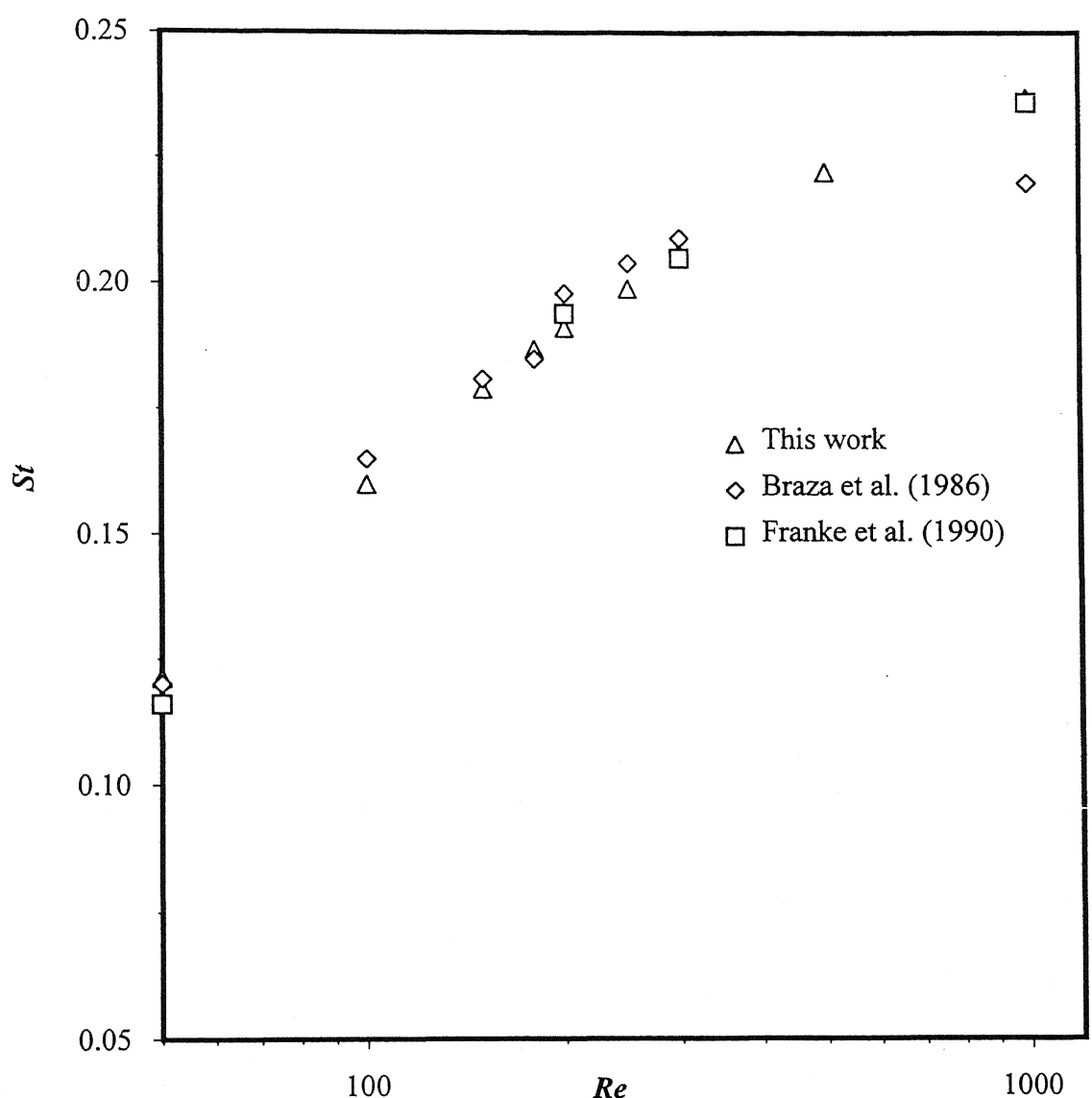


Figure 5.4: Validation of  $St$  for unconfined flow in the unsteady range ( $R_\alpha/r = 140$ )

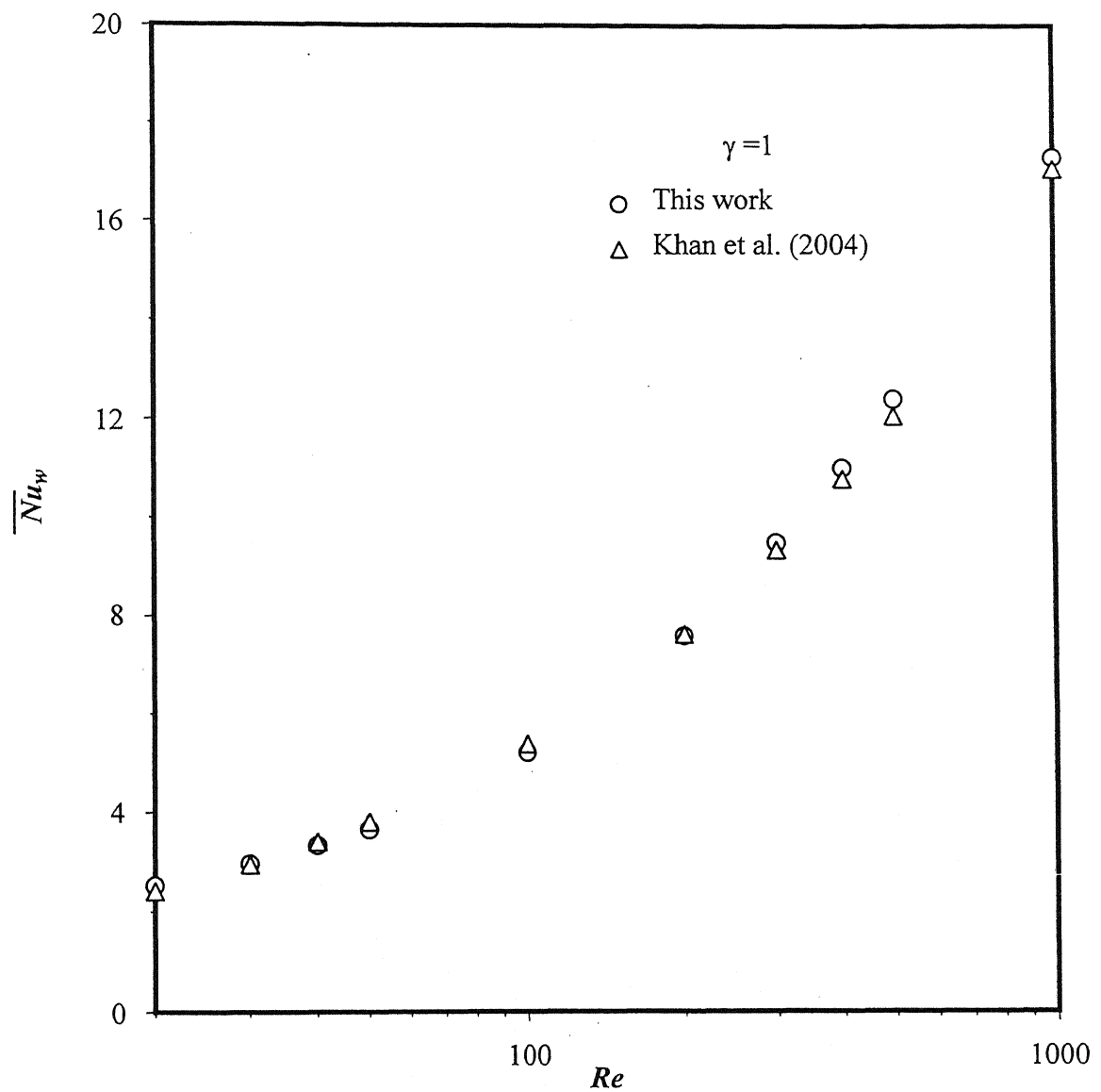
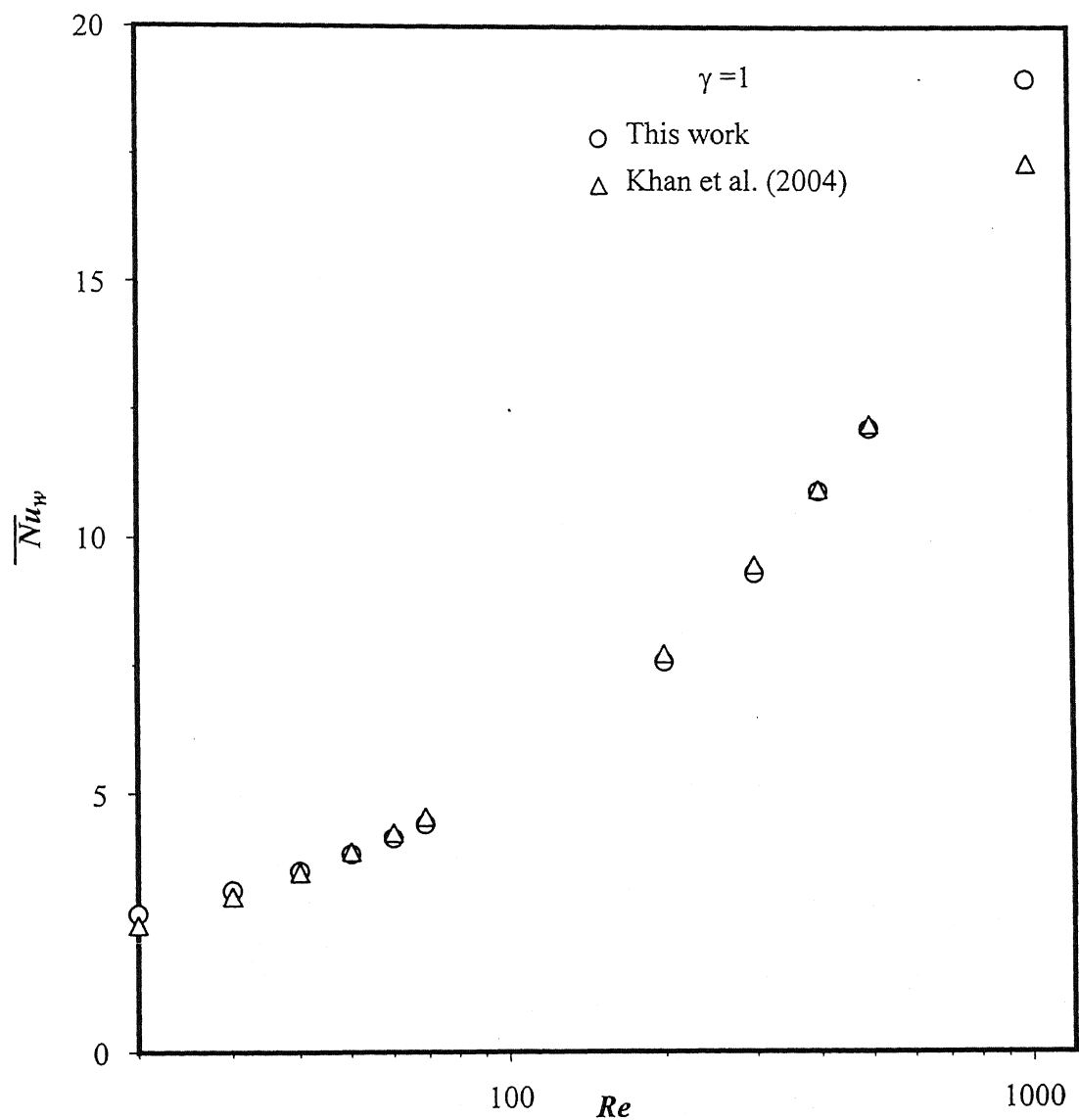


Figure 5.5: Validation of  $\overline{Nu}_w$  ( $Pr = 0.7441$ ) for  $\gamma = 1$  (symmetrical) for  $\beta = 0.1$



**Figure 5.6: Validation of  $\overline{Nu_w}$  ( $Pr = 0.7441$ ) for  $\gamma = 1$  (symmetrical) for  $\beta = 0.2$**

## CHAPTER 6

### RESULTS AND DISCUSSION

This chapter presents the simulation results for the flow of an incompressible, Newtonian fluid past a circular cylinder in unconfined as well as confined domains. The main objective of this study, as mentioned earlier, is to study the transition of flow from 2-D steady to 2-D unsteady in unconfined and confined domains. In the case of flow in unconfined domain, the validation of simulation results for  $\bar{C}_D$ ,  $St$ , and critical  $Re$  with the published data is presented. In addition, the comparison of  $\bar{C}_D$  and  $St$  and critical  $Re$  obtained using various upwinding schemes available in FLUENT is presented. Since the data available in the literature for the transition of the flow past a circular cylinder confined in a plane channel is limited [23,24], the transition is characterized as the function of asymmetry ( $\gamma$ , gap ratio) over a wide range of blockage ratios ( $\beta$ ). In this work, in particular the critical  $Re$  at which transition in the flow takes place is determined as a function of  $\gamma$  and  $\beta$ .

#### 6.1 The transition of flow past a circular cylinder from steady to unsteady in unbounded domain

The flow past a circular cylinder may be divided into different regimes depending on  $Re$ . For  $Re \sim 1$ , the flow is fore and aft symmetric, divides at front stagnation point and reunites smoothly behind the cylinder. As  $Re$  increases above 5, the flow separation takes places on the downstream side with formation of two symmetric vortices, which are stable and remain attached to the cylinder. Around  $Re = 47$ , flow transition takes place from steady to unsteady, in which case the oscillations of vortices give rise to the well-known Von karman vortex street, with the non-dimensional number  $St$  characterizing the frequency of oscillation of the vortices. In this section, this flow transition is numerically studied by the various upwinding schemes available in FLUENT. The critical  $Re$  at which the transition takes place is determined for each of the upwinding schemes by carrying out unsteady numerical simulations.

The grid (120×144) used for the unsteady simulations is shown in Figure 6.1, which was found to be optimum by carrying out grid sensitivity analysis. The results for the grid independence study are shown in Table 5.3. In the simulation, the radius ( $R_\infty$ ) of outer circular

boundary is taken to be large ( $R_\infty/r = 140$ ) enough to ensure that the effect of boundaries on the flow field near the cylinder wall is negligible. The resolution of boundary layer near the cylinder wall significantly influences the numerical results. Therefore, to resolve the boundary layer accurately, a constant expansion factor is used while meshing the geometry that produces a non-uniform grid with a finer mesh near the cylinder and coarser mesh away from the cylinder. In particular, the distance of the first grid point from the cylinder wall is kept at 0.007% of the diameter of the cylinder. The time step ( $\Delta t$ ) in the unsteady simulation is kept below  $T/100$ , where  $T$  is the time period of the oscillations, i.e. more than 100 time steps per period are used.

#### 6.1.1 Vortex shedding initiation mechanism:

The time marching calculations were started with the step increase in the velocity from zero to free stream value of  $U_\infty$ . For  $Re > 40$ , one experimentally observes Von karman vortex street which is the characteristic of the unsteady flow. In the case of numerical simulations the destabilizing factors like, non-uniform inlet conditions, irregularity of the boundary conditions, vibrations and surface roughness that are usually present in the experimental conditions are absent as the boundary conditions and initial condition are symmetric, which in general should lead to the steady symmetric solution of the Navier-Stokes equations. However, in numerical simulations, the truncation errors, round-off errors and the errors due to numerical approximations act as destabilizing factors, which lead to vortex shedding. But the time period required for numerical errors to accumulate and eventually lead to vortex shedding turns out to be significantly large. Therefore, to reduce this transition period before the periodic vortex shedding could be observed from the cylinder, Braza et al. [17] have introduced a perturbation method to generate vortex shedding from the cylinder, which is based on the artificial rotation of the circular cylinder in clockwise direction followed by rotation in anticlockwise direction for a short duration and then keeping the cylinder stationary for the remaining part of the calculations, as depicted in Figure 6.2.

In our study, we have also used the method of Braza et al. [17] to generate vortex shedding from the cylinder. It has been shown by Martinez (1979) that any random or imposed perturbations die out for  $Re < 40$ , whereas they result in vortex shedding for  $Re > 50$ . The final periodic state solution should be the same irrespective of the magnitude of the disturbance, if the vortex shedding is intrinsic property of the flow at  $Re > 50$ . To ascertain this, the effect of the

magnitude of the disturbance has been tested by varying the speed of the rotation of the cylinder for  $Re = 100$ , as shown in Table 6.1. The cylinder is rotated for about hundred time steps in clockwise direction followed by rotation in anticlockwise direction using two different rotational speeds, 2 rad/sec and 6 rad/sec. It is evident from the results presented in Table 6.1 that the effect of the magnitude of the disturbance on global parameters like  $\bar{C}_D$ ,  $C_L$  and  $St$  is very insignificant. The final periodic state reached by the oscillations of  $\bar{C}_D$  and  $C_L$  for the two disturbances may be clearly observed from Figure 6.3. They are essentially identical for two disturbances, one of which is three times the other. From these observations, it may be concluded that vortex shedding is the intrinsic property of the flow and the final periodic state solution is not influenced by the magnitude of the disturbance introduced into the flow.

#### 6.1.2 Comparison of upwinding schemes:

The comparison of various upwinding schemes available in FLUENT for momentum upwinding, namely; first order upwinding, second order upwinding and QUICK schemes is presented with respect to the transition of the flow from steady to unsteady flow. The flow is perturbed slightly and the time dependent motion following perturbation is examined. The critical  $Re$  at which the disturbance given through the rotation of the cylinder amplifies leading to periodic vortex shedding is determined for each of the upwinding schemes. The results are shown in Table 6.2. The critical  $Re$  determined using second order and Quick upwinding schemes is 50, which is very close to the value (46) obtained by Jackson [18] using finite element method. The history of lift coefficient for  $Re = 48$  and 50 is shown in Figure 6.4 for the second order upwinding scheme. The disturbance introduced into the flow through the rotation of the cylinder decayed at  $Re = 48$ , whereas at  $Re = 50$  it is amplified, leading to periodic vortex shedding from the circular cylinder. The unsteady nature of the flow at  $Re = 50$  is depicted in Figure 6.5, in which case streamline plots for  $Re = 46, 48$ , and 50 are shown. The streamlines at  $Re = 46$  and 48 show symmetric vortices implying the steady nature of the flow, whereas at  $Re = 50$  the streamlines are asymmetric showing the unsteady nature of the flow. The time dependence of the flow at  $Re = 50$  is also described in Figure 6.5 via the streamline plots constructed at different time steps.

The lift coefficient history at  $Re = 50$  calculated from QUICK scheme is shown in Figure 6.6, which shows that the disturbance introduced into flow is sustained and resulted in periodic

vortex shedding from the cylinder. The streamline plots at  $Re = 50$  for different time steps are presented in Figure 6.7, in which case the unsteady nature of the flow is clearly evident. The critical  $Re$  determined using first order upwinding scheme for momentum upwinding is 100, which shows more than 100% deviation from the literature value of 46 [18]. The lift coefficient histories at  $Re = 94, 96$ , and 100 are shown in Figure 6.8 for the first order upwinding scheme. It is evident from the figure that perturbation decayed at  $Re = 94$  and 96, whereas it resulted in the periodic solution at  $Re = 100$ .

The comparison of  $\bar{C}_D$  and  $St$  in the range of  $Re$  from 50 to 1000 for the above-mentioned three-upwinding schemes is shown in Tables 6.3 and 6.4. Figure 6.9 also illustrates the variation in  $\bar{C}_D$ . It may be seen from the figure that both second order upwinding and QUICK scheme predict the identical time averaged drag coefficient with a negligible variation of 4%, whereas first order upwinding scheme predicts higher  $\bar{C}_D$  at  $Re \leq 50$  and lower  $\bar{C}_D$  at  $Re \geq 100$  than  $\bar{C}_D$  predicted by the second order and QUICK schemes. The comparison of  $St$  is described in Figure 6.10. As seen from the figure, second order and QUICK schemes predict the same  $St$  for each  $Re$  and are also in good agreement with those obtained by Braza et al. [17]. On the other hand, first order upwinding scheme predicts lower  $St$  values than the values reported in the literature.

## 6.2 The transition of flow past a circular cylinder confined in a plane channel from steady to unsteady

As shown in Section 6.1, the steady flow past a circular cylinder in unbounded domain loses stability leading to periodic vortex shedding as  $Re$ , based on the diameter of the cylinder, is increased above 50. However, when the circular cylinder is confined in a plane channel, in which case the velocity profile is parabolic, the dynamics of the stability of the flow differ greatly owing to the blockage effect induced by the stationary walls of the plane channel. The effect of blockage on the stability of the flow may also vary depending on the situation, whether the cylinder is confined symmetrically between the plane walls or the cylinder is closer to one of the confining walls i.e. the cylinder is confined asymmetrically. The typical grids used to simulate flow past a cylinder confined symmetrically and asymmetrically in a plane channel are shown in Figure 6.11. The grid sensitivity analysis is done for each case to determine the optimum grid size. The Reynolds number for the flow past a cylinder confined in a rectangular plane channel

is defined in a way that is useful for the comparison of the results with the unbounded flow past a circular cylinder.

$$Re = \frac{d\bar{u}_d \rho}{\mu} \quad (6.1)$$

where  $\bar{u}_d$  is the velocity average over the diameter of the cylinder, given as follows:

$$\bar{u}_d(\beta, \gamma) = \frac{1}{d} \int_{d_2}^{d_1} u_{\max} \left( 1 - \left( \frac{y}{H/2} \right)^2 \right) dy \quad (6.2)$$

where  $d_1$  and  $d_2$  are the y-coordinates of the cylinder and are function of  $\beta$  and  $\gamma$  as given below

$$d_1 = \frac{d}{2\beta} (\gamma(1-\beta) - 1) + d \quad (6.3)$$

$$d_2 = \frac{d}{2\beta} (\gamma(1-\beta) - 1) \quad (6.4)$$

### 6.2.1 Validation of critical $Re$

The transition of flow from steady to unsteady is delayed when the circular cylinder is confined in a plane channel. Chen et al. [23] have determined the critical  $Re$  at which the flow becomes unsteady for  $\beta = 0$  to 0.7 for a symmetrically confined cylinder. In their study, it was shown that the critical  $Re$  increases with increase in  $\beta$  i.e. the transition is delayed with increase in  $\beta$ . The model in the present study has been validated with their results for the critical  $Re$  and  $St$  for  $\beta = 0$  to 0.4 and the results are found to be in good agreement, as shown in Table 6.5. The comparison is also described in Figures 6.12. For determining critical  $Re$ , the flow is disturbed by the rotation of the cylinder as described in section 6.1.1 for unbounded flow and the ensuing time dependent motion is examined to check whether the disturbance is decayed or amplified leading to vortex shedding. Zovatto and Pedrizzetti [24] have determined the critical  $Re$  for a cylinder confined asymmetrically between the plane walls for  $\beta = 0.2$  and  $\gamma = 1$  to 0.125 and the critical  $Re$  was found to increase with the decrease in  $\gamma$ . We have validated our model with their results for critical  $Re$  and the results are in good agreement, as shown in Table 6.6 and Figure 6.13.

### 6.2.2 Variation of critical $Re$ with $\beta$ and $\gamma$

As shown in section 6.2.1, the transition of the flow past a cylinder confined symmetrically in a plane channel is delayed with increase in  $\beta$ . In the present study, the variation of critical  $Re$  with  $\gamma$  for  $\beta = 0.1$  to  $0.4$  is determined using time dependent numerical simulations. Table 6.7 presents the results for the variation of critical  $Re$  with  $\beta$  and  $\gamma$ . While determining the critical  $Re$ ,  $Re$  was increased in steps of 4 in the simulations. Therefore, the difference between the actual critical  $Re$  and the number determined in this study may be around 3. The effect of variation in  $\beta$  and  $\gamma$  on critical  $Re$  is also described in Figure 6.14. As observed from the figure, for a given  $\beta$  the critical  $Re$  increases with decrease in  $\gamma$  implying that the transition of the flow is delayed as the cylinder moves closer to one of the confining walls. It may also be observed from the figure that the critical  $Re$  increases steeply at  $\gamma < 0.5$ . The increase is more pronounced at higher  $\beta$ . For example, at  $\beta = 0.3$ , the critical  $Re$  increases from 120 to 276 as  $\gamma$  decreases from 0.5 to 0.25. This may be attributed to the fact that as the cylinder approaches the wall, the interaction of the boundary layer of the wall with that of the cylinder suppresses the vortex shedding from the cylinder resulting in the stability of the flow. Figure 6.14 also describes the effect of  $\beta$  for a constant  $\gamma$ . The critical  $Re$  increases with increase in  $\beta$  for a given  $\gamma$ , which is in agreement with the general trend observed that the vortex shedding is suppressed with increase in  $\beta$ .

#### 6.2.3 Effect of blockage ratio ( $\beta$ ) on $\bar{C}_D$ , $St$ , $C_L$ and $\bar{Nu}_w$ for a symmetrically confined cylinder

The presence of the stationary walls significantly affects the drag force exerted on the cylinder by the fluid. Table 6.8 presents the effect of increase in  $\beta$  on  $\bar{C}_D$  for different  $Re$  for a cylinder confined symmetrically in the plane channel. The effect is also pictorially depicted in Figure 6.15. As observed from the figure,  $\bar{C}_D$  increases with increase in  $\beta$  from 0 (unbounded flow) to 0.1 for  $Re < 50$ . For  $Re \geq 50$  the effect of increase in  $\beta$  from 0 to 0.1 on  $\bar{C}_D$  is negligible. It may also be observed from the figure that as the value of  $\beta$  increased from 0.1 to 0.4,  $\bar{C}_D$  increases for fixed  $Re$ . The increase in  $\bar{C}_D$  with increase in  $\beta$  is attributed to the fact that as the walls approach closer to the cylinder, the obstruction to the flow increases. Therefore, the velocity gradients become relatively steeper resulting in the higher drag force on the cylinder. However, the increase in  $\bar{C}_D$  is pronounced only at low  $Re$ . The significant increase in  $\bar{C}_D$  is

caused by the large boundary layer thickness at low  $Re$  i.e. the effect of viscous forces extends to larger distance from the cylinder resulting in the interaction with walls.

Table 6.9 and Figure 6.16 presents the effect of increase in  $\beta$  on  $St$ . also illustrates the effect of  $\beta$  on  $St$ . As seen from the figure, for all values of  $\beta$ , except at 0.4,  $St$  increases with increase in  $Re$ , which is in agreement with the general trend. The change in  $St$  as  $\beta$  increases from 0 to 0.2 is negligible for  $Re \leq 300$ , whereas it decreases for  $Re \geq 400$ . For example, at  $Re = 500$  the decrease in  $St$  is 3.7% as  $\beta$  increases from 0 to 0.2. It may also be observed from the figure that as  $\beta$  increases from 0.2 to 0.4,  $St$  increases significantly for a fixed  $Re$ . The increase in  $St$  from  $\beta = 0.2$  to 0.4 at  $Re = 400$  is 31%. For  $\beta = 0.4$ ,  $St$  decreases with increase in  $Re$  from 200 to 300 and then increases with  $Re$ .

Figure 6.17 describes vorticity contours at  $Re = 200$  for various values of  $\beta$ . As seen from the figure, at  $\beta = 0.1$  vortices that are shed from the cylinder are regularly placed and the effect of vortices shed from the walls is negligible on those shed from the cylinder. However, at  $\beta = 0.2$  the dominance of vortices shed from the walls grows. This effect is more pronounced as  $\beta$  increases. At  $\beta = 0.3$  and 0.4, vortices shed from the walls significantly affect the vorticity distribution resulting in the distortion of the symmetric distribution of vortices shed from the cylinder.

Figure 6.18 illustrates the trajectories of  $\bar{C}_D$  and  $C_L$  during one period of oscillation of the alternating vortices. As seen from the figure, the amplitude of oscillation of  $C_L$  decreases with increase in  $\beta$ . The double rings in the trajectories show that the time period of oscillation of  $C_L$  is twice that of  $\bar{C}_D$ . This may also be explained from Figure 6.19 where the trajectory of  $\bar{C}_D$  and  $C_L$  for  $\beta = 0.1$  and the time histories of  $C_D$  and  $C_L$  are plotted over one period. As seen from the figure, from point 1 to point 2  $C_L$  increases and  $C_D$  decreases. At point 2, the reverse in the trend of  $C_D$  takes place whereas  $C_L$  continues to increase upto point 3. From point 3 to 4  $C_D$  and  $C_L$  both decrease. At point 4, the reverse in the trend of  $C_D$  takes place whereas  $C_L$  continues to decrease upto point 5. The frequency of the oscillation of  $C_D$  is twice that of  $C_L$  due to the contribution of upper and lower alternating vortices to the oscillation of  $C_D$ .

The effect of  $\beta$  on  $\bar{Nu}_w$  is illustrated in Table 6.10 and Figure 6.20. It may be observed from the figure that the effect of increase in  $\beta$  from 0 to 0.3 on  $\bar{Nu}_w$  is negligible. As  $\beta$  increases

from 0.3 to 0.4,  $\overline{Nu}_w$  increases. For example, at  $Re = 100$  increase in  $\overline{Nu}_w$  is 7.78%, corresponding to increase in  $\beta$  from 0.3 to 0.4.

#### 6.2.4 Effect of gap ratio ( $\gamma$ ) on $\overline{C}_D$ for an asymmetrically confined cylinder

As shown in section 6.2.3, the presence of stationary walls significantly affects the drag force exerted by fluid on a cylinder confined symmetrically in the plane channel. Furthermore, when the cylinder is confined asymmetrically in the plane channel, the dynamics of flow differs due to the presence of stationary wall closer to the cylinder surface. Tables 6.11-6.14 present the effect of decrease in  $\gamma$  on  $\overline{C}_D$  for  $\beta = 0.1, 0.2, 0.3$ , and  $0.4$  respectively. Figure 6.21 also describes the effect of  $\gamma$  on  $\overline{C}_D$ . As observed from the figure, at  $\beta = 0.1$  as  $\gamma$  decreases i.e. the cylinder approaches one of the confining walls for fixed  $Re$ ,  $\overline{C}_D$  increases. Change in  $\overline{C}_D$  is negligible as  $\gamma$  decreases from 1 to 0.75, except at  $Re = 1000$  where  $\overline{C}_D$  decreases by 12%. For fixed  $Re < 200$ ,  $\overline{C}_D$  increases as  $\gamma$  decreases from 0.75 to 0.25 and the change in  $\overline{C}_D$  is negligible at  $Re \geq 200$ . For example, at  $Re = 20$  increase in  $\overline{C}_D$  is 21% as  $\gamma$  decreases from 0.75 to 0.25. For  $\beta = 0.1$ , the effect of decrease in  $\gamma$  on  $\overline{C}_D$  is more pronounced only at low  $Re$  and the effect vanishes at  $Re \geq 200$ .

It may also be observed from the figure that for  $\beta = 0.2, 0.3$ , and  $0.4$  drag coefficient increases with decrease in  $\gamma$ . At higher  $Re$  and higher blockage ratios increase in  $\overline{C}_D$  as  $\gamma$  decreases from 1 to 0.25 is large. For example at  $\beta = 0.1$  and  $Re = 100$  increase in  $\overline{C}_D$  as  $\gamma$  decreases from 1 to 0.25 is 8%, whereas at  $\beta = 0.4$  increase in  $\overline{C}_D$  is 38%. Increase in  $\overline{C}_D$  as the cylinder approaches closer to one of the confining walls is attributed to increase in the resistance to the flow. When the cylinder is present closer to the wall, the gap between the cylinder and the wall is filled by the boundary layers of the cylinder and wall where viscous forces are dominant. In this case the viscous and pressure forces exerted on the cylinder increase resulting in increase in the total drag coefficient. The significant increase in  $\overline{C}_D$  at low  $Re$  is due to the large boundary layer thickness.

Figures 6.22 and 6.23 illustrate the effect of  $\gamma$  on  $C_{DP}$  and  $C_{DF}$  for  $\beta = 0.1, 0.2, 0.3$ , and  $0.4$  in the steady flow range. As seen from the figures,  $C_{DP}$  and  $C_{DF}$  increase with decrease in  $\gamma$ .

for fixed  $Re$  at each  $\beta$ . However, increase in  $C_{DF}$  is higher than increase in  $C_{DP}$  at  $\beta = 0.1$ , whereas for  $\beta = 0.2, 0.3$ , and  $0.4$  increase in  $C_{DP}$  is higher than increase in  $C_{DF}$ . For example, at  $Re = 20$  and  $\beta = 0.1$  increase in  $C_{DF}$  is 85% whereas increase in  $C_{DP}$  is only 7% as  $\gamma$  decreases from 1 to 0.25 and at  $Re = 20$  and  $\beta = 0.2$  increase in  $C_{DP}$  is 69%, whereas increase in  $C_{DF}$  is only 12%.

#### 6.2.5 Effect of gap ratio ( $\gamma$ ) on vortex shedding from an asymmetrically confined cylinder

As shown in section 6.2.3, the presence of the stationary walls significantly affects  $St$  for a cylinder confined symmetrically in the plane channel. The asymmetric confinement of the cylinder in a plane channel also considerably affects  $St$ . Tables 6.15 - 6.18 present the effect of decrease in  $\gamma$  on  $St$  for various values of  $\beta$ . The effect of  $\gamma$  on  $St$  is illustrated in Figure 6.24. As seen from the figure, for a given  $\beta$  and  $Re$ ,  $St$  increases with decrease in  $\gamma$ . At  $\beta = 0.1$ , increase in  $St$  at  $Re = 200$  is 14.3% as  $\gamma$  decreases from 1 to 0.25. It may also be observed from the figure that for a fixed  $\gamma$  and  $Re$ ,  $St$  increases with increase in  $\beta$ .

Figure 6.25 illustrates the effect of  $\beta$  and  $\gamma$  on vortex shedding from the cylinder at  $Re = 200$ . In the figure the instantaneous vorticity contours are presented to show the effect of asymmetrical confinement of the cylinder on vortex shedding. For the simulation purpose  $\beta$  is varied from 0.1 to 0.4 and  $\gamma$  from 1 to 0.25. As observed from the figure, at  $\beta = 0.1$ , when the cylinder is symmetrically confined in the plane channel, the vortex street consists of positive (shed from the bottom) and negative (shed from the top) vortices shed from the cylinder, which are regularly placed. As the cylinder approaches one of the confining walls the regular structure of the vortices is distorted. The distortion is caused by the presence of the wall close to the cylinder in which case the vortices shed from the wall begins to interfere with that from the cylinder. It may also be observed from the figure that at  $\beta = 0.1$  and  $\gamma = 1$  the vortex structure consists of double row of vortices shed from the cylinder. However, at  $\gamma = 0.75$ , the positive vortices shed from the cylinder are significantly distorted due to the effect of vortices shed from the wall which results in the formation of vortex street with a single row of vortices. As observed from the figure, at  $\gamma = 0.75$  the vortex street consists of double row of vortices but the positive vortices shed from the cylinder are weaker. At  $\gamma = 0.75$  and 0.25, the effect is more pronounced with weak positive vortices shed from the bottom side of the cylinder. In this case the vortex street has almost become a single row of vortices.

The above phenomenon may also be explained by the trajectories of  $C_L - C_D$  over one period of the unsteady periodic state, as shown in Figure 6.26 for  $\beta = 0.1$  and  $Re = 200$ . The double ring in the trajectories is due to the fact that the frequency of the drag coefficient is twice that of the lift coefficient. Re-referring Figure 6.19, this in turn is due to the simultaneous contribution of the negative and positive vortices shed from the cylinder to the drag. The phenomenon of the formation the double ring has been explained in section 6.2.3. As observed from Figure 6.26, at  $\gamma = 1$ , i.e. when the cylinder is confined symmetrically in the plane channel, the lift coefficient oscillates symmetrically about zero with an amplitude of  $\pm 0.64$ . The mean lift coefficient in this case is zero. However, at larger values of  $\gamma$  (0.75, 0.5 and 0.25) the oscillations in the values of the lift coefficient are not symmetric about zero. Therefore, the mean lift coefficient has a non-zero value in the asymmetrically confined case. Due to the relatively larger amplitude of the oscillations in the lift coefficient in the negative direction the mean lift coefficient is negative. It may also be observed from the figure that the amplitude of the lift coefficient increases in the negative direction and decreases in the positive direction as the cylinder moves closer to the bottom wall of the plane channel. This phenomenon is directly related to the shedding of the negative and positive vortices from the cylinder. The double ring in the trajectories of  $C_L - C_D$  gradually begins to collapse into a single ring as the cylinder moves closer to the wall, as seen in the figure for  $\beta = 0.1$  in the case of  $\gamma = 0.25$ .

Figure 6.25 illustrates the effect of decrease in  $\gamma$  on the vortex shedding from the cylinder for  $\beta = 0.2$  at  $Re = 200$ . As seen from the figure, when the cylinder is symmetrically confined in the plane channel, the structure of vortex street is well defined, with regularly placed positive and negative vortices. However, when compared to the symmetrically confined case at  $\beta = 0.1$ , the vortex shedding structure is relatively irregular. It may also be observed from the figure that as the cylinder approaches one of the confining walls the double row of vortices converges to single row of vortices. At  $\gamma = 0.125$ , i.e. when the cylinder is present very close to the bottom wall, the vortex shedding is completely suppressed.

Figure 6.27 describes the suppression of vortex shedding from the cylinder in which the trajectories of  $C_L - C_D$  for  $\beta = 0.2$  at various gap ratios are shown. As seen from the figure the amplitude of  $C_L$  in the negative direction becomes relatively larger as the cylinder moves closer to the wall. At  $\gamma = 0.125$ , the trajectory reduces to a point with a positive lift. In such case the lift

and drag coefficients are constant and are not fluctuating with time, indicating that the vortex shedding from the cylinder is completely suppressed.

Re-referring Figure 6.25, the vortex shedding is gradually suppressed as the cylinder approaches one of the confining walls at  $\beta = 0.3$  and  $0.4$ . As seen from the figure at  $\gamma = 0.25$  vortex shedding from the cylinder is completely suppressed in both the cases. The corresponding trajectories of  $C_L - C_D$  at  $\beta = 0.3$  and  $0.4$  are shown in Figures 6.28 and 6.29. These trajectories also confirm the suppression of vortex shedding from the cylinder. Figure 6.30 illustrates the effect of  $\gamma$  on  $\bar{C}_L$  for various blockage ratios. As observed from the figure, for fixed  $Re$ ,  $\bar{C}_L$  decreases as  $\gamma$  decreases. The trend is reversed when the cylinder is present sufficiently close to the cylinder which is observed for  $\beta = 0.2, 0.3$  and  $0.4$ . At  $\beta = 0.1$ , the cylinder is not present sufficiently close to the cylinder so as to results in the mean positive lift. The unsteady vorticity contours at  $Re = 200$  for  $\beta = 0.3$  at various  $\gamma$  are shown in Figure 6.31. The steady nature of the flow at  $\gamma = 0.25$  is evident from the figure.

#### 6.2.6 Effect of gap ratio ( $\gamma$ ) on $\bar{Nu}_w$ for an asymmetrically confined cylinder

Tables 6.19 - 6.22 present the effect of decrease in  $\gamma$  on  $\bar{Nu}_w$  for  $\beta = 0.1, 0.2, 0.3$ , and  $0.4$ , respectively. Figure 6.32 also describes the effect of  $\gamma$  on  $\bar{Nu}_w$ . It may be observed from the figure that the effect of decrease in  $\gamma$  on  $\bar{Nu}_w$  is negligible for all blockage ratios. The variation of local  $Nu_w$  on the surface of the cylinder with that in the gap ratio is described in Figure 6.33. As observed from the figure, at each blockage ratio change in the distribution of local  $Nu_w$  on the surface of the cylinder is negligible with decrease in  $\gamma$ , except some distortion in the distribution when the cylinder is present very close to the bottom wall. The distortion is more pronounced at high blockage ratios. However, change in the surface averaged  $Nu_w$  is negligible with decrease in  $\gamma$  for each blockage ratio.

### 6.3 The transition of flow past a circular cylinder from 2-D to 3-D in unbounded domain

As discussed earlier, the flow past a circular cylinder in unbounded domain loses stability around  $Re = 47$ , leading to periodic vortex shedding. If  $Re$  is increased to 180 flow transition takes from 2-D to 3-D with a complex wake structure. Williamson [50] has investigated experimentally the discontinuities in  $St-Re$  curve in the range of  $Re$  from 49 to 178. The author

has concluded that the discontinuities in  $St$ - $Re$  curve are caused by the three dimensional transition in the wake of the cylinder due to the change in oblique vortex shedding modes. The ‘Quasi-periodic’ mode that exists for  $Re < 64$  consists of regions of different frequencies along the span of the cylinder. In this mode the central region of higher frequency ( $f_U$ ) are sandwiched between two regions of lower frequency ( $f_L$ ). When  $Re$  is increased above 64, shedding mode changes to ‘Periodic’ oblique shedding mode, which consists of the regions of lower frequency along the entire span with a ‘chevron’- shaped pattern. In both of the shedding modes there are end regions of lower frequency ( $f_e$ ) that are significantly affected by the end conditions of the cylinder. It was also shown that the end regions merge together covering the whole span if the aspect ratio (L/D) of the cylinder is less than 28. By manipulating the end conditions of the cylinder, the parallel mode of vortex shedding was observed which indicates that indeed there exists a universal  $St$ - $Re$  curve without discontinuities. The relation between  $St$  for the parallel and oblique shedding modes was given as  $S_o = S_0/\cos \theta$ , where  $S_o$  and  $S_0$  are *Strouhal numbers* for parallel and oblique ( $\theta$ ) shedding modes respectively.

The existence of two successive transitions in the transition of the flow past a cylinder to three-dimensionality was also observed by Williamson [51]. The first discontinuity that exists between  $Re$  of 170-180 is called Mode A, which has large spanwise wave lengths of 3-4 diameters and scales to the larger physical structure in the flow i.e. the primary vortex core. The second discontinuity appears between  $Re$  of 230-260 is called Mode B, which has small wavelength of around 1 diameter and scales to the smaller physical structure of the flow i.e. the braid shear layer. In these modes, vortex dislocation occurs resulting in the three-dimensionality of the flow. It was observed by Prasad and Williamson [52] that vortex shedding control is possible by manipulating the end conditions of the cylinder, except in the transition region 190-260 which is marked by vortex dislocations.

In the present study, we have carried out 3-D numerical simulation to characterize the discontinuities in  $St$ - $Re$  relationship and vortex dislocation. The geometry used to simulate 3-D unbounded flow past a circular cylinder, described schematically in Figure 3.2, is a rectangular brick of dimensions  $28d$ ,  $16d$  and  $2.25d$  in x, y and z-directions, respectively, where  $d$  is the diameter of the cylinder. The cylinder is assumed to be located at  $10d$  and  $18d$  from the inlet and outlet, respectively. The fluid enters at the plane  $ABCD$  with a uniform velocity  $U_x$  and leaves at the plane  $EFGH$ . The typical mesh configuration used for 3-D simulation is shown in Figure

6.34. The grid independence test is carried out on this geometry as shown in Table 6.23. As observed from the table, change in  $\bar{C}_D$  as the number of cells is increased from 282,000 to 663,000 is below 2%. Therefore, the grid with 282,000 cells was chosen as the optimum grid. The comparison of  $\bar{C}_D$  and  $St$  values with the values reported in the literature is presented in Table 6.24. The maximum deviation in  $\bar{C}_D$  values from the values reported in the literature is 11% at  $Re = 100$ . The values of  $St$  are matching well with the published data with a maximum deviation of 9% at  $Re = 100$ .

A coarser grid size with 133,000 cells is also used to simulate 3-D flow past a cylinder to save computational time. The corresponding results obtained using this grid are presented in Table 6.25. In order to characterize the three dimensionality of the flow, the  $St-Re$  curves for 2-D flow and 3-D flow are compared in Figure 6.35. The results obtained using both coarser and finer grid are shown in the figure. In the case of finer grid the discontinuity in  $St-Re$  was found at  $Re = 300$ , whereas in the case of relatively coarser grid the  $St-Re$  curve lies below the  $St-Re$  curve for the 2-D Flow case. The  $St-Re$  curve obtained using coarser grid is in accordance with the observation of Williamson [50] that the end regions of lower frequency merge together covering the whole span if the aspect ratio ( $L/D$ ) of the cylinder is less than 28. However, when finer mesh is used the Mode A discontinuity was not observed, rather Mode B discontinuity was observed at  $Re = 300$ .

The normalized velocity plots for  $Re = 100$  along the span of the cylinder in z-direction at 2D and 5D downstream locations are shown in Figure 6.36. As seen from the figure, at both the downstream locations the velocity profiles along the span of the cylinder are essentially the same. There is no variation in the velocity profiles in z-direction. Therefore, the flow at  $Re = 100$  is 2-D in nature. The normalized velocity profiles for  $Re = 200$  are described in Figure 6.37. As observed from the figure the flow at  $Re = 200$  is 2-D in nature. However, as observed by Williamson [51], the flow at  $Re = 200$  is 3-D. The discrepancy may due to the small aspect ratio ( $L/D = 2.25$ ) used in this study. The normalized velocity plots at  $Re = 300$  are shown in Figure 6.38. The 3-D nature of the flow is clearly evident from the figure, which shows considerable variation in profiles in z-direction. The low aspect ratio ( $L/D = 2.25$ ) used in this study is found to be inadequate to predict the discontinuities in  $St-Re$  curve. Hence, high aspect ratio has to be used to predict the three-dimensional transition in the cylinder wake, which requires large amount of computational resources and time.

Rotational speed ( $\Omega$ ) rad/sec	$\bar{C}_D$	$C_L$	$St$
2	1.303	$\pm 0.285$	0.1608
6	1.303	$\pm 0.283$	0.1608

**Table 6.1: The effect of the disturbance (rotational speed) on  $\bar{C}_D$ ,  $C_L$ , and  $St$  at  $Re = 100$**

Upwinding Scheme	$Re_c$	$Re_c$ Jackson (1987)
First order	100	-
Second order	50	46
QUICK	50	-

**Table 6.2: Comparison of critical  $Re$  observed from various upwinding schemes**

S.No	$Re$	$\bar{C}_D$			
		QUICK	First order	Second order	Braza et al. (1986)
1	40	1.5124	1.6086	1.5022	1.45
2	50	1.3970	1.5225	1.3936	1.40
3	100	1.3059	1.2425	1.3027	1.253
4	200	1.3010	1.1747	1.2981	1.321
5	500	1.3258	1.1551	1.3814	-
6	1000	1.4741	1.189	1.4734	1.198

**Table 6.3: Comparison of  $\bar{C}_D$  values calculated from different upwinding schemes**

S.No	$Re$	$St$			
		QUICK	First order	Second order	Braza et al. (1986)
1	50	0.1182	Steady State	0.1212	0.1200
2	100	0.1605	0.1193	0.1600	0.165
3	200	0.1911	0.1442	0.1912	0.198
4	500	0.2081	0.1627	0.2222	-
5	1000	0.2376	0.1731	0.2370	0.22

Table 6.4: Comparison of  $St$  values calculated from different upwinding schemes

S.No	$\beta$	$Re_C$		$St$	
		This work	Chen et al. (1995)	This work	Chen et al. (1995)
1	0	50	47.9	0.121	0.138
2	0.1	50	51.6	0.120	0.122
3	0.2	69	69	0.158	0.158
4	0.3	92	92	0.214	0.215
5	0.4	110	110.1	0.287	0.286

Table 6.5: Comparison of  $Re_C$  and  $St$  values at various blockage ratios

S.No	$\gamma$	$Re_C$	
		This work	Zovatto and Pedrizzetti (2001)
1	1	69	68
2	0.587	72	75
3	0.375	108	110
4	0.125	300	300

Table 6.6: Comparison of  $Re_C$  values for various  $\gamma$  ( $\beta=0.2$ )

S.No	Gap ratio $\gamma$	$Re_C$		
		$\beta = 0.1$	0.3	0.4
1	1	50	92	110
2	0.75	55	96	120
3	0.5	65	120	156
4	0.25	90	276	400-500

Table 6.7: Variation of  $Re_C$  with  $\beta$  and  $\gamma$

S.No	$Re$	$\bar{C}_D$			
		$\beta = 0.1$	0.2	0.3	0.4
1	10	3.127	4.175	-	-
2	20	2.157	2.671	3.759	-
3	30	1.78	2.142	-	-
4	40	1.567	1.860	2.47	3.643
5	50	1.426	1.681	-	-
6	60	-	1.5563	2.030	2.914
7	80	-	-	1.796	2.543
8	100	1.296	-	1.650	2.314
9	110	-	-	-	2.229
10	200	1.290	1.253	1.421	1.858
11	300	1.321	1.268	1.391	1.733
12	400	1.338	1.274	1.384	1.688
13	500	1.340	1.324	1.385	1.658
14	1000	1.400	1.368	1.403	1.612

Table 6.8: Effect of blockage ratio ( $\beta$ ) on  $\bar{C}_D$  for  $\gamma = 1$  (symmetrical case)

S.No	Re	St			
		$\beta = 0.1$	0.2	0.3	0.4
1	50	0.1210	Steady	Steady	Steady
4	100	0.1608	-	0.2175	Steady
5	110	-	-	-	0.2870
6	200	0.1914	0.1922	0.2260	0.2946
7	300	0.2046	0.2028	0.2251	0.2721
8	400	0.2100	0.2054	0.2279	0.2702
9	500	0.2183	0.2140	0.2351	0.2725
10	1000	0.2330	0.2261	0.2466	0.2885

Table 6.9: Effect of blockage ratio ( $\beta$ ) on  $St$  for  $\gamma = 1$ (symmetrical condition)

S.No	Re	$\overline{Nu}_w$			
		$\beta = 0.1$	0.2	0.3	0.4
1	10	1.930	2.063	-	-
2	20	2.526	2.667	2.873	-
3	30	2.969	3.119	-	-
4	40	3.337	3.497	3.732	4.064
5	50	3.660	3.830	-	-
6	60	-	4.135	4.385	4.751
7	80	-	-	4.948	5.345
8	100	5.219	-	5.455	5.880
9	200	7.596	7.592	7.7253	8.1813
10	300	9.493	9.326	9.4953	10.0998
11	400	11.011	10.916	10.9416	11.5889
12	500	12.402	12.131	12.1821	12.7945
13	1000	17.300	18.980	17.9611	18.4201

Table 6.10: Effect of blockage ratio ( $\beta$ ) on  $\overline{Nu}_w$  for  $\gamma = 1$ (symmetrical case)

S.No	Re	$\bar{C}_D$			
		$\gamma = 1$	0.75	0.5	0.25
1	10	3.127	3.128	3.258	3.800
2	20	2.157	2.158	2.249	2.622
3	30	1.780	1.782	1.860	2.156
4	40	1.567	1.570	1.643	1.900
5	50	1.426	1.431	1.500	1.734
6	100	1.296	1.282	1.302	1.400
7	200	1.290	1.267	1.270	1.325
8	300	1.321	1.300	1.290	1.323
9	400	1.338	1.328	1.303	1.318
10	500	1.340	1.321	1.309	1.300
11	1000	1.400	1.229	1.237	1.239

Table 6.11: Effect of gap ratio ( $\gamma$ ) on  $\bar{C}_D$  for  $\beta = 0.1$

S.No	Re	$\bar{C}_D$			
		$\gamma = 1$	0.875	0.375	0.125
1	10	4.175	4.197	4.642	5.549
2	20	2.671	2.686	3.149	3.918
3	30	2.142	2.154	2.556	3.290
4	40	1.860	1.871	2.222	2.940
5	50	1.681	1.691	2.005	2.714
6	60	1.556	1.564	1.852	2.550
7	200	1.253	1.2573	1.333	1.750
8	300	1.268	1.2676	1.318	1.586
9	400	1.274	1.2856	1.380	1.609
10	500	1.324	1.300	1.380	1.606
11	1000	1.368	1.400	1.4305	1.897

Table 6.12: Effect of gap ratio ( $\gamma$ ) on  $\bar{C}_D$  for  $\beta = 0.2$

S.No	$Re$	$\bar{C}_D$			
		$\gamma = 1$	0.75	0.5	0.25
1	20	3.759	3.853	4.142	-
2	40	2.476	2.540	2.820	2.726
3	60	2.030	2.079	2.308	2.330
4	80	1.796	1.836	2.033	2.098
5	100	1.650	1.682	1.859	1.940
6	200	1.421	1.438	1.547	1.516
7	300	1.391	1.404	1.484	1.399
8	400	1.384	1.396	1.452	1.352
9	500	1.385	1.393	1.435	1.323
10	1000	1.403	1.397	1.395	1.266

Table 6.13: Effect of gap ratio ( $\gamma$ ) on  $\bar{C}_D$  for  $\beta = 0.3$

S.No	$Re$	$\bar{C}_D$			
		$\gamma = 1$	0.75	0.5	0.25
1	40	3.643	3.761	4.1253	4.390
2	60	2.914	3.004	3.3468	3.779
3	80	2.543	2.618	2.9173	3.434
4	100	2.314	2.381	2.6482	3.204
5	110	2.229	2.292	-	-
6	120	-	2.218	2.463	3.026
7	200	1.858	1.904	2.098	2.5716
8	300	1.733	1.748	1.9241	2.3044
9	400	1.688	1.683	1.8363	2.1714
10	500	1.658	1.658	1.7974	2.0868
11	1000	1.612	1.620	1.7356	1.8986

Table 6.14: Effect of gap ratio ( $\gamma$ ) on  $\bar{C}_D$  for  $\beta = 0.4$

S.No	Re	St			
		$\gamma = 1$	0.75	0.5	0.25
1	50	0.1210	Steady	Steady	Steady
2	55	-	0.1273	Steady	Steady
3	100	0.1608	0.1610	0.1660	0.1973
4	200	0.1914	0.1883	0.1930	0.2188
5	300	0.2046	0.2023	0.2055	0.2233
6	400	0.2100	0.2120	0.2108	0.2266
7	500	0.2183	0.2170	0.2170	0.2287
8	1000	0.2330	0.2377	0.2380	0.2440

Table 6.15: Effect of gap ratio ( $\gamma$ ) on St for  $\beta = 0.1$

S.No	Re	St			
		$\gamma = 1$	0.875	0.375	0.125
1	69	0.1589	Steady	Steady	Steady
2	72	-	0.1614	Steady	Steady
3	108	-	-	0.2142	Steady
4	200	0.1922	0.1942	0.2346	Steady
5	300	0.2028	0.2051	0.2349	0.3063
6	400	0.2054	0.2114	0.2361	0.2938
7	500	0.2140	0.2148	0.2377	0.2608
8	1000	0.2261	0.2268	0.2300	0.2843

Table 6.16: Effect of gap ratio ( $\gamma$ ) on St for  $\beta = 0.2$

S.No	Re	St			
		$\gamma = 1$	0.75	0.5	0.25
1	100	0.2175	0.2205	Steady	Steady
2	200	0.2260	0.2341	0.2563	Steady
3	300	0.2251	0.2320	0.2527	0.26388
4	400	0.2279	0.2330	0.2488	0.27037
5	500	0.2351	0.2358	0.2483	0.26979
6	1000	0.2466	0.2460	0.2555	0.27097

Table 6.17: Effect of gap ratio ( $\gamma$ ) on St for  $\beta = 0.3$

S.No	Re	St		
		$\gamma = 1$	0.75	0.5
1	110	0.287	Steady	Steady
2	120	-	0.2852	Steady
4	200	0.2946	0.3006	0.3089
5	300	0.2721	0.2791	0.3113
6	400	0.2702	0.2684	0.3058
7	500	0.2725	0.2687	0.3046
8	1000	0.2885	0.2790	0.2926

Table 6.18: Effect of gap ratio ( $\gamma$ ) on St for  $\beta = 0.4$

S.No	Re	$\overline{Nu}_w$			
		$\gamma = 1$	0.75	0.5	0.25
1	10	1.930	1.9281	1.9421	1.9039
2	20	2.526	2.525	2.5501	2.629
3	30	2.969	2.9686	3.0014	3.1107
4	40	3.337	3.3365	3.3756	3.5038
5	50	3.660	3.6598	3.70433	3.8478
6	100	5.219	5.2077	5.2271	5.2927
7	200	7.596	7.5405	7.6368	7.7468
8	300	9.493	9.3808	9.3426	9.4156
9	400	11.011	10.935	10.904	11.105
10	500	12.402	12.1702	12.212	12.6958
11	1000	17.300	18.291	18.005	18.6624

Table 6.19: Effect of gap ratio ( $\gamma$ ) on  $\overline{Nu}_w$  for  $\beta=0.1$

S.No	Re	$\overline{Nu}_w$			
		$\gamma = 1$	0.875	0.375	0.125
1	10	2.063	2.064	2.093	2.755
2	20	2.667	2.670	2.706	3.126
3	30	3.119	3.123	3.205	3.435
4	40	3.497	3.501	3.609	3.719
5	50	3.830	3.835	3.956	3.994
6	60	4.135	4.140	4.269	4.268
8	200	7.592	7.601	7.615	7.520
9	300	9.326	9.354	9.452	9.673
10	400	10.916	10.839	11.237	11.415
11	500	12.131	12.088	12.647	13.209
12	1000	18.980	17.927	19.336	20.540

Table 6.20: Effect of gap ratio ( $\gamma$ ) on  $\overline{Nu}_w$  for  $\beta=0.2$

S.No	Re	$\overline{Nu}_w$			
		$\gamma = 1$	0.75	0.5	0.25
1	20	2.873	2.880	2.861	-
2	40	3.7385	3.747	3.786	3.610
3	60	4.385	4.404	4.461	4.204
4	80	4.948	4.969	5.033	4.765
5	100	5.455	5.478	5.546	5.270
6	200	7.725	7.759	7.759	7.281
7	300	9.495	9.609	9.595	9.000
8	400	10.941	11.172	11.085	10.561
9	500	12.182	12.245	12.413	11.922
10	1000	17.961	17.823	18.207	16.560

Table 6.21: Effect of gap ratio ( $\gamma$ ) on  $\overline{Nu}_w$  for  $\beta = 0.3$

S.No	Re	$\overline{Nu}_w$			
		$\gamma = 1$	0.75	0.5	0.25
1	40	4.064	4.069	4.035	4.160
2	60	4.751	4.762	4.773	4.697
3	80	5.345	5.358	5.387	5.220
4	100	5.880	5.895	5.937	5.732
5	110	-	6.145	-	-
6	120	-	6.388	6.441	6.223
7	200	8.181	8.173	8.263	7.993
8	300	10.099	10.076	10.236	9.716
9	400	11.588	11.730	11.711	11.156
10	500	12.794	12.903	13.181	12.492
11	1000	18.420	18.217	18.352	17.751

Table 6.22: Effect of gap ratio ( $\gamma$ ) on  $\overline{Nu}_w$  for  $\beta = 0.4$

Re	$\bar{C}_D$			$St$			$\bar{C}_D$ Persillon and Braza (1998)	$St$ Persillon and Braza (1998)
	GRID1	GRID2	GRID3	GRID1	GRID2	GRID3		
100	1.386	1.391	1.394	0.168	0.167	0.168	1.240	0.164
200	1.371	1.390	1.369	0.195	0.193	0.197	1.306	0.181
500	1.259	1.264	1.284	0.199	0.201	0.201	-	-

**Table 6.23: Grid independence test for 3-D flow past a cylinder in unbounded domain**

GRID1: 282,000 cells with 96 intervals on the surface of the cylinder.

GRID2: 461,000 cells with 120 intervals on the surface of the cylinder.

GRID3: 663,000 cells with 120 intervals on the surface of the cylinder.

S.No	Re	$\bar{C}_D$			$St$		
		This work	Persillon and Braza (1998)	Zhang et.al. (1998)	This work	Persillon and Braza (1998)	Zhang et.al. (1998)
1	100	1.386	1.240	1.32	0.168	0.164	0.154
2	200	1.371	1.306	1.28	0.195	0.181	0.190
3	220	1.373	1.313	-	0.199	0.184	-
4	300	1.366	1.366	-	0.199	0.206	-
5	400	1.375	-	-	-	-	-
6	500	1.259	-	-	0.199	-	-

**Table 6.24:  $\bar{C}_D$  and  $St$  for 3-D flow past a cylinder using GRID2**

S.No	Re	$\bar{C}_D$		$St$	
		This work	Persillon and Braza (1998)	This work	Persillon and Braza (1998)
1	50	1.595	-	Steady	-
2	100	1.336	1.240	0.147	0.164
3	150	1.266	-	0.156	0.175
4	180	1.239	-	0.159	0.178
5	200	1.241	1.306	0.165	0.181
6	250	1.180	1.343	0.166	0.186
7	300	1.123	1.366	0.170	0.206

**Table 6.25:  $\bar{C}_D$  and  $St$  for 3-D flow past a cylinder obtained using coarser grid (133,000 cells)**

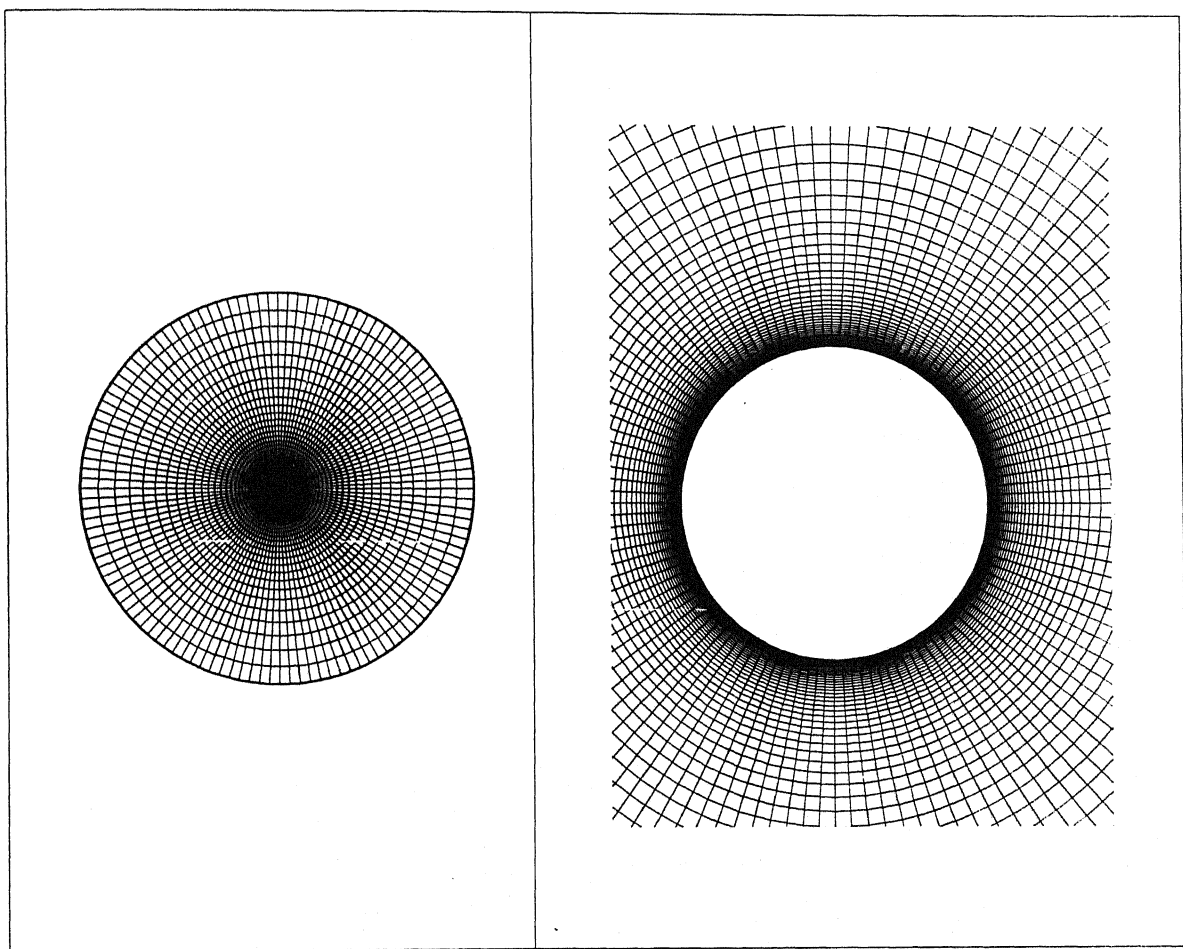


Figure 6.1: Typical mesh configuration used to simulate flow past a cylinder in unbounded domain ( $R/r = 140$ )

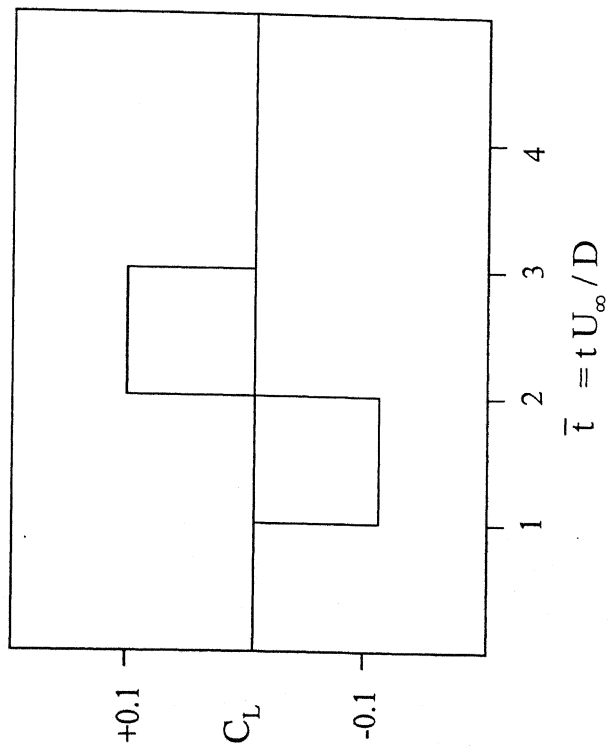
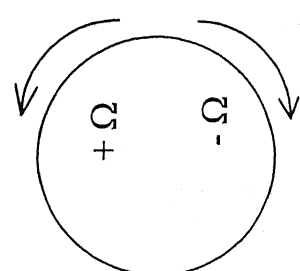


Figure 6.2: Schematic of the rotation of the circular cylinder



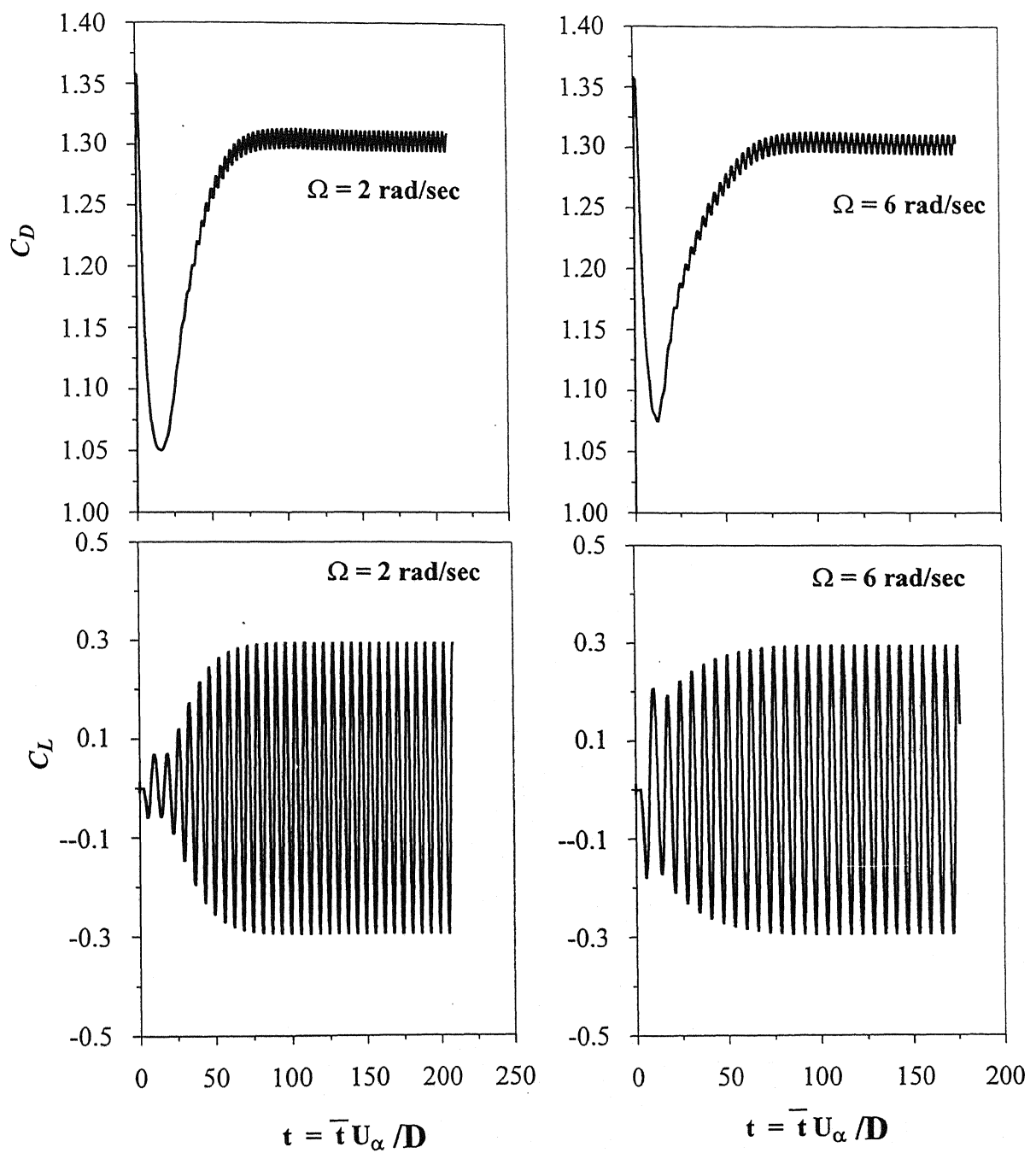
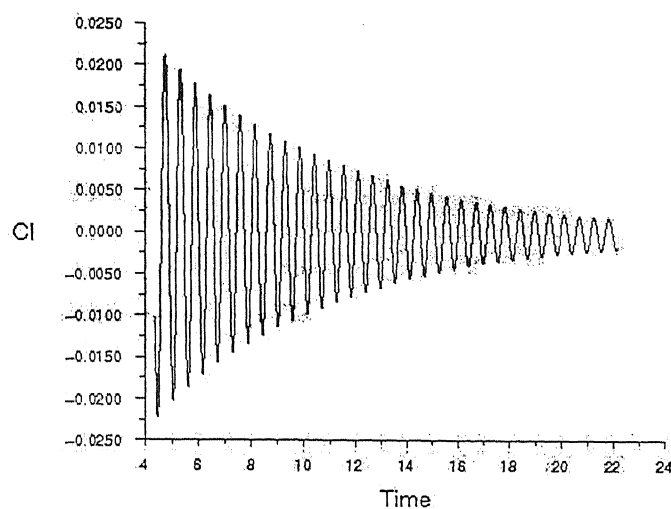
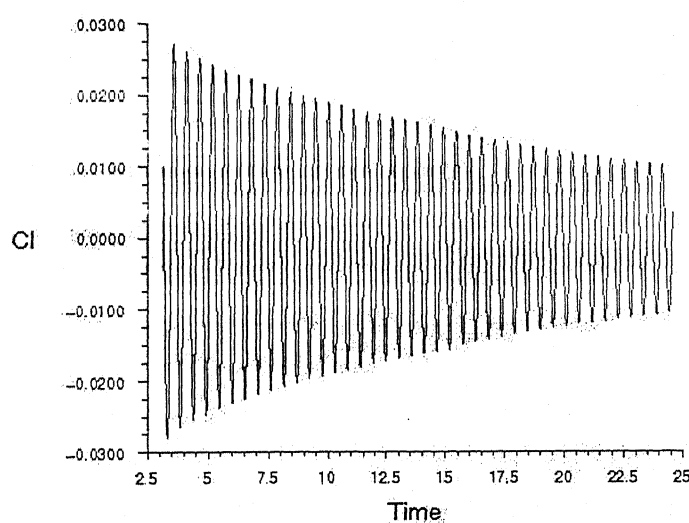


Figure 6.3:  $C_D$  and  $C_L$  time histories for  $Re = 100$



Lift Convergence History (Time=2.2176e+01) Jun 12, 2004  
FLUENT 6.0 (2d, dp, segregated, lam, unsteady)



Lift Convergence History (Time=2.4618e+01) Jun 10, 2004  
FLUENT 6.0 (2d, dp, segregated, lam, unsteady)

**Figure 6.4:  $C_L$  vs time for  $Re = 48$  and  $50$  using second order upwinding scheme**

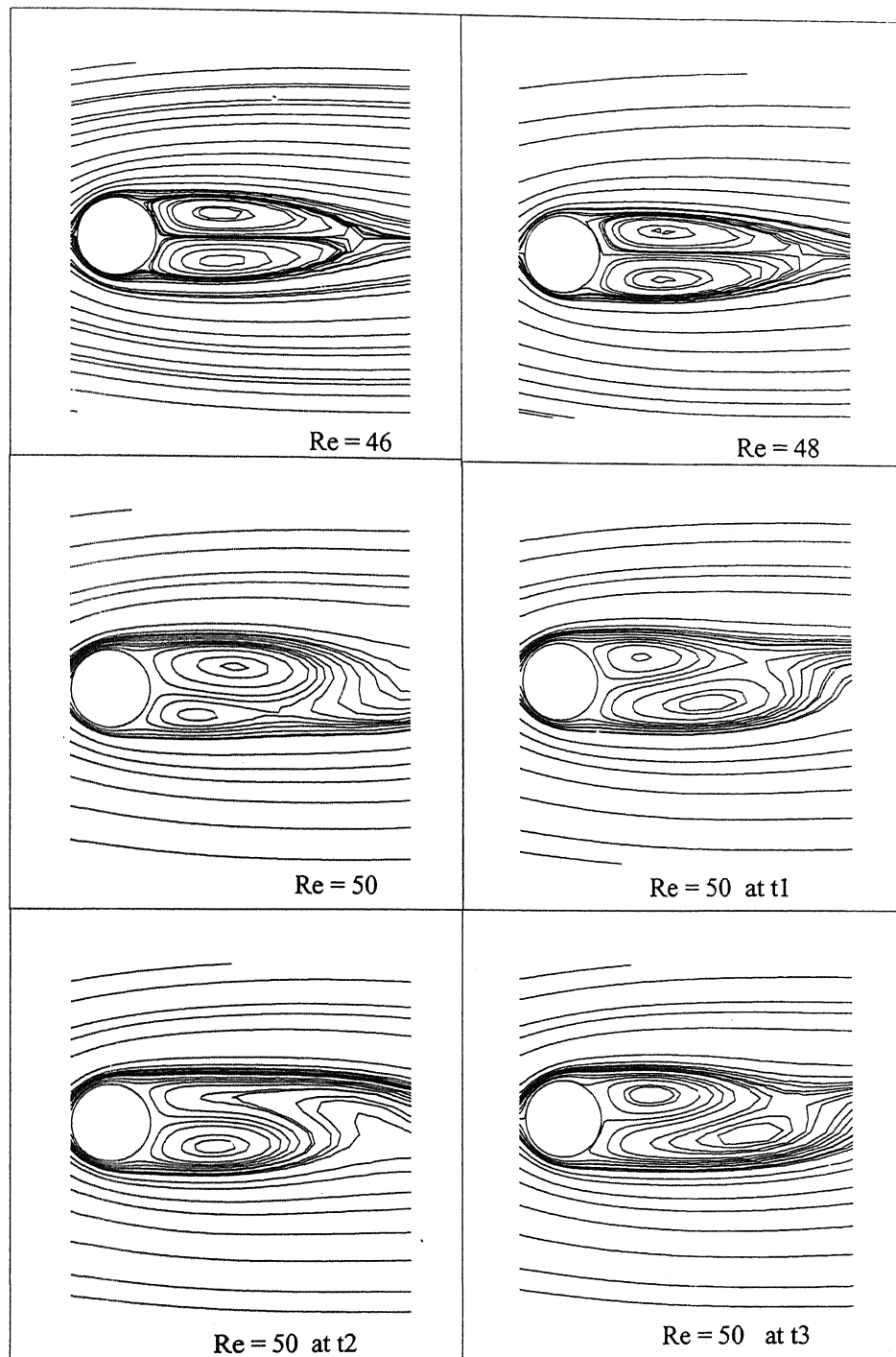
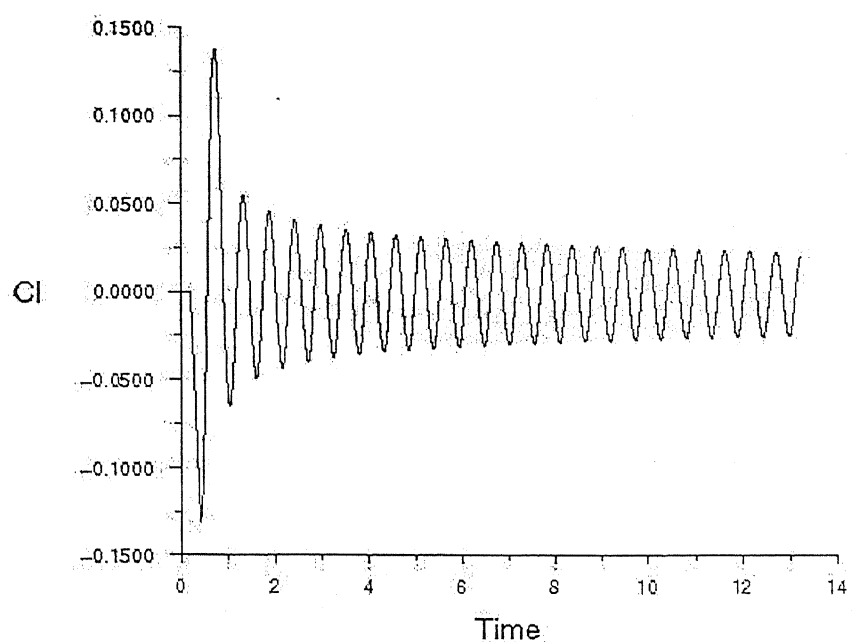


**Figure 6.5: Streamline plots at  $Re = 46, 48$  and  $50$  for second order upwinding scheme**



Lift Convergence History (Time=1.3222e+01)

Aug 13, 2004  
FLUENT 6.0 (2d, dp, segregated, lam, unsteady)

Figure 6.6:  $C_L$  vs time for  $Re = 50$  using QUICK scheme

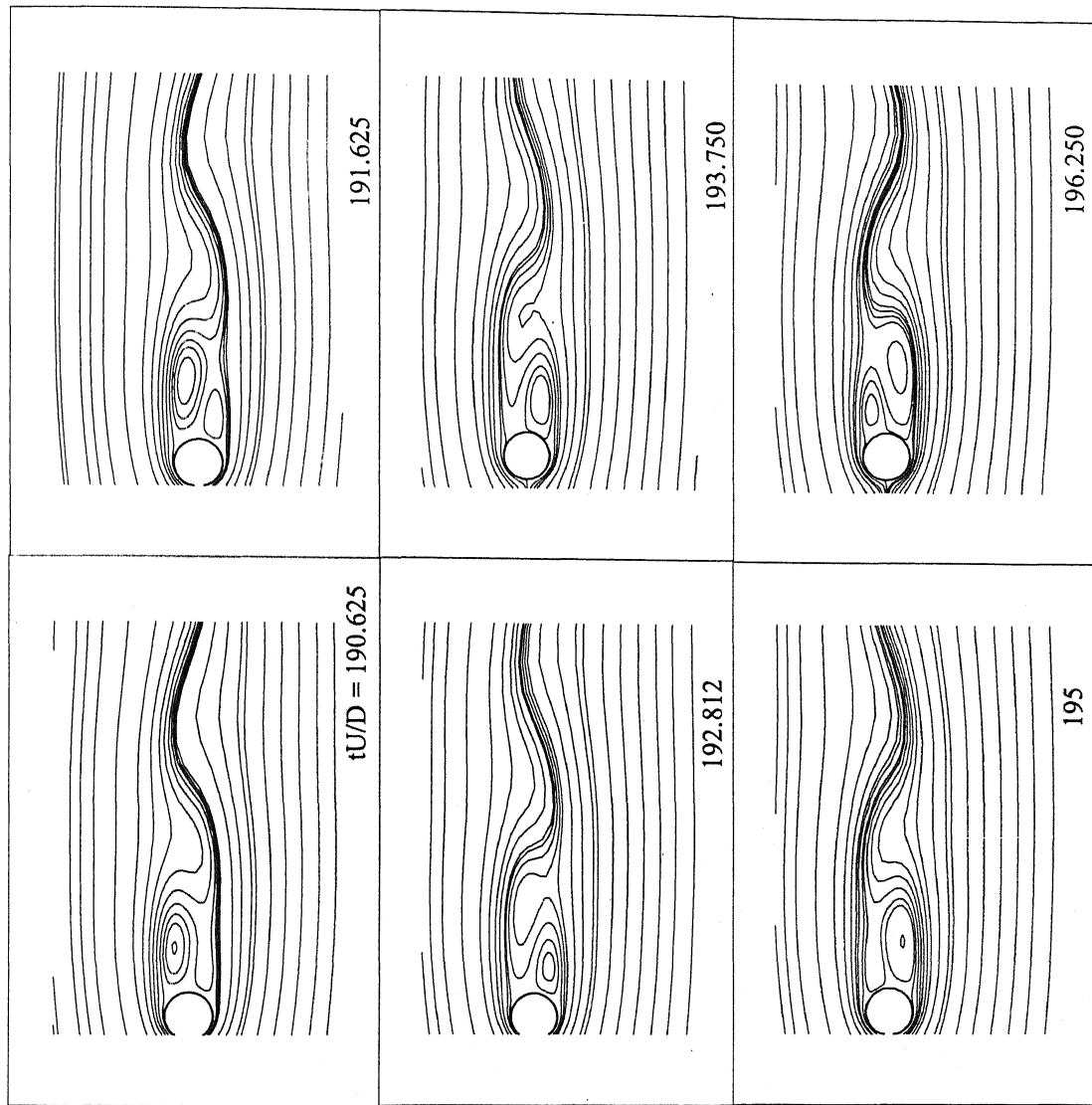
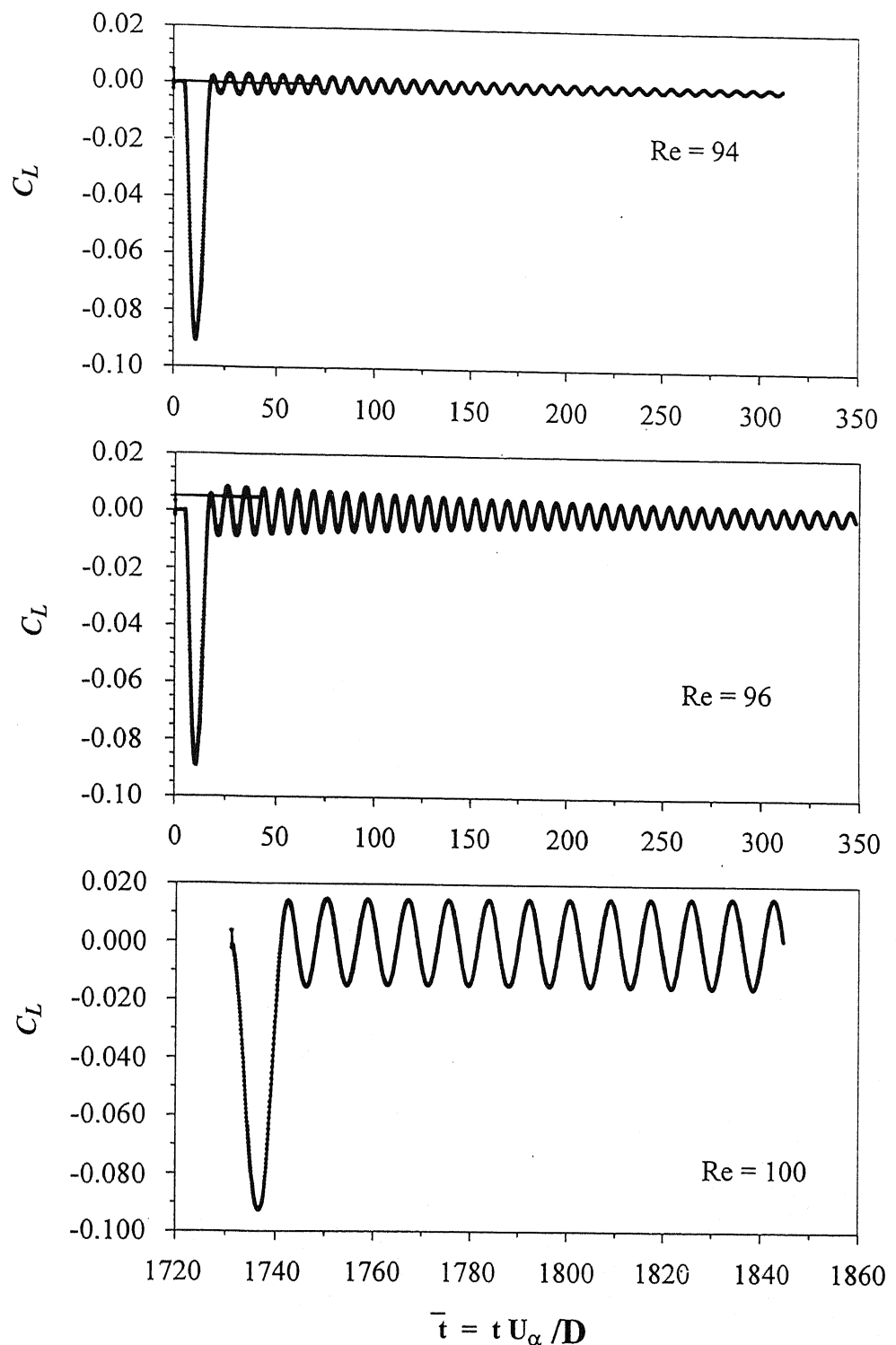


Figure 6.7: Streamline plots at  $Re = 50$  at different time steps from QUICK scheme



**Figure 6.8:  $C_L$  time histories at  $Re = 94, 96$  and  $100$  by first order upwinding scheme**

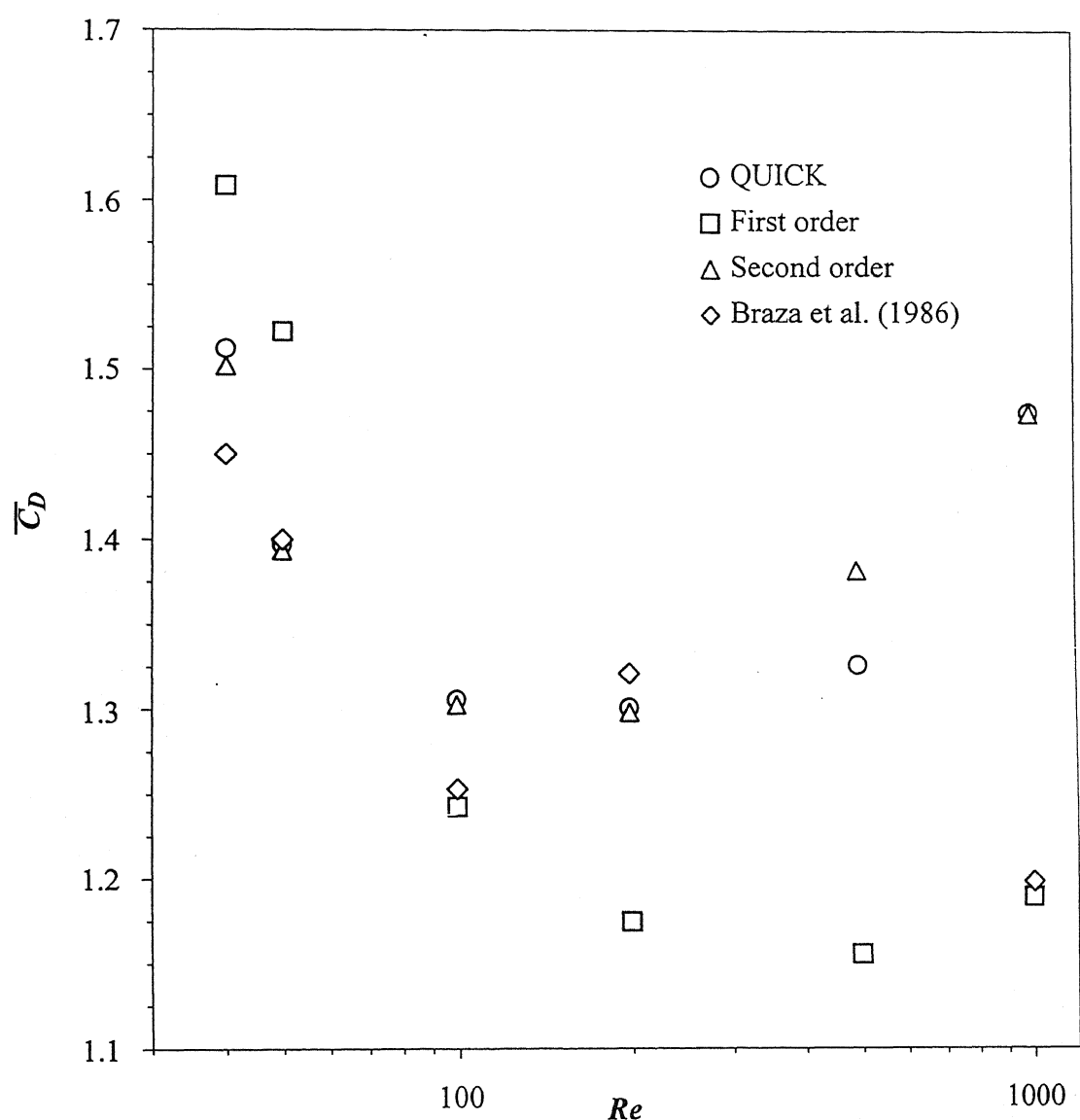


Figure 6.9:  $\bar{C}_D$  vs  $Re$  calculated from various upwinding schemes

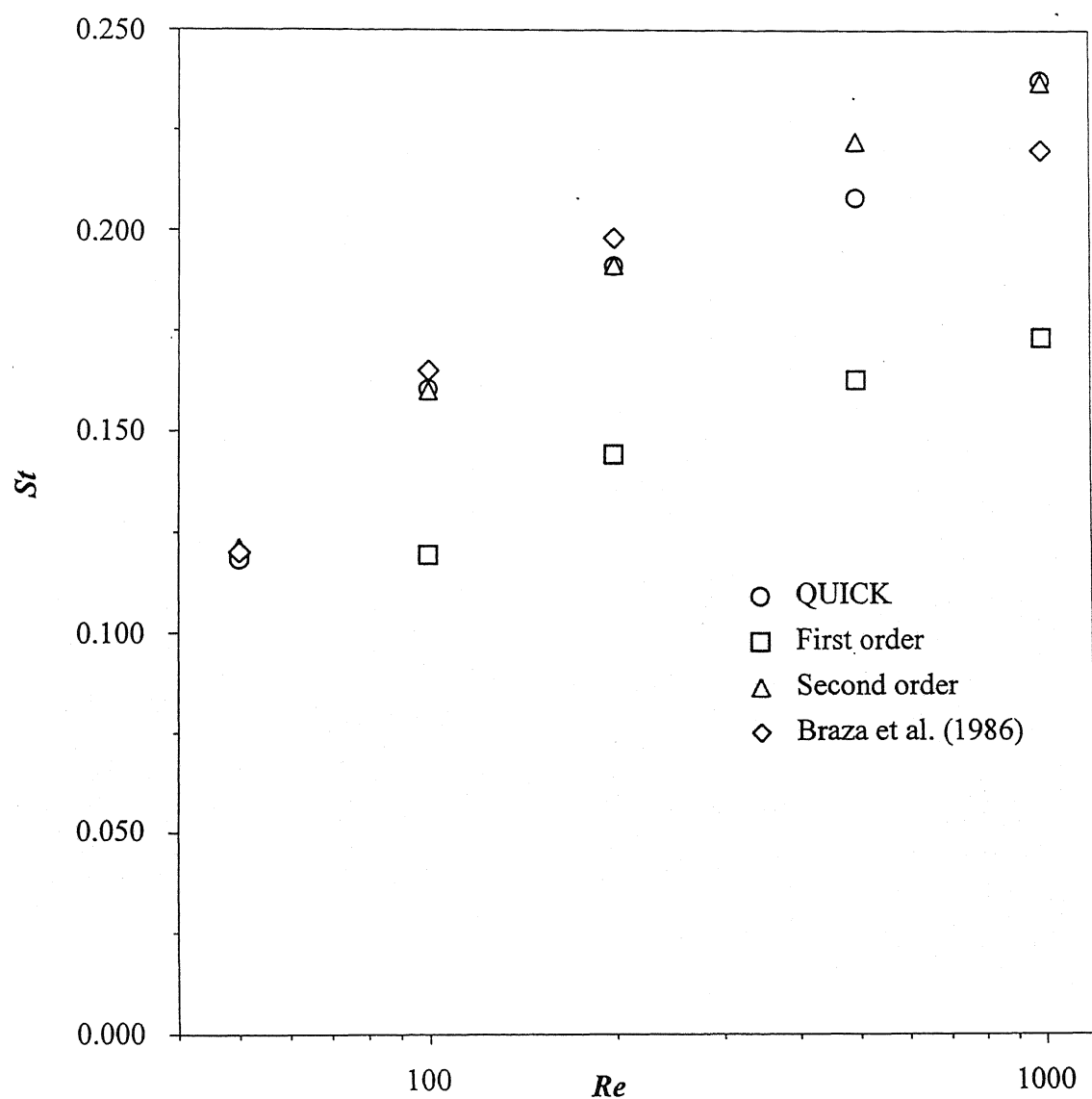


Figure 6.10:  $St$  vs  $Re$  calculated from various upwinding schemes

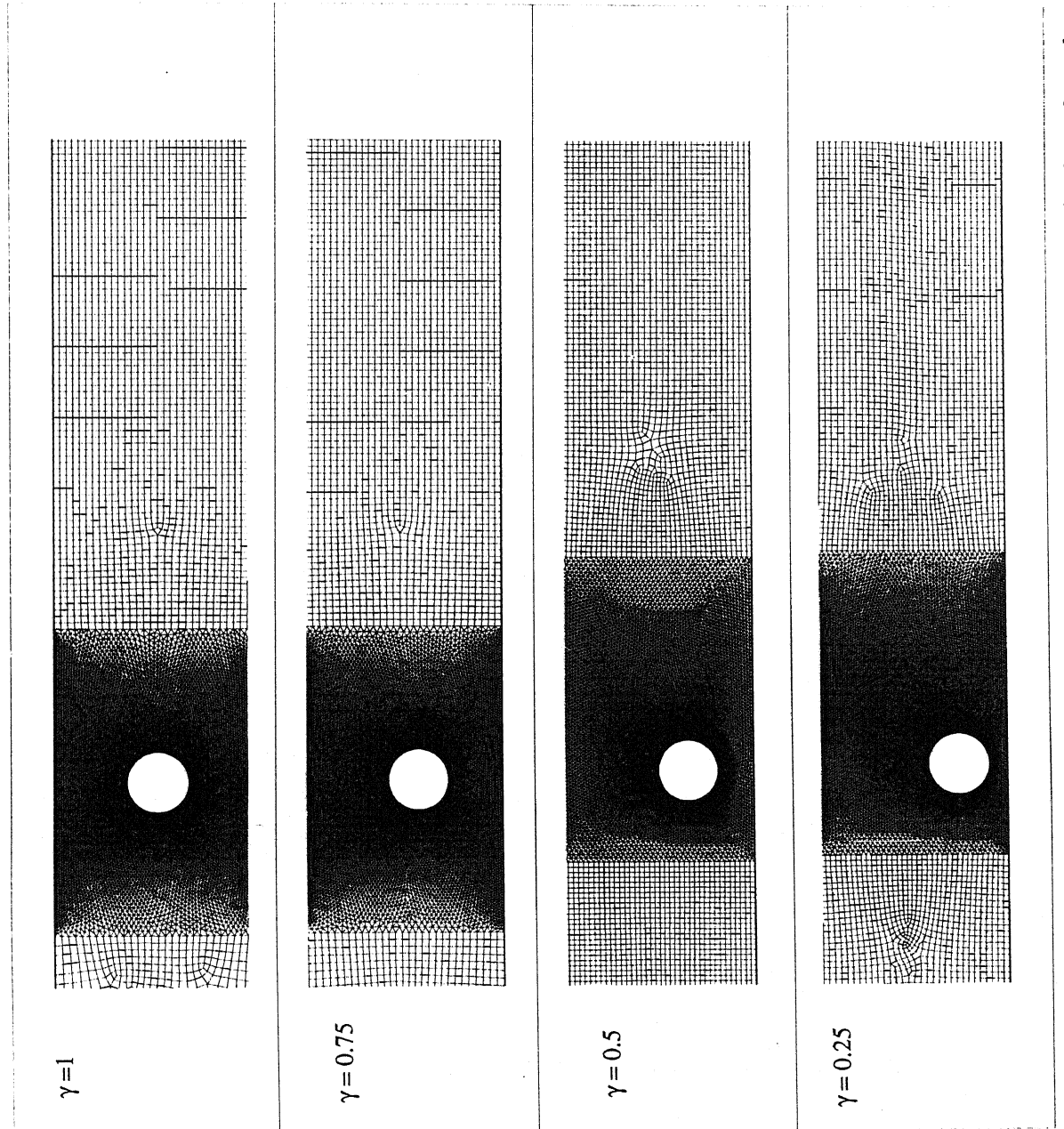


Figure 6.11: Typical mesh configurations used to simulate flow past a cylinder confined in plane channel

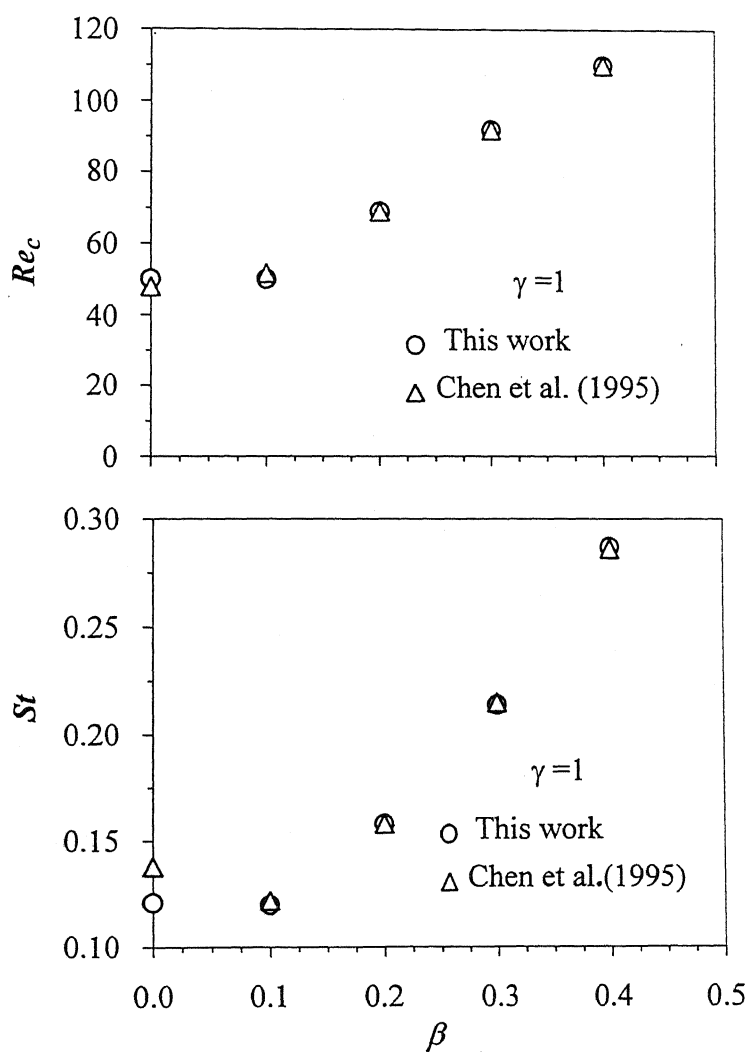
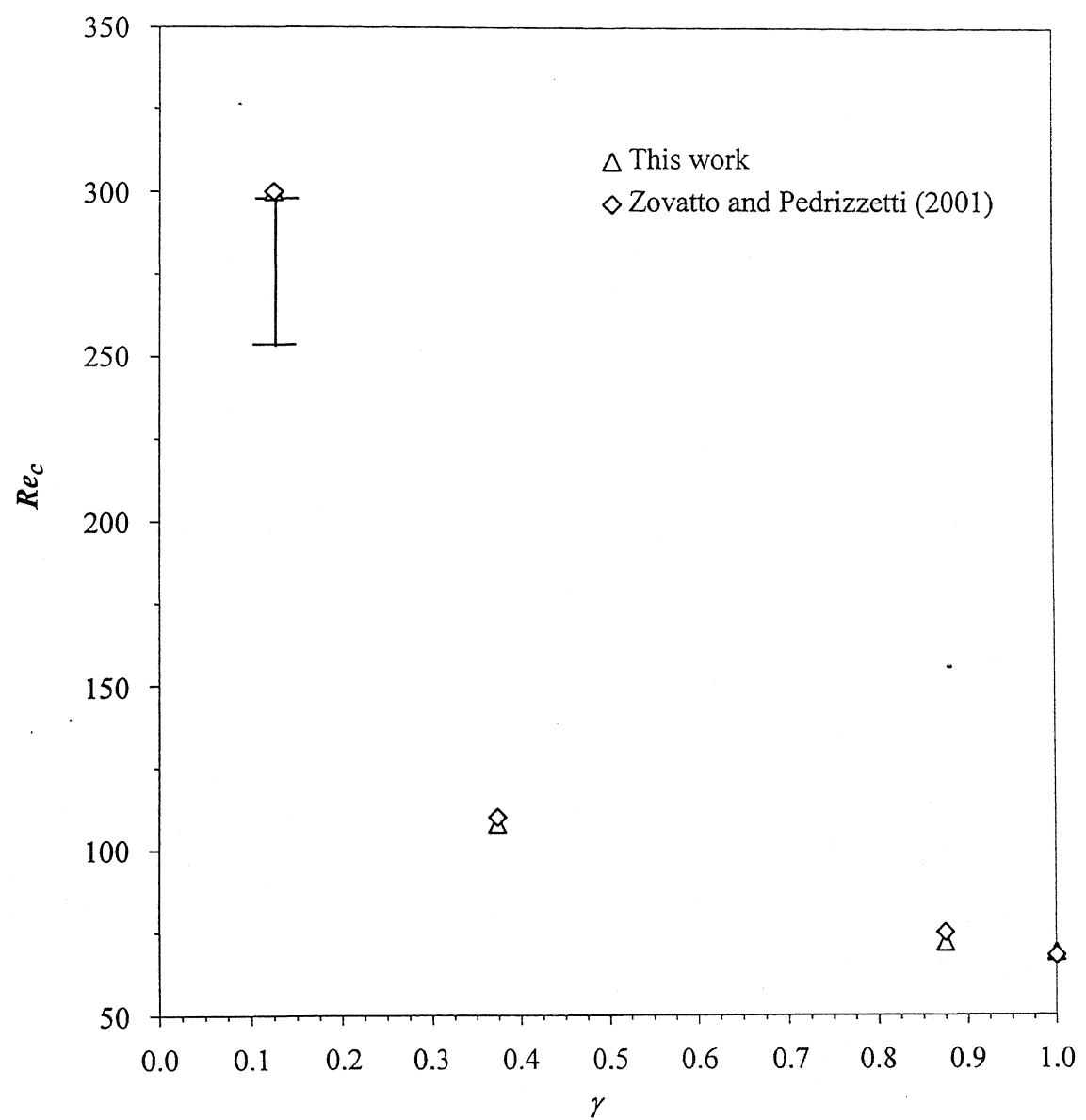


Figure 6.12: Comparison of  $Re_C$  and  $St$  for various  $\beta$  and  $\gamma = 1$  (symmetrical)



**Figure 6.13: Variation of critical Re with  $\gamma$  for  $\beta = 0.2$**

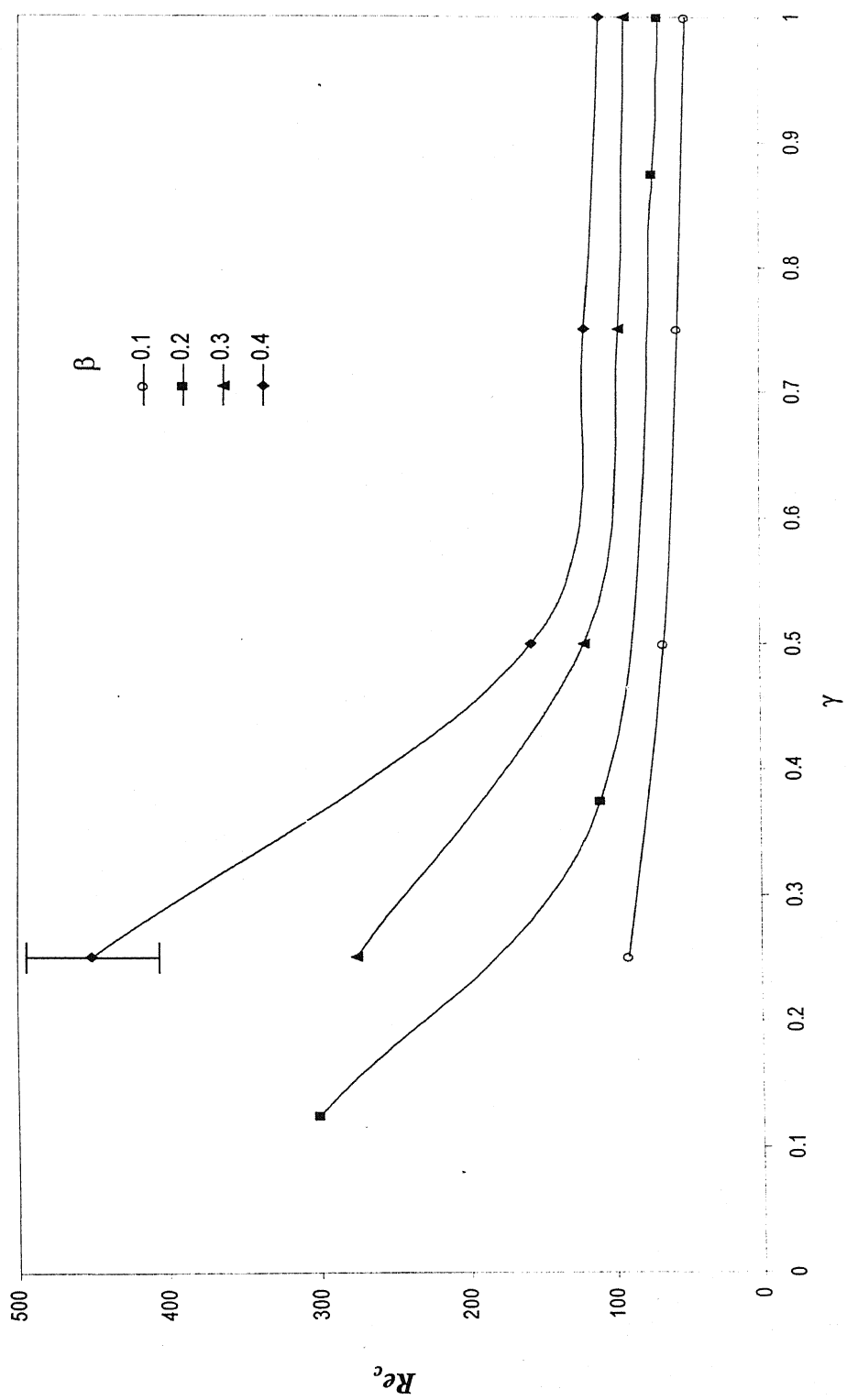


Figure 6.14: Variation of critical  $Re$  with  $\beta$  and  $\gamma$

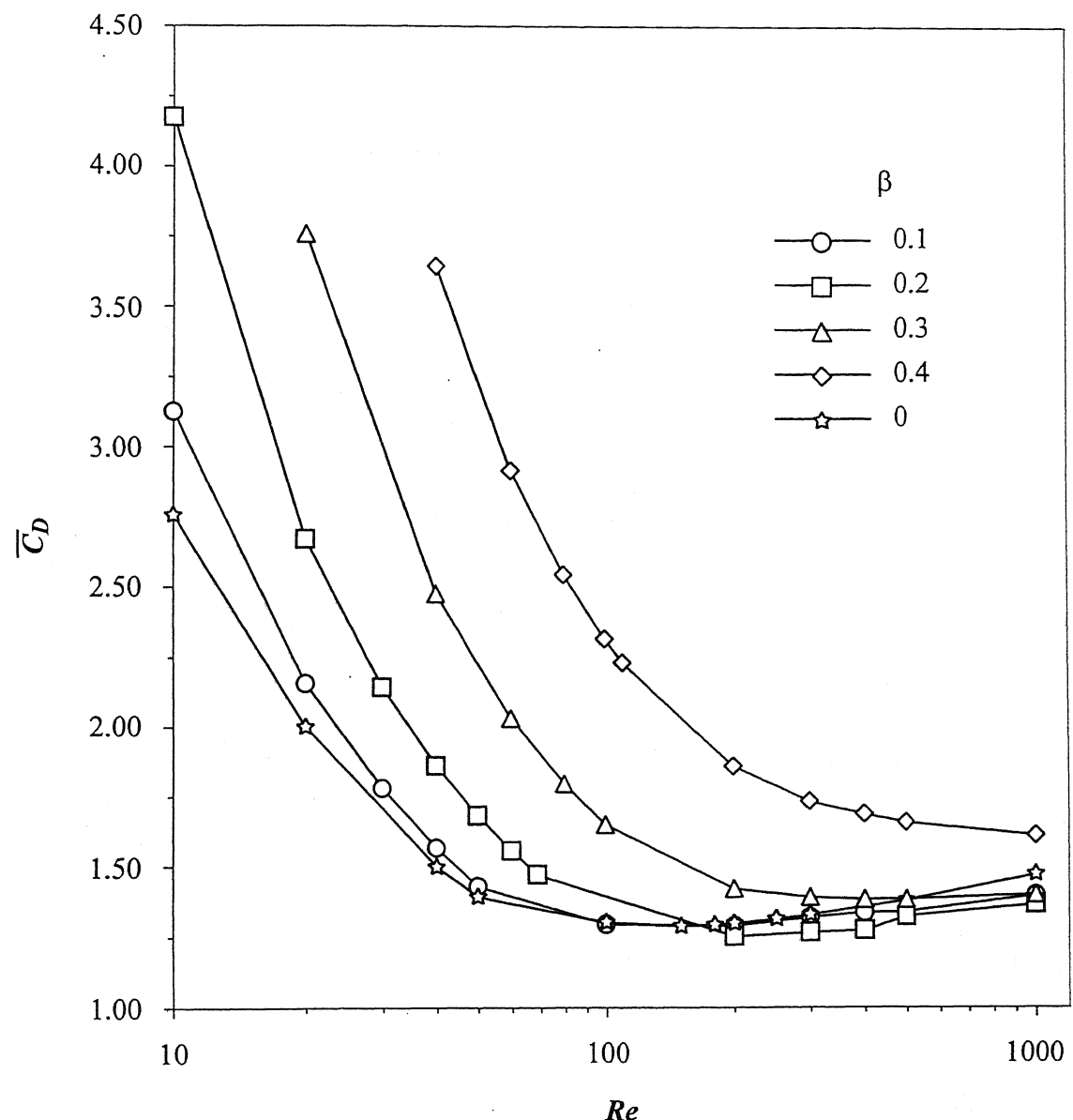


Figure 6.15: Effect of blockage ratio ( $\beta$ ) on  $\bar{C}_D$  for  $\gamma = 1$  (symmetrical)

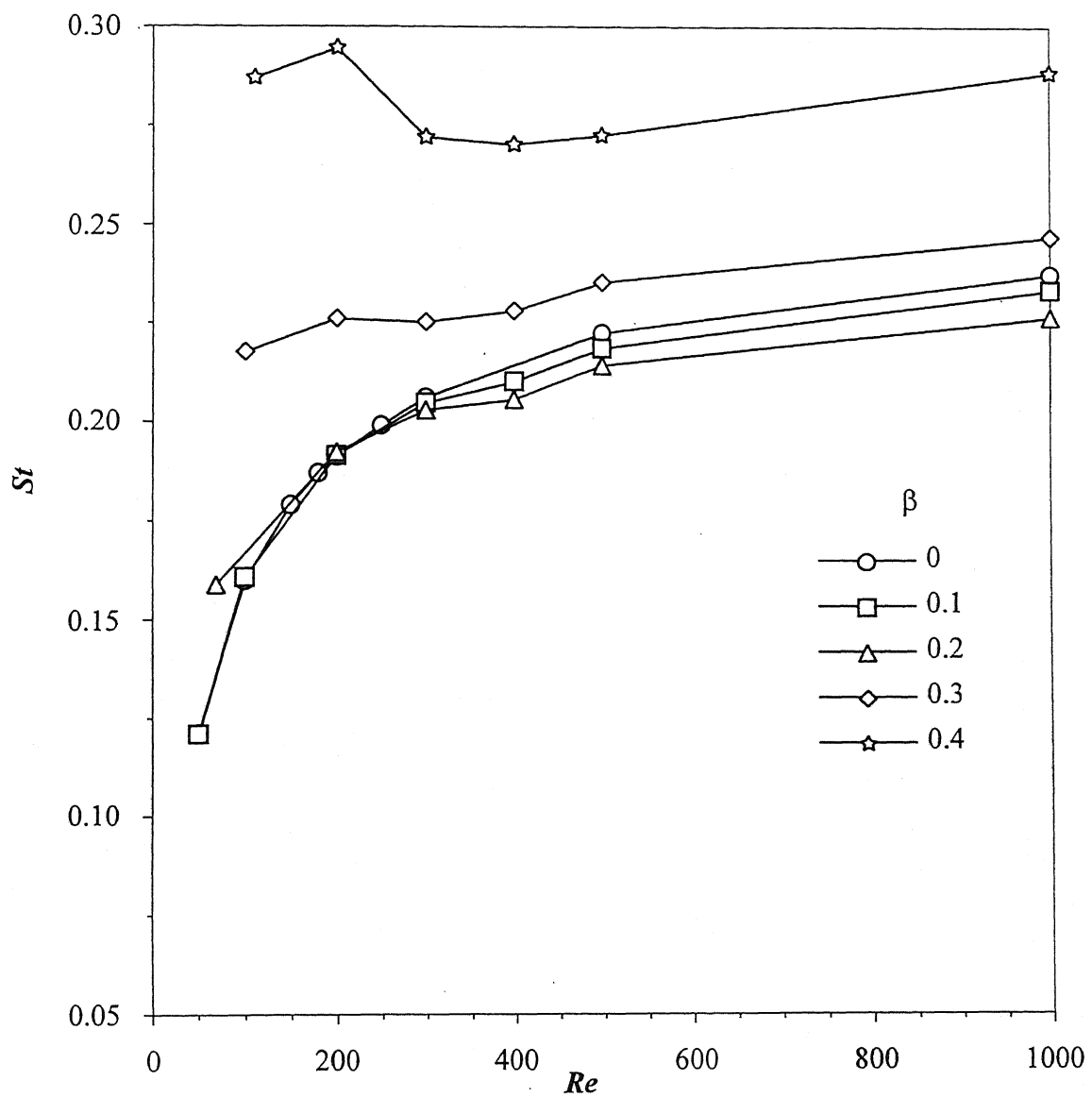


Figure 6.16: Effect of blockage ratio ( $\beta$ ) on  $St$  for  $\gamma = 1$  (symmetrical)

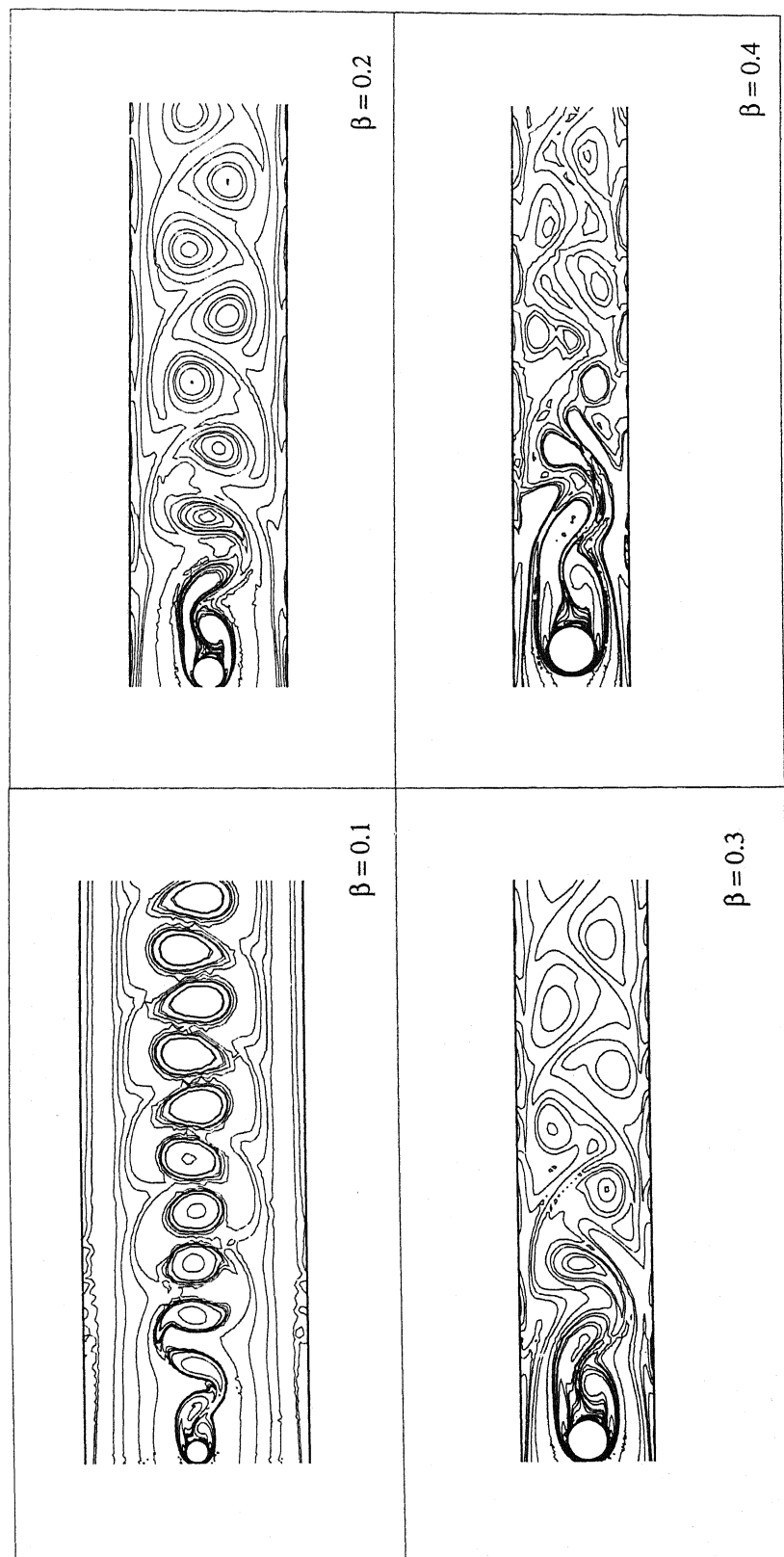
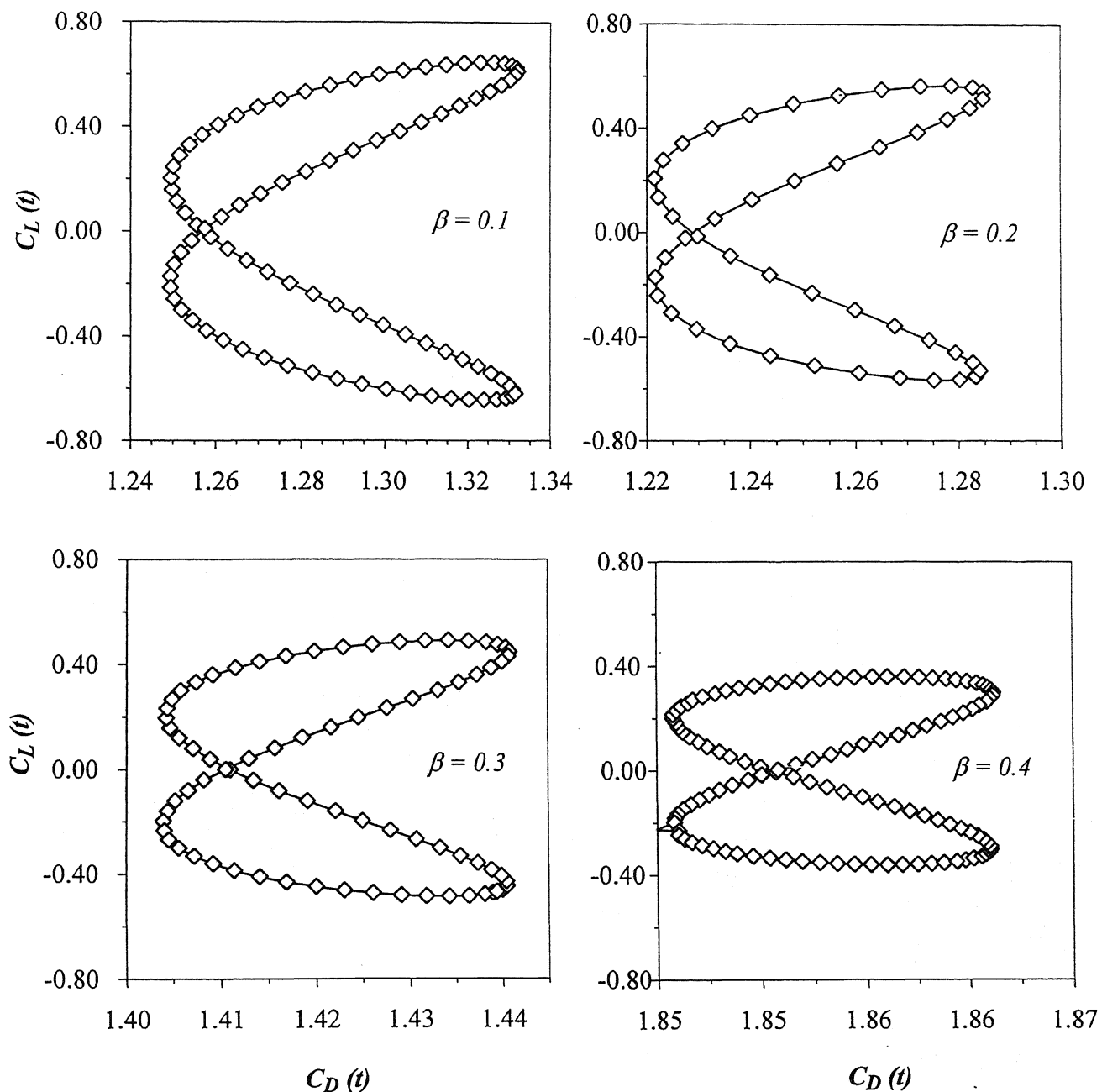
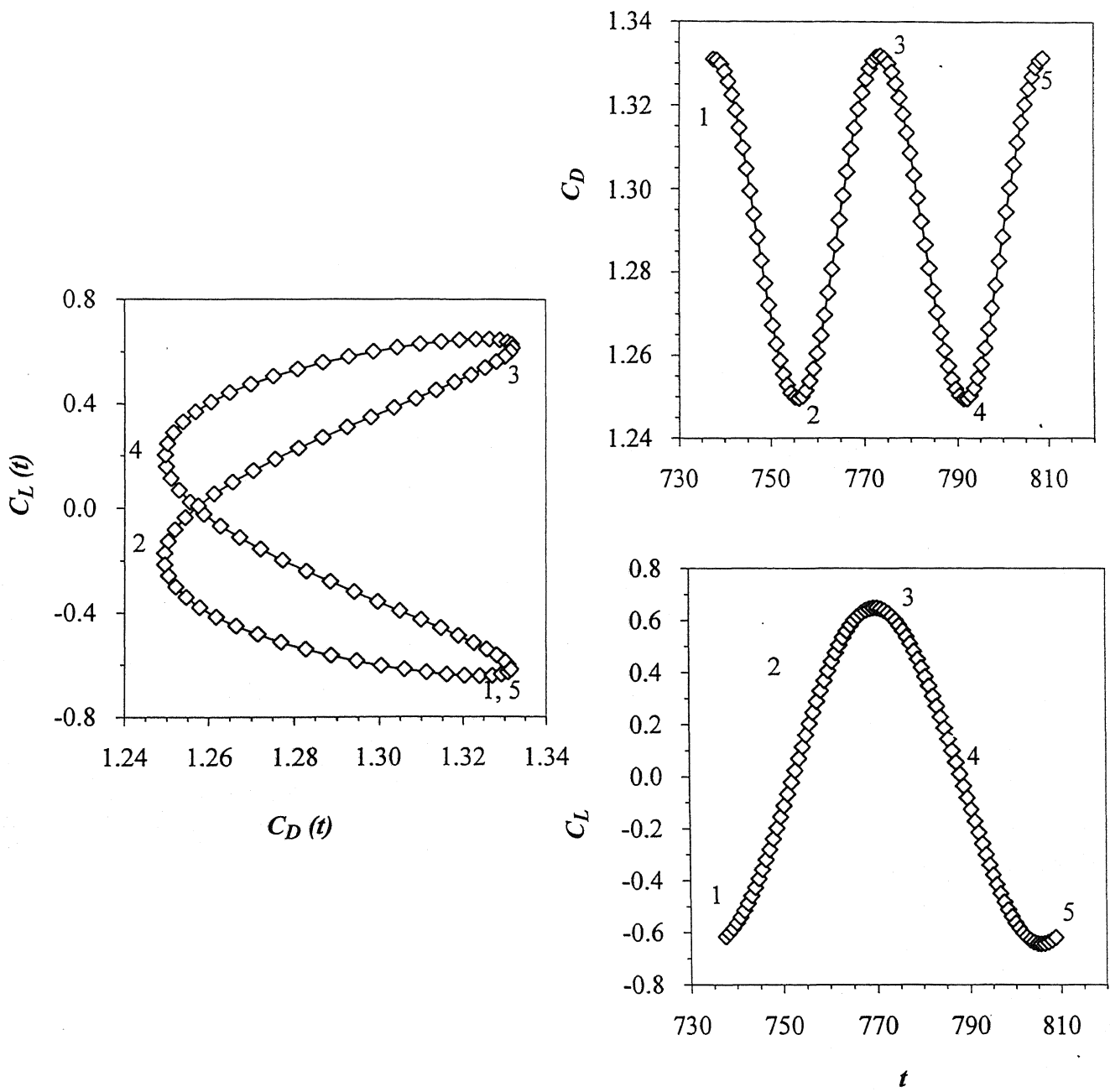


Figure 6.17: Snapshots of instantaneous vorticity contours at  $Re = 200$  for various blockage ratios



**Figure 6.18:  $C_L$ - $C_D$  periodic trajectories during one period at  $Re = 200$  for various  $\beta$  and  $\gamma = 1$**



**Figure 6.19: Trajectory of  $C_D$  and  $C_L$  and time histories of  $C_D$  and  $C_L$  for  $\beta = 0.1$  and  $\gamma = 1$**

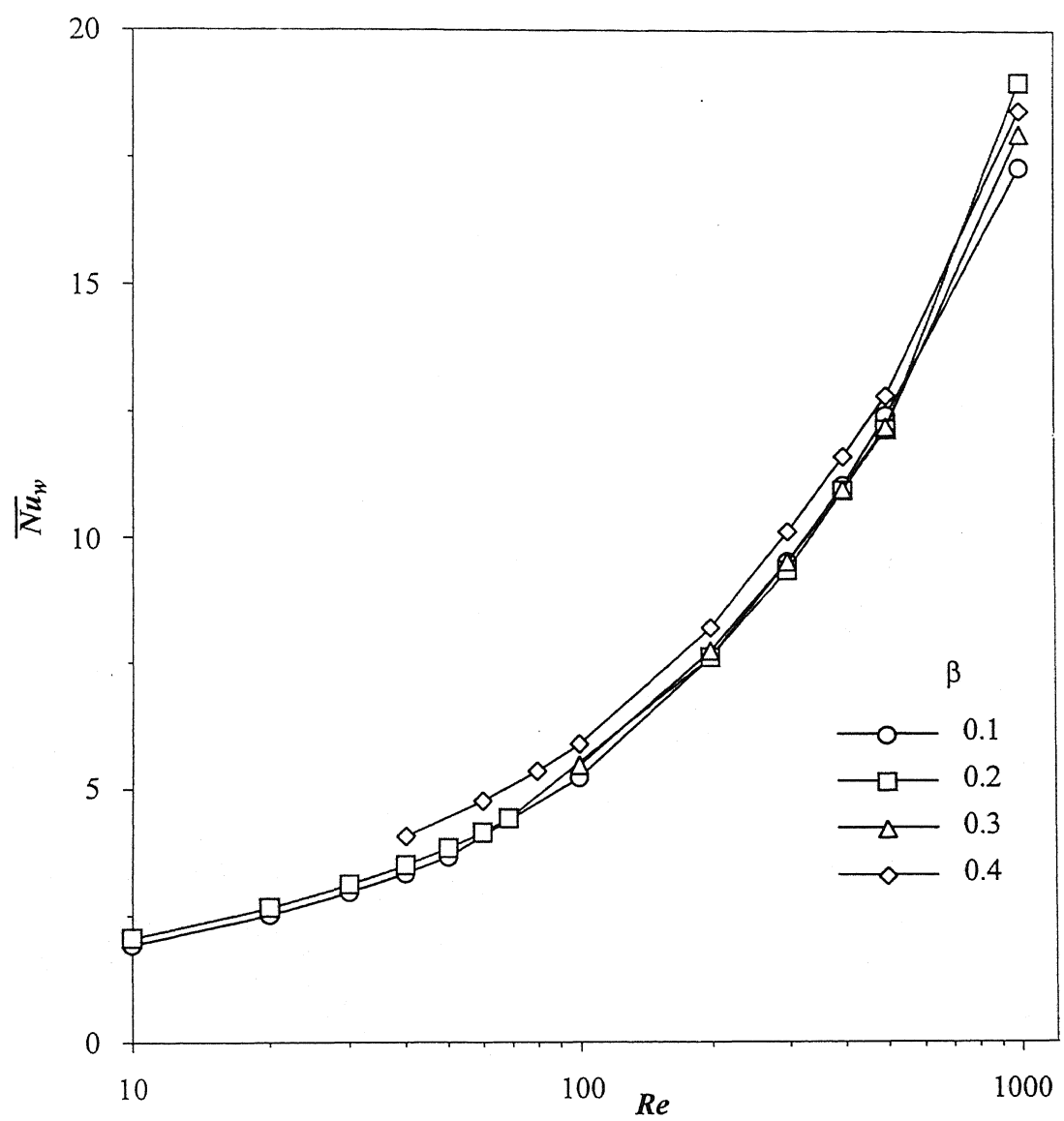


Figure 6.20 : Effect of blockage ratio (  $\beta$  ) on  $\overline{Nu}_w$  (Pr =0.7441) for  $\gamma = 1$  (symmetrical)

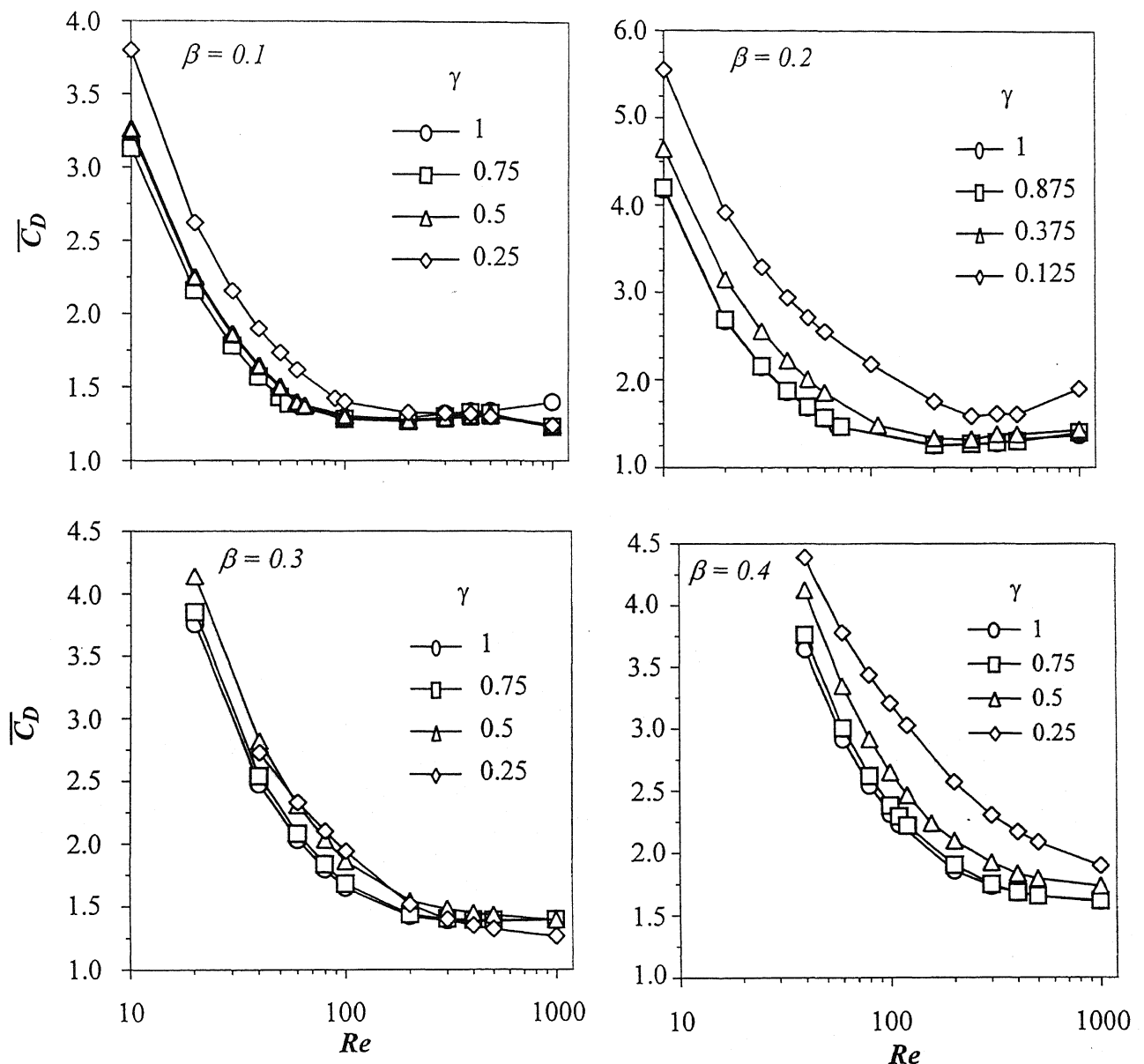


Figure 6.21:  $\bar{C}_D$  vs  $Re$  as a function of  $\beta$  and  $\gamma$

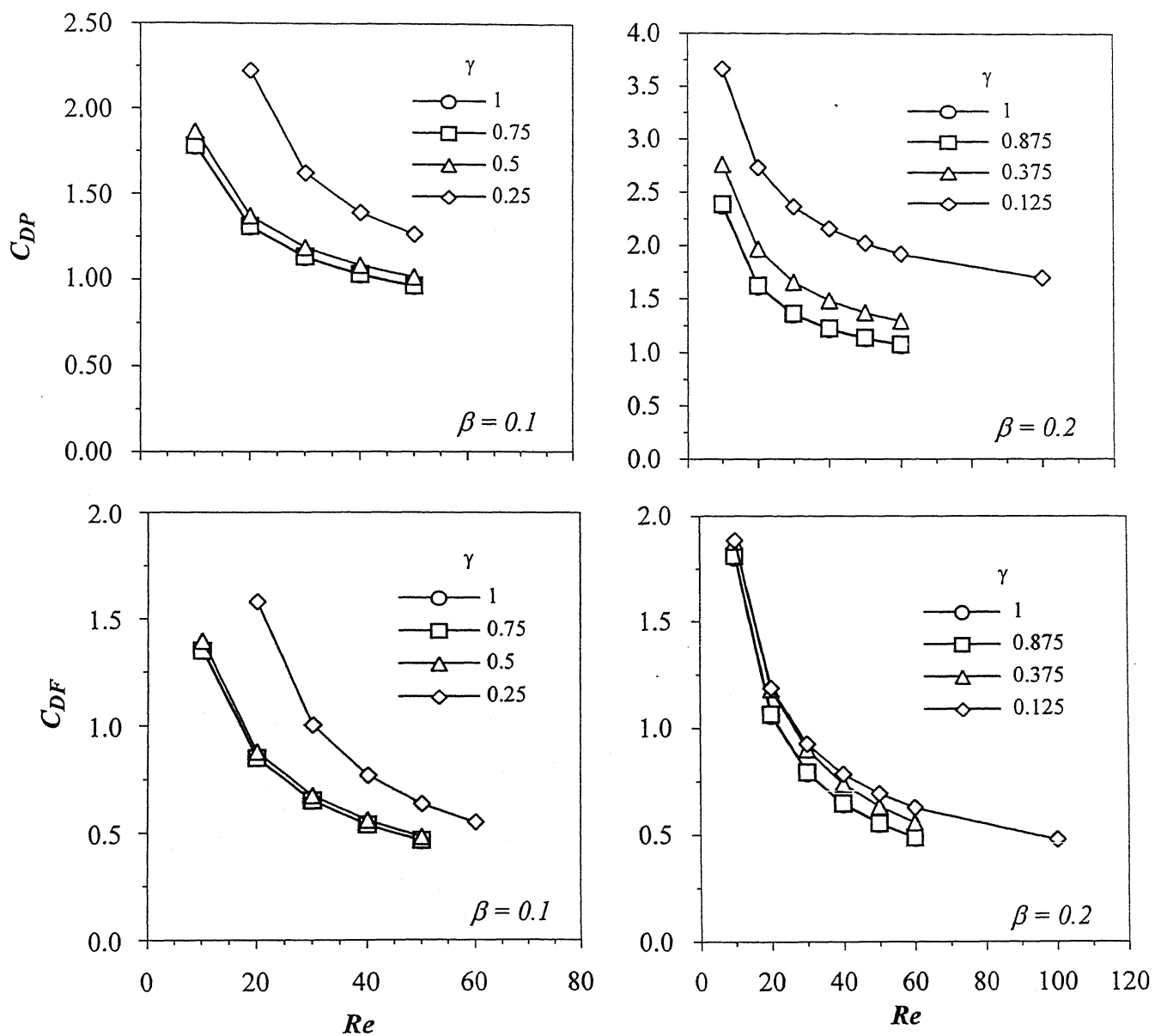


Figure 6.22:  $C_{DP}$  vs  $Re$  and  $C_{DF}$  vs  $Re$  as a function of  $\gamma$  ( $\beta = 0.1$  and  $0.2$ )

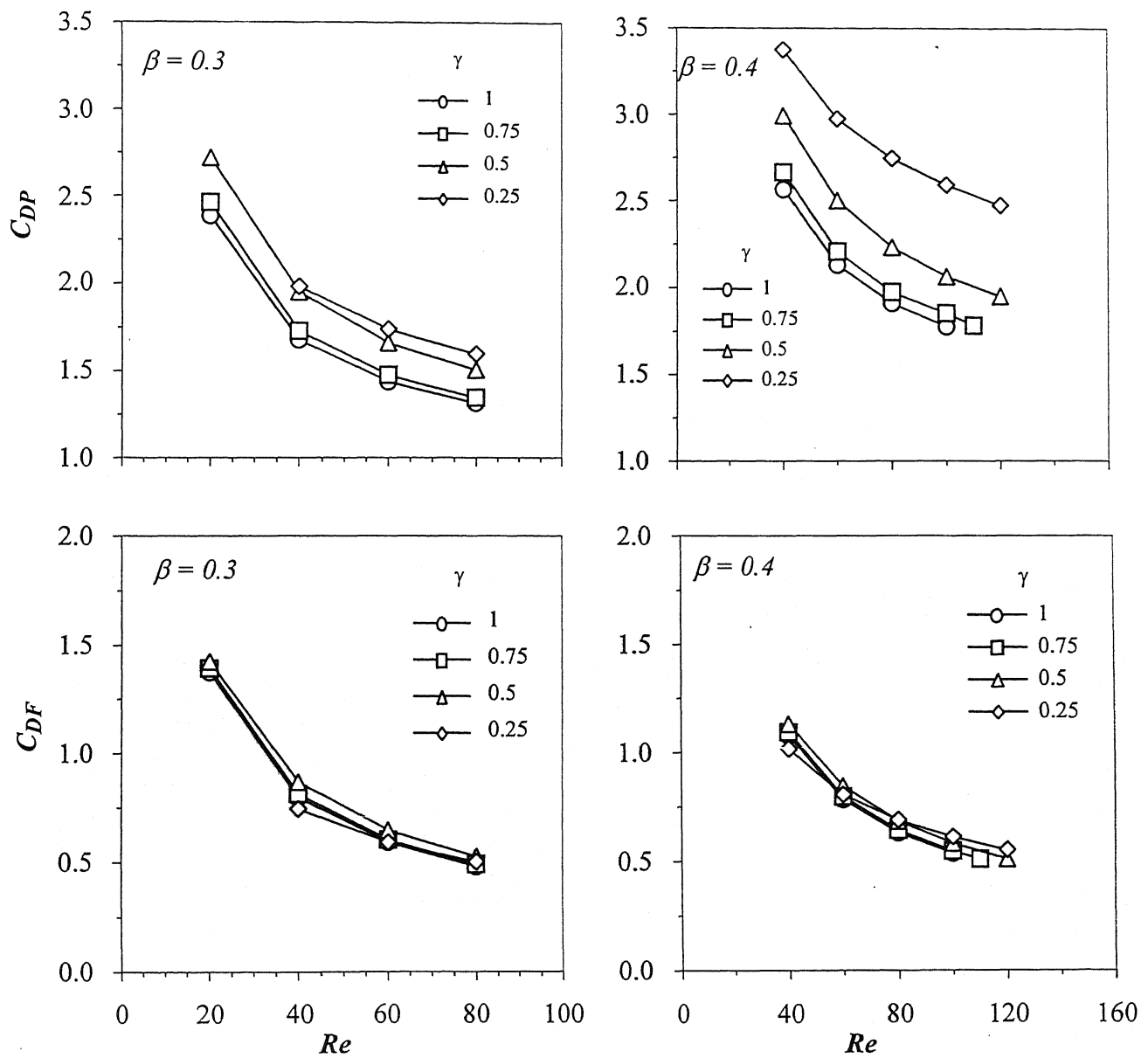
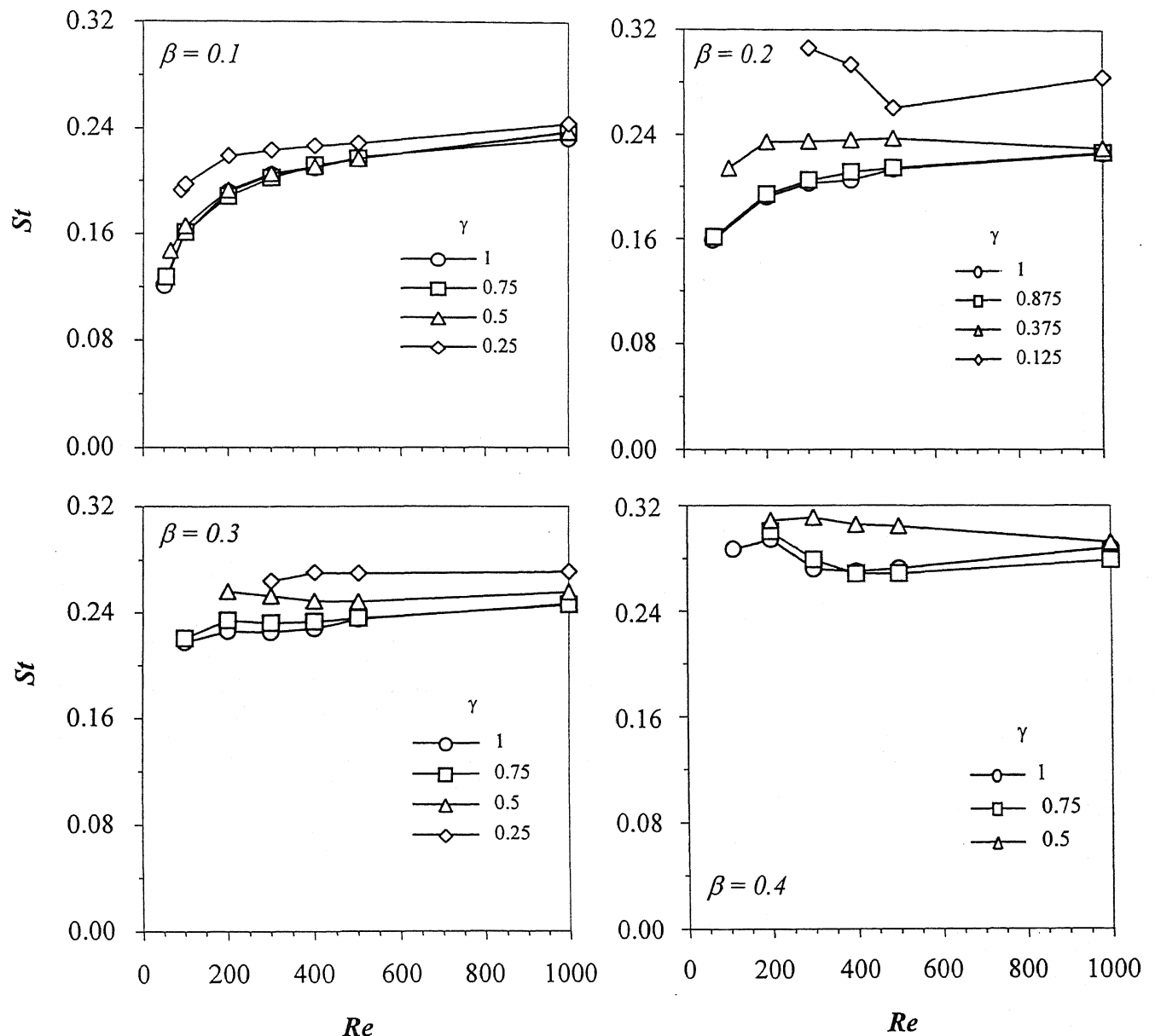


Figure 6.23:  $C_{DP}$  vs  $Re$  and  $C_{DF}$  vs  $Re$  as a function of  $\gamma$  ( $\beta = 0.3$  and  $0.4$ )



**Figure 6.24:  $St$  vs  $Re$  as a function of  $\beta$  and  $\gamma$**

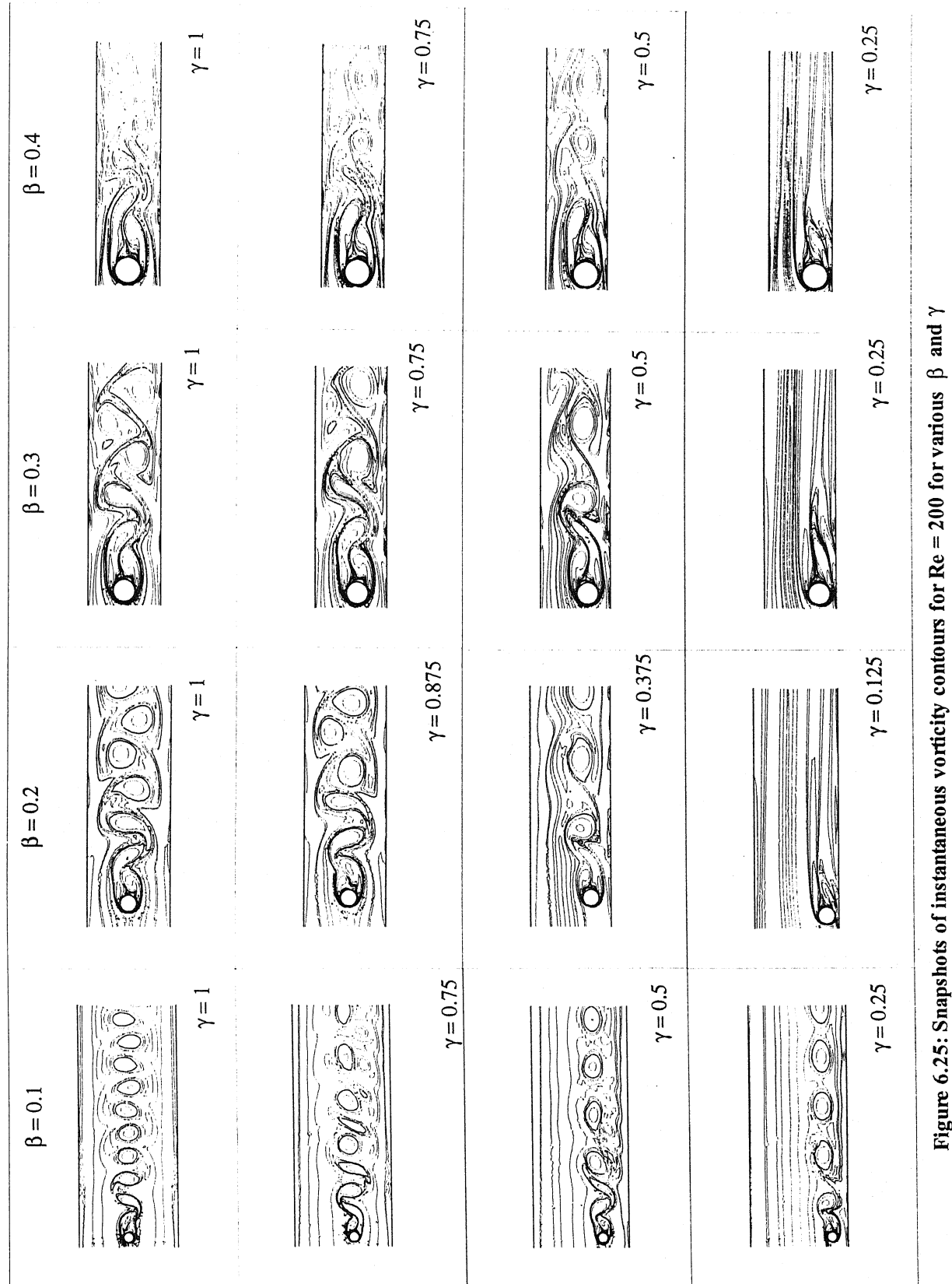


Figure 6.25: Snapshots of instantaneous vorticity contours for  $Re = 200$  for various  $\beta$  and  $\gamma$

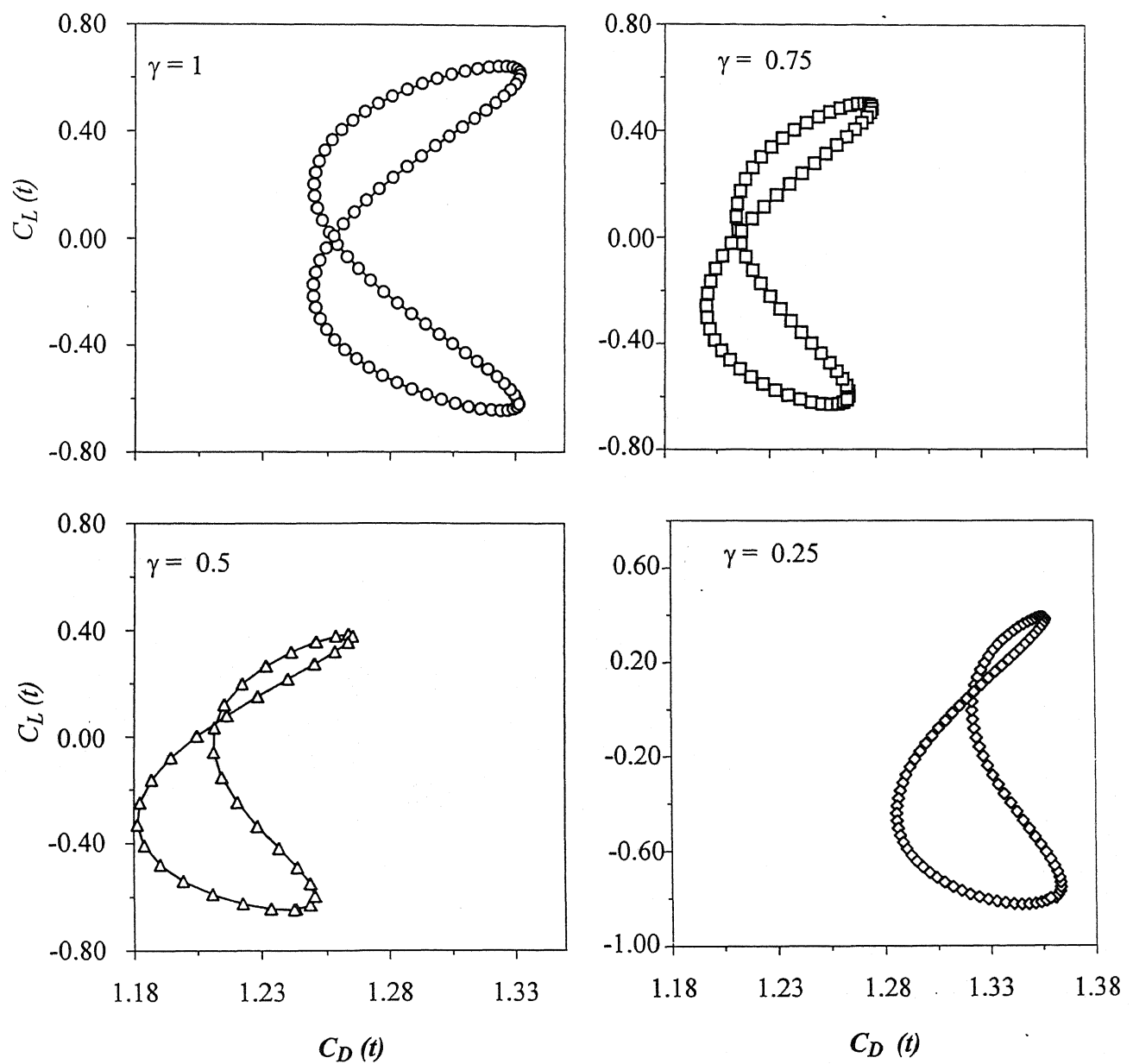


Figure 6.26:  $C_L$ - $C_D$  periodic trajectories at  $Re = 200$  for  $\beta = 0.1$  as a function of  $\gamma$

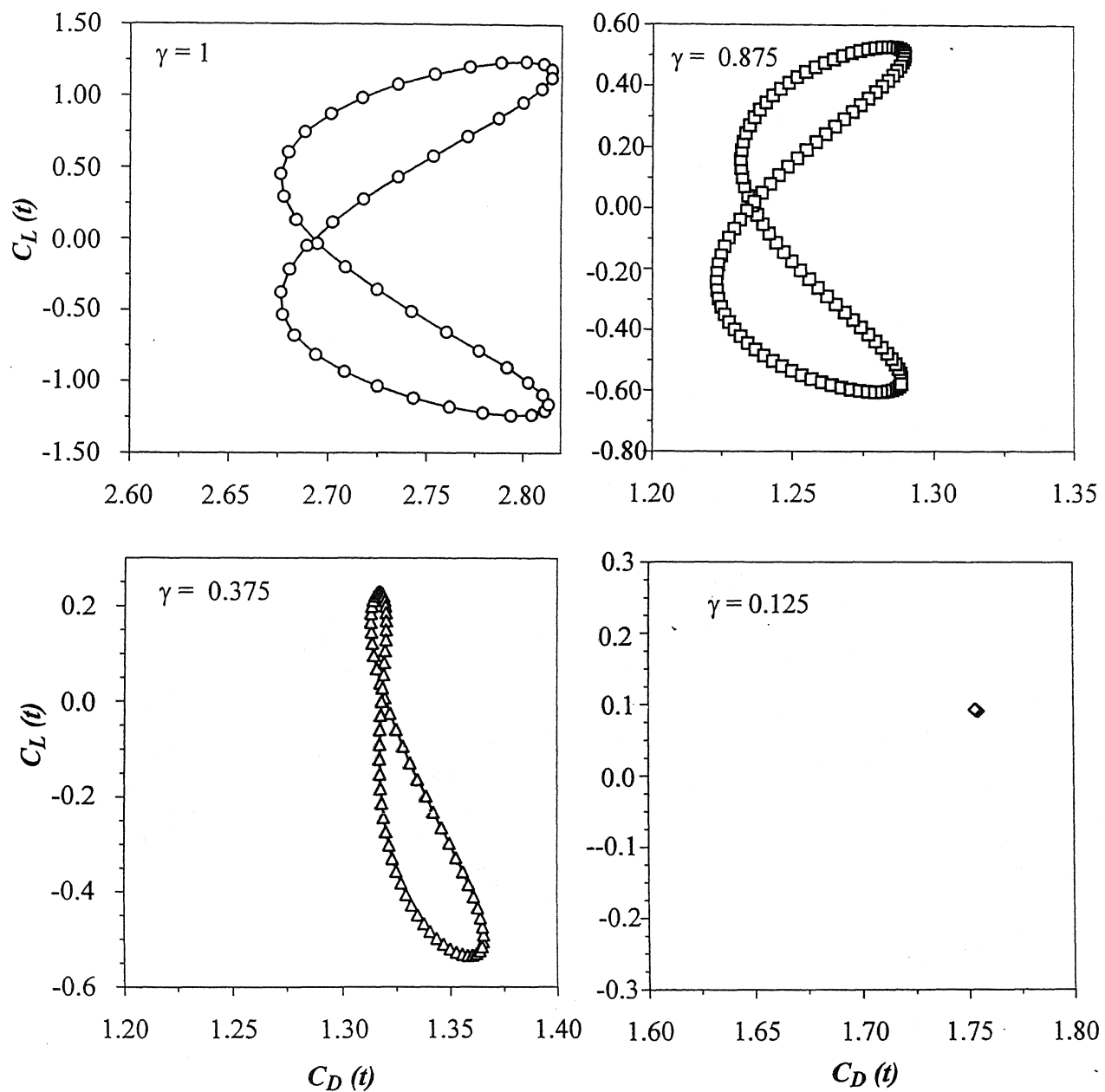


Figure 6.27:  $C_L$ - $C_D$  periodic trajectories at  $Re = 200$  and  $\beta = 0.2$  as a function of  $\gamma$

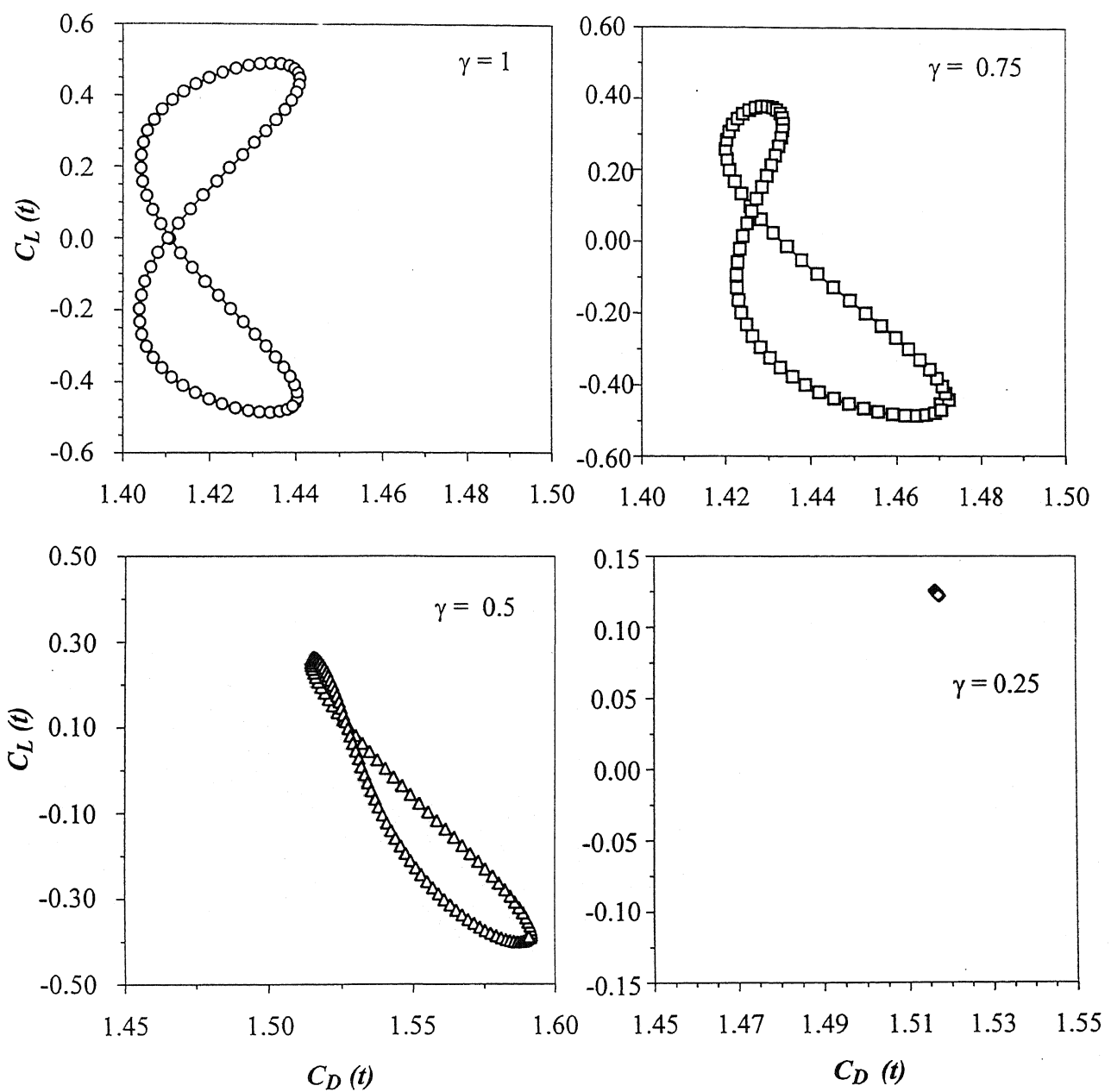


Figure 6.28:  $C_L$ - $C_D$  periodic trajectories at  $Re = 200$  and  $\beta = 0.3$  as a function of  $\gamma$

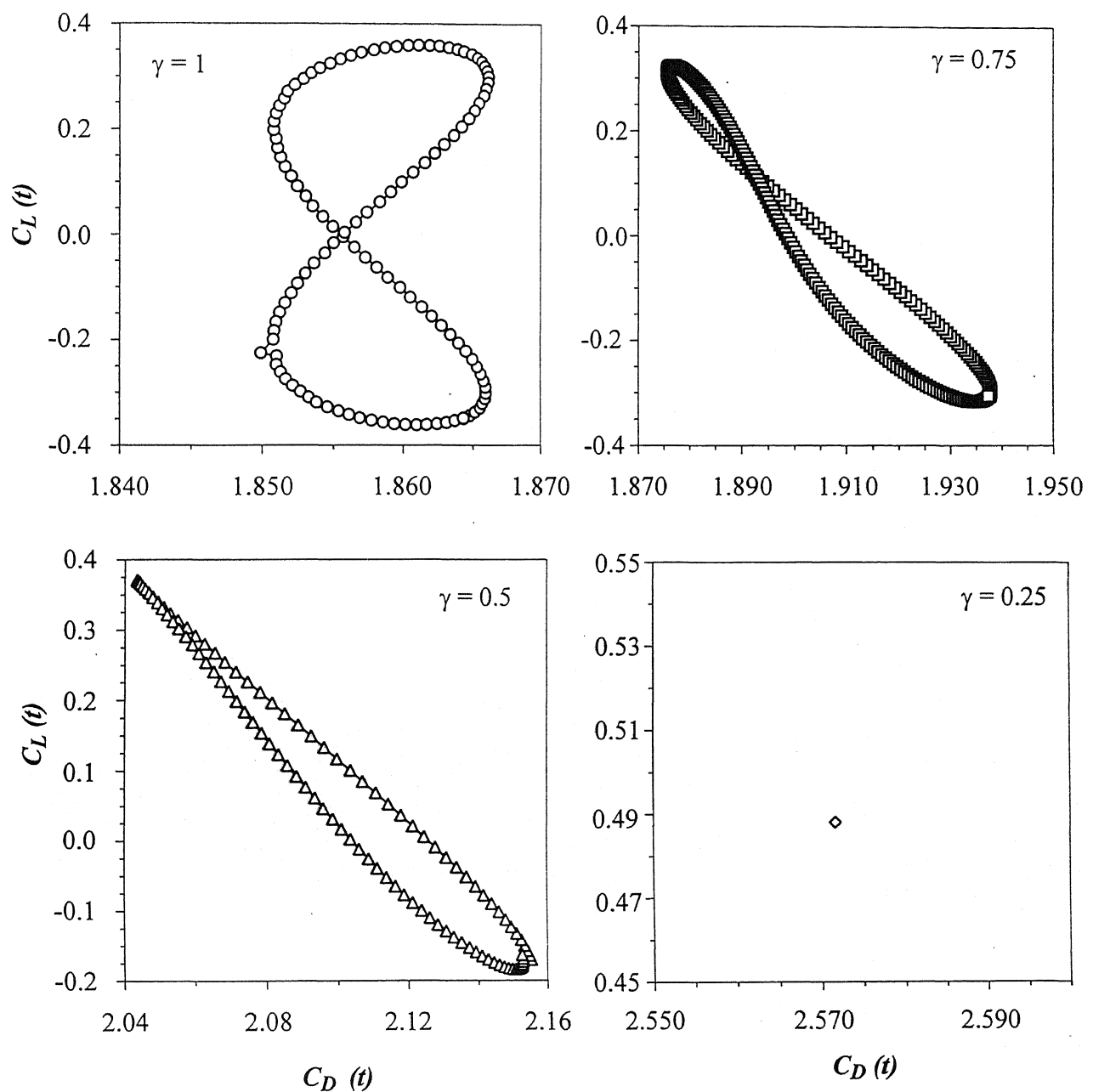


Figure 6.29:  $C_L$ - $C_D$  periodic trajectories at  $Re = 200$  and  $\beta = 0.4$  as a function of  $\gamma$

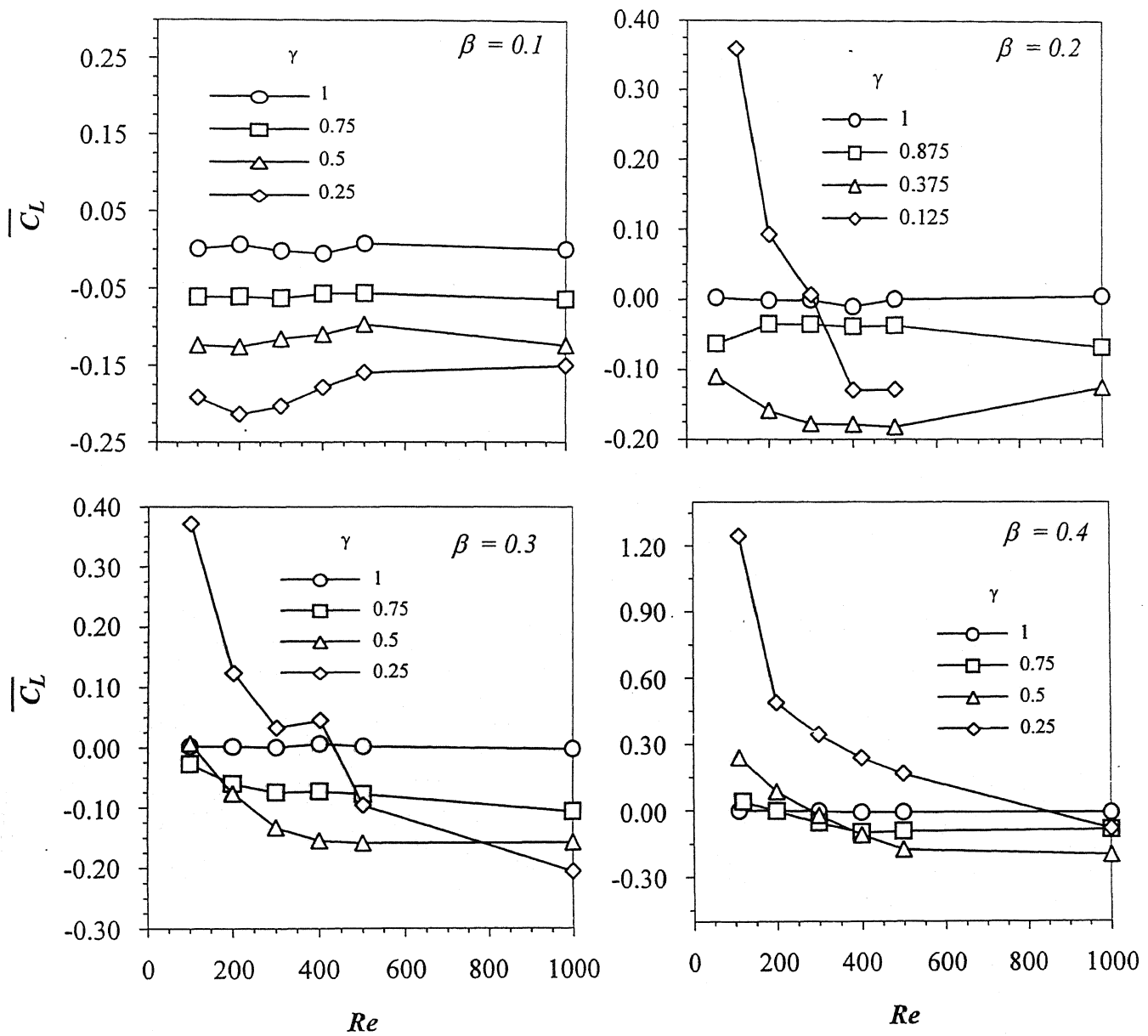


Figure 6.30:  $\bar{C}_L$  vs  $Re$  as a function of  $\beta$  and  $\gamma$

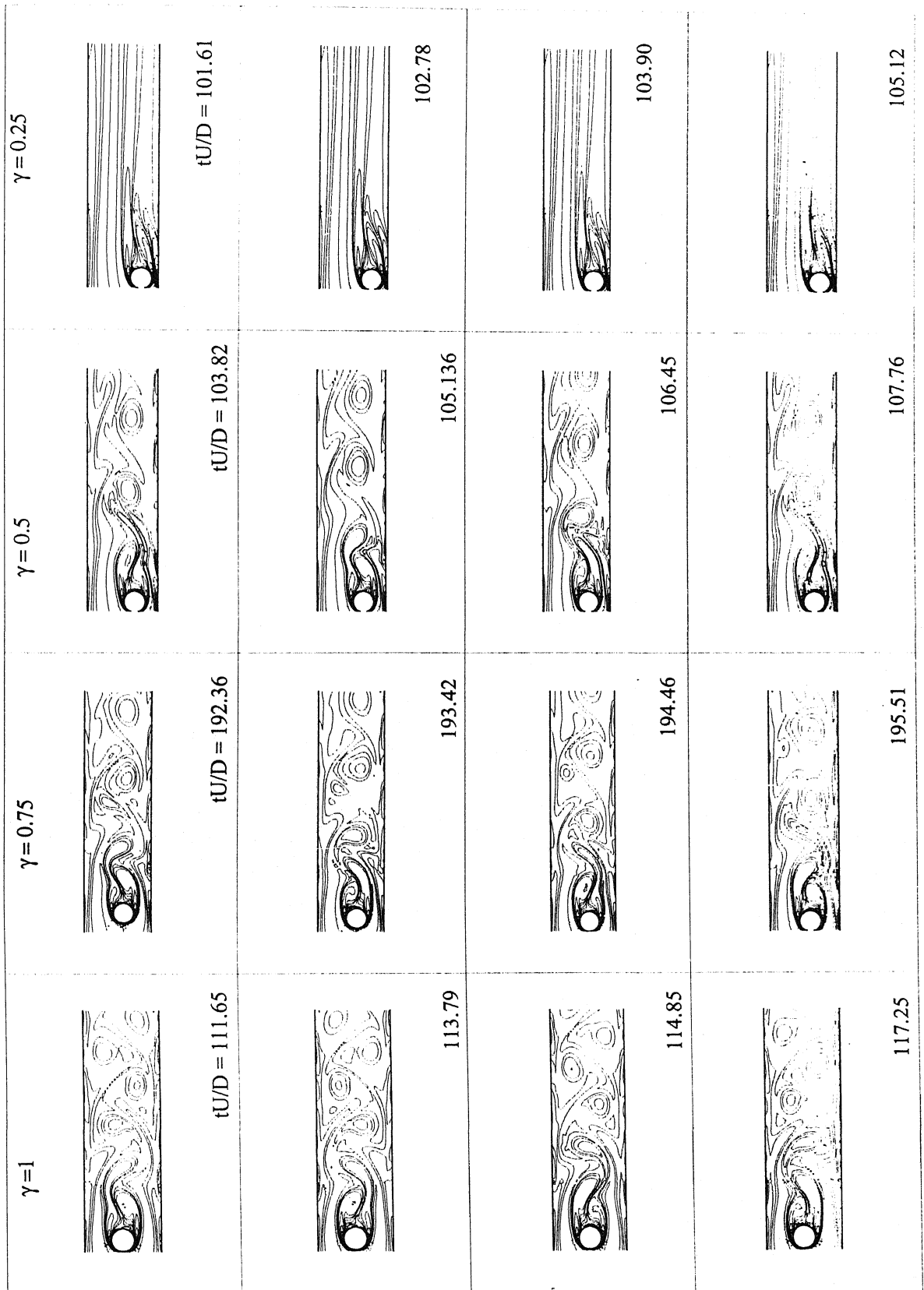


Figure 6.31: Unsteady vorticity contours at  $Re = 200$  and  $\beta = 0.3$

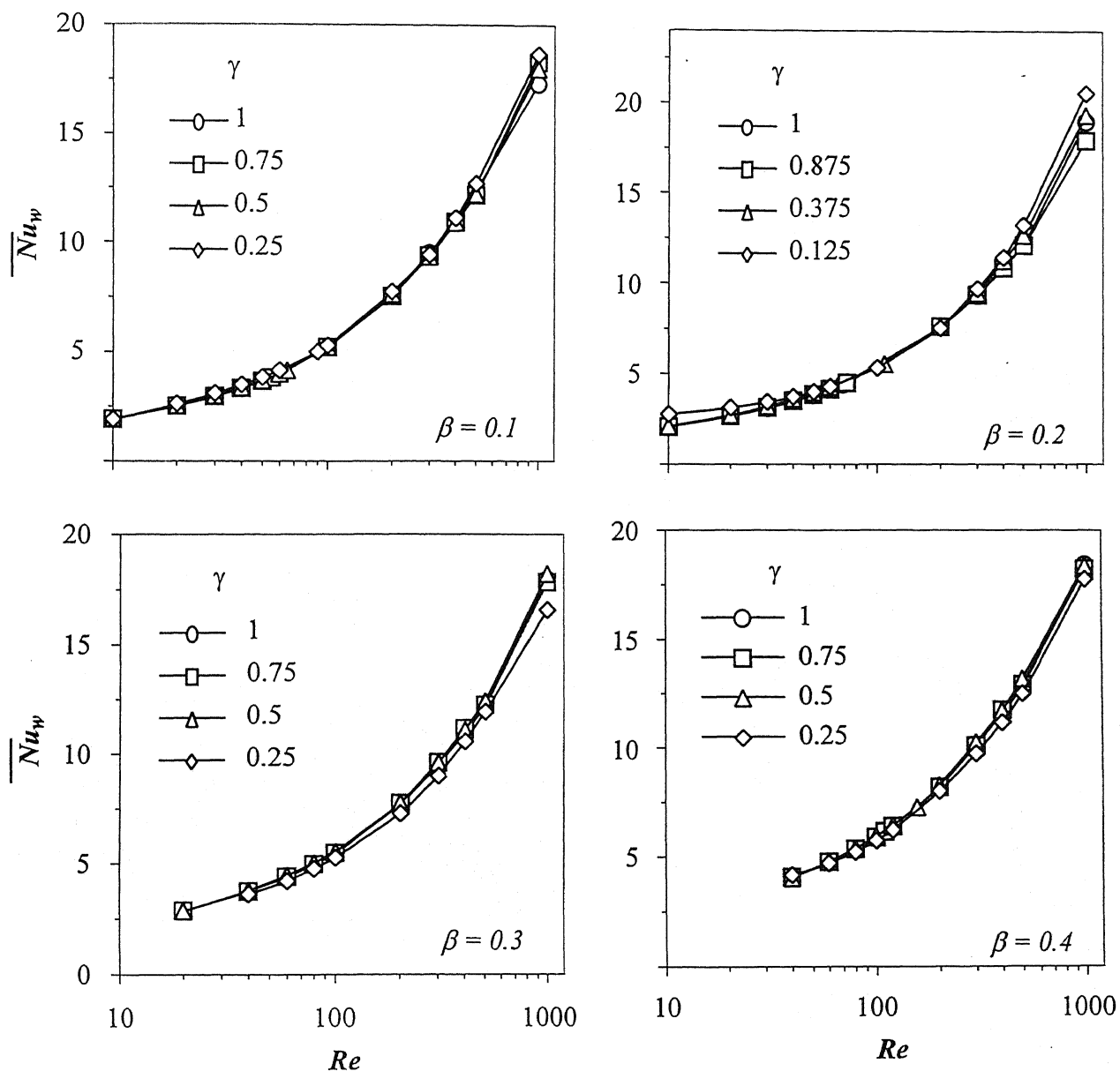
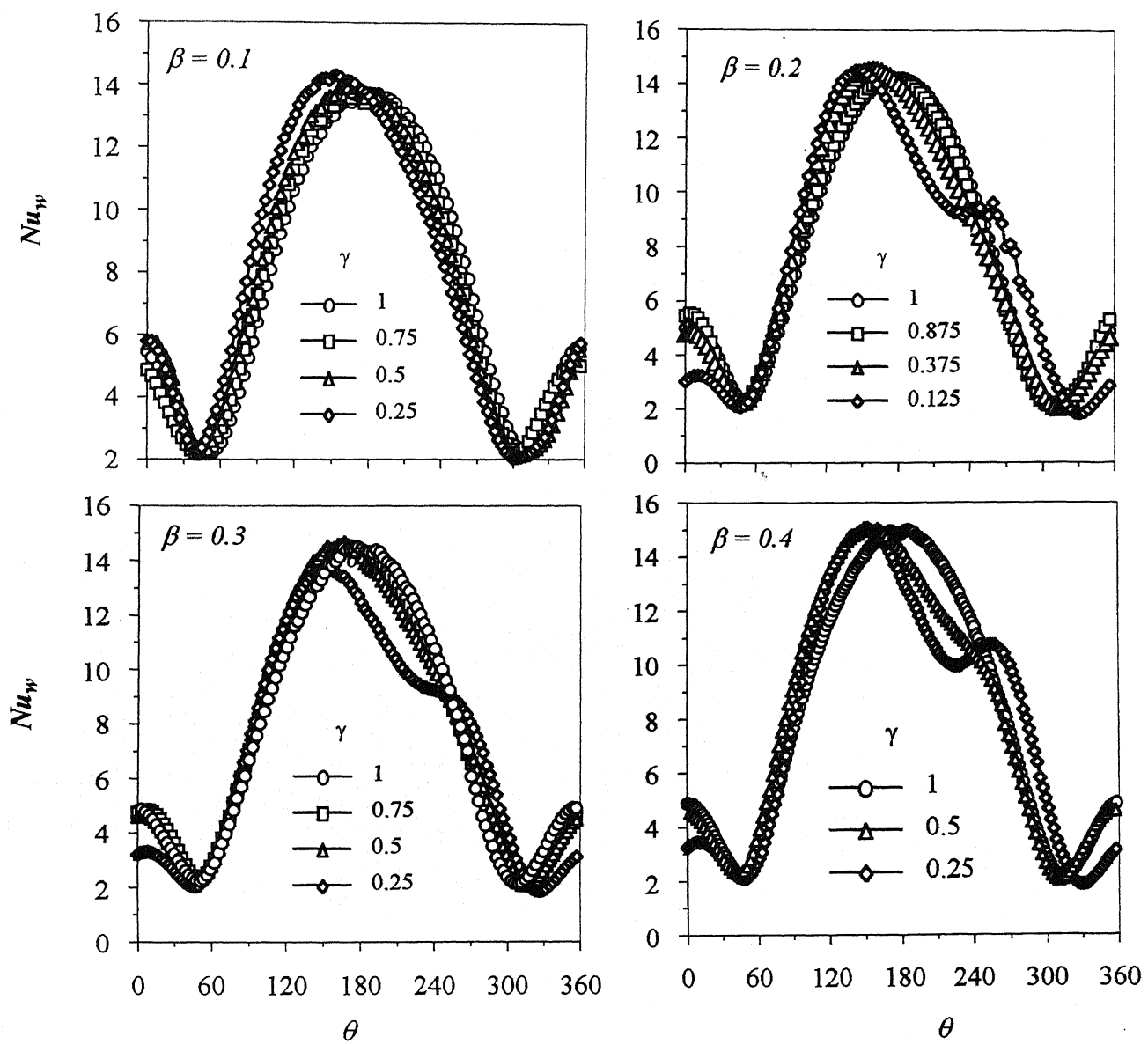
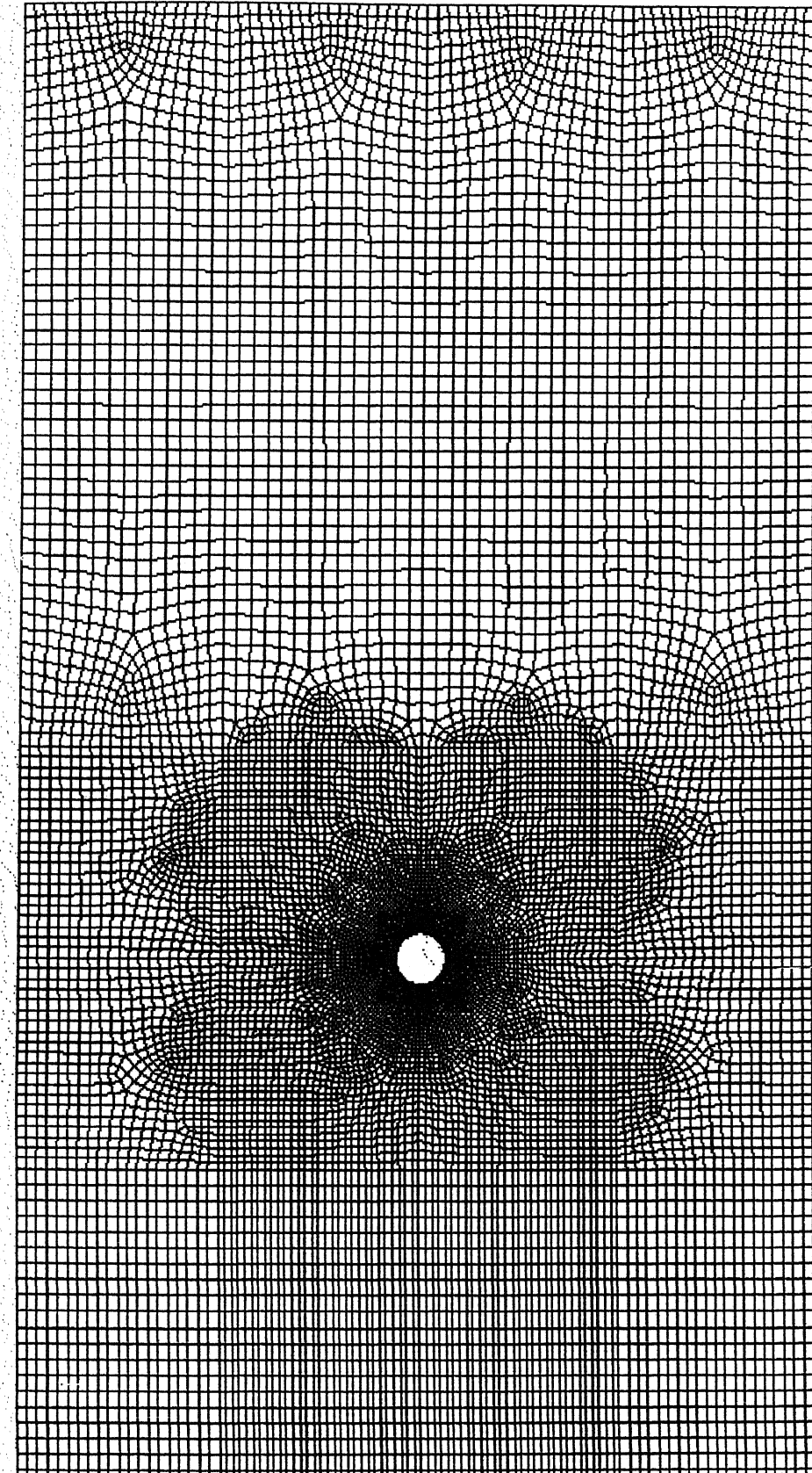


Figure 6.32:  $\overline{Nu}_w$  vs  $Re$  ( $Pr = 0.7441$ ) as a function of  $\beta$  and  $\gamma$



**Figure 6.33: Variation of local  $Nu_w$  plots over the surface of the cylinder as a function of  $\beta$  and  $\gamma$   
 (  $\theta = 0$  is rear stagnation point and  $\theta = 180$  is front stagnation point)**



Grid

101

FLUENT 6.1 (3d, dp, segregated, lam)  
May 02, 2005

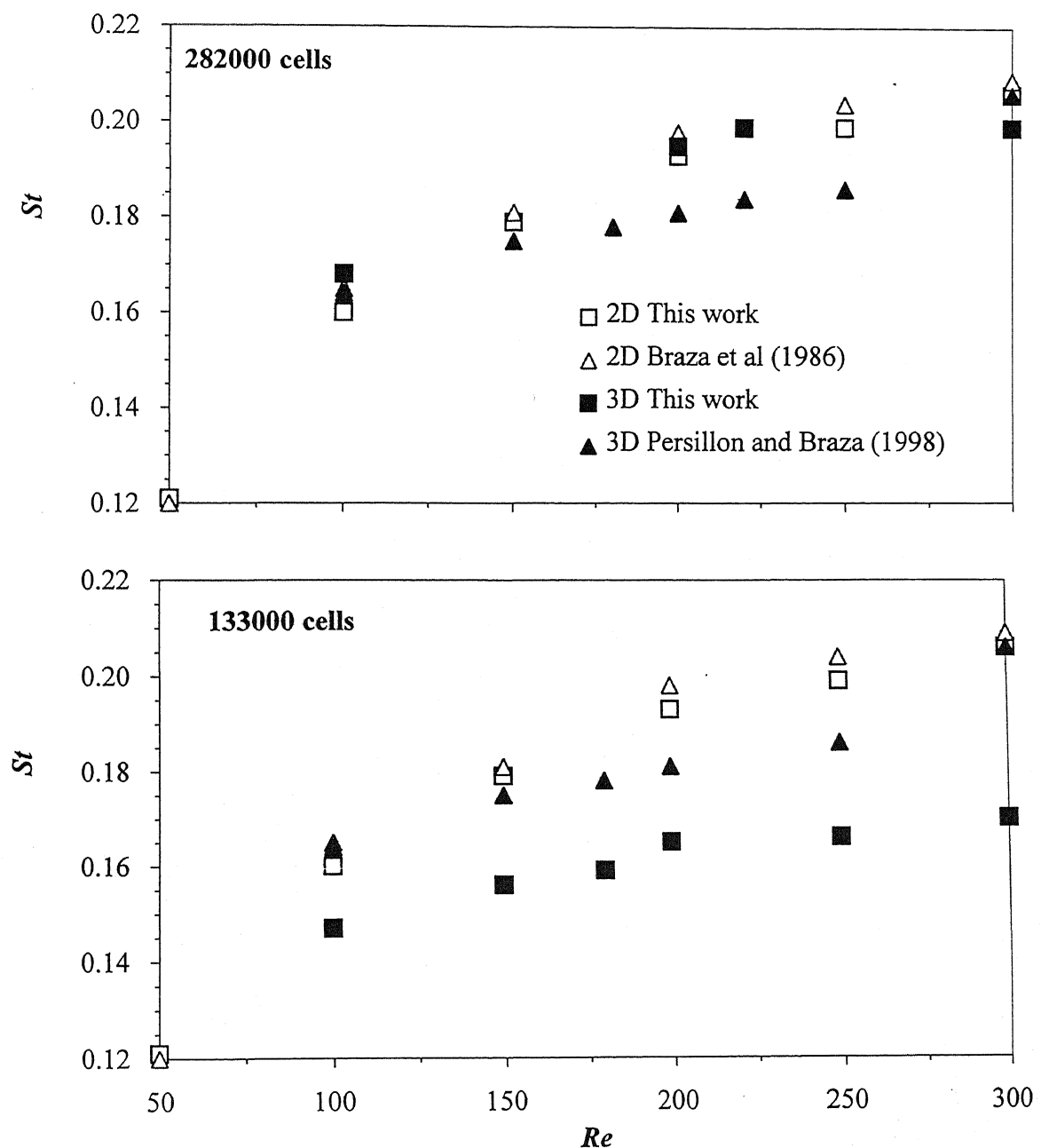
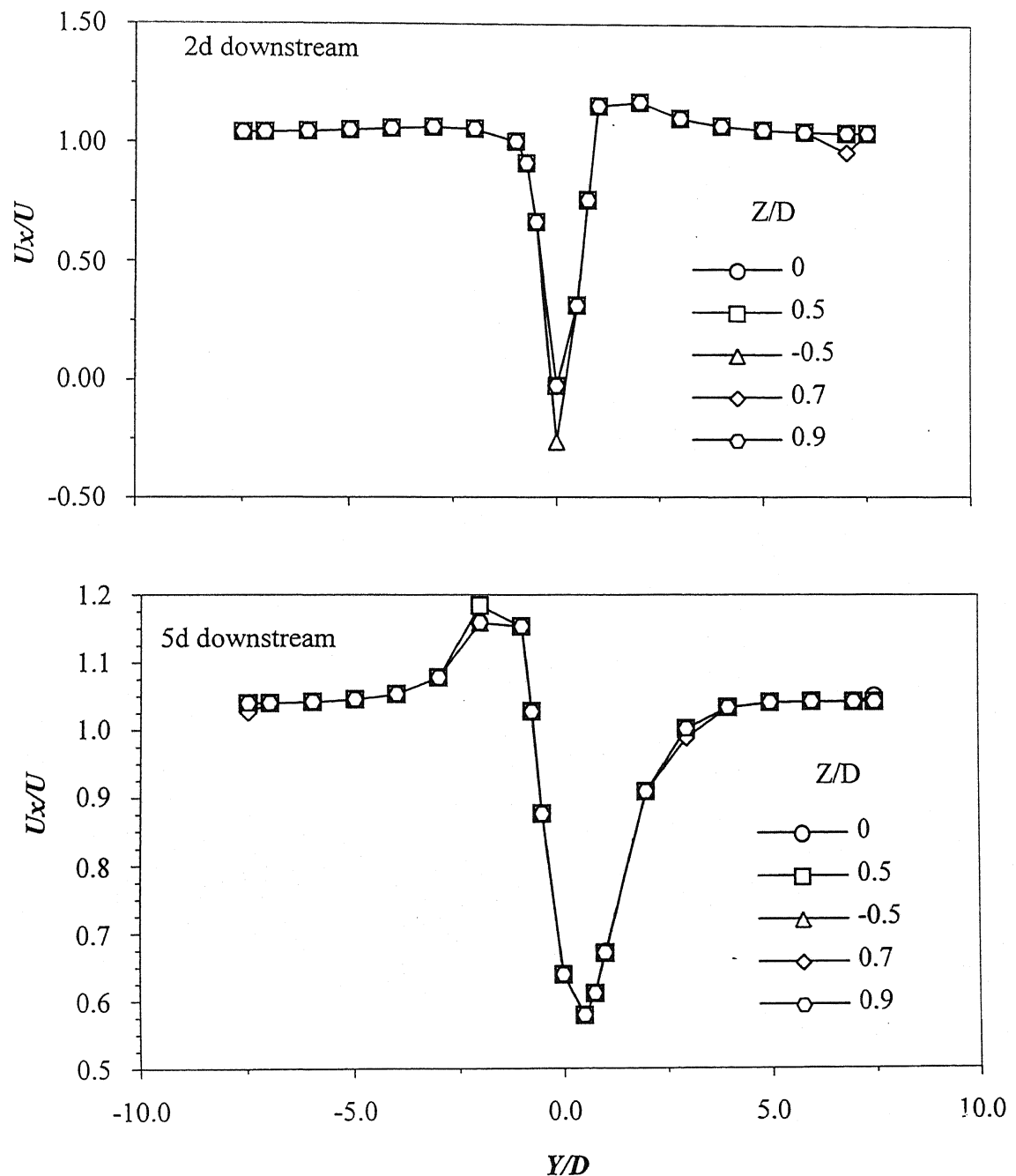
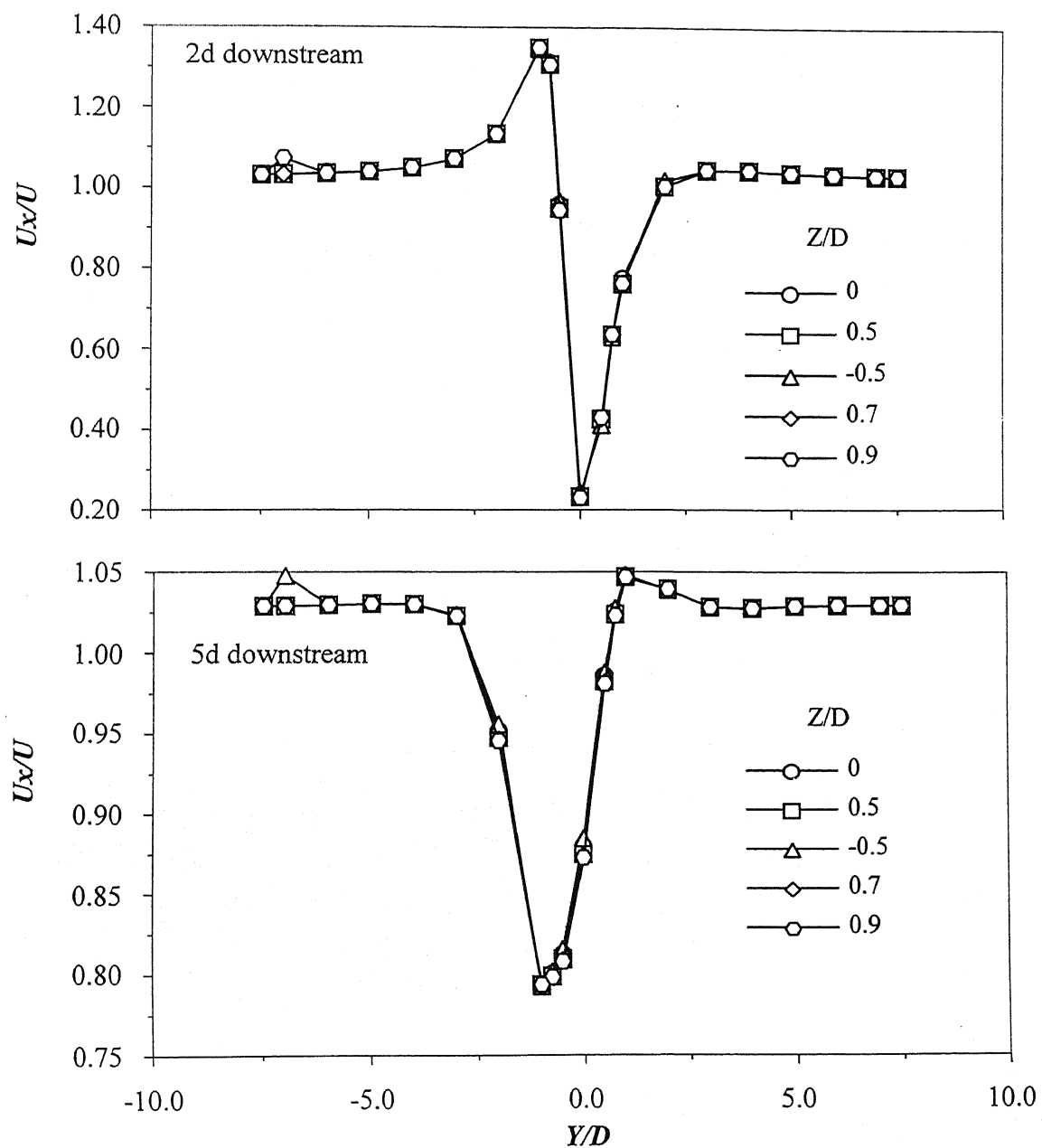


Figure 6.35: St-Re curves for 2-D and 3-D simulations



**Figure 6.36: Normalized velocity profiles at  $Re = 100$  along the span of the cylinder at  $2d$ ,  $5d$  downstream locations**



**Figure 6.37: Normalized velocity profiles at  $Re = 200$  along the span of the cylinder at  $2d$ ,  $5d$  downstream locations**

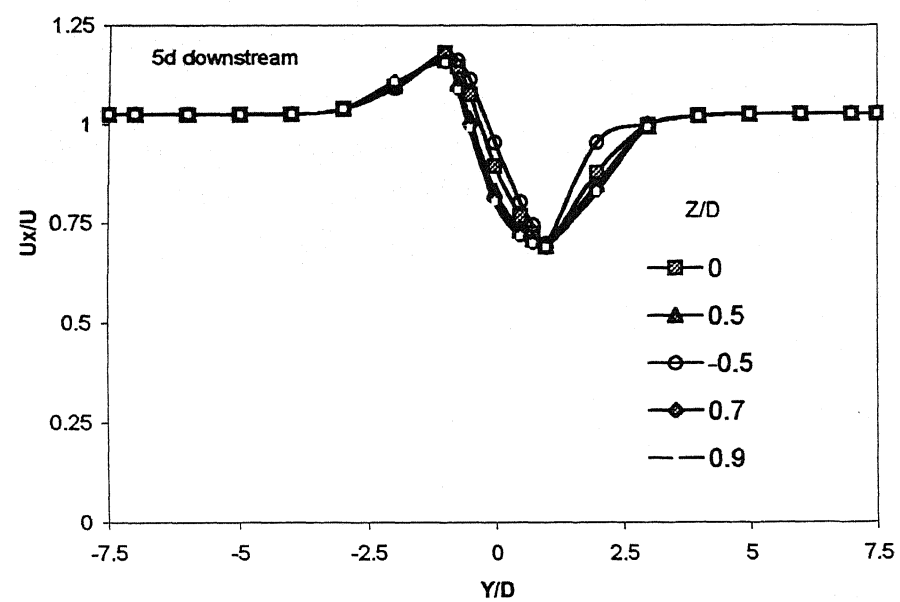
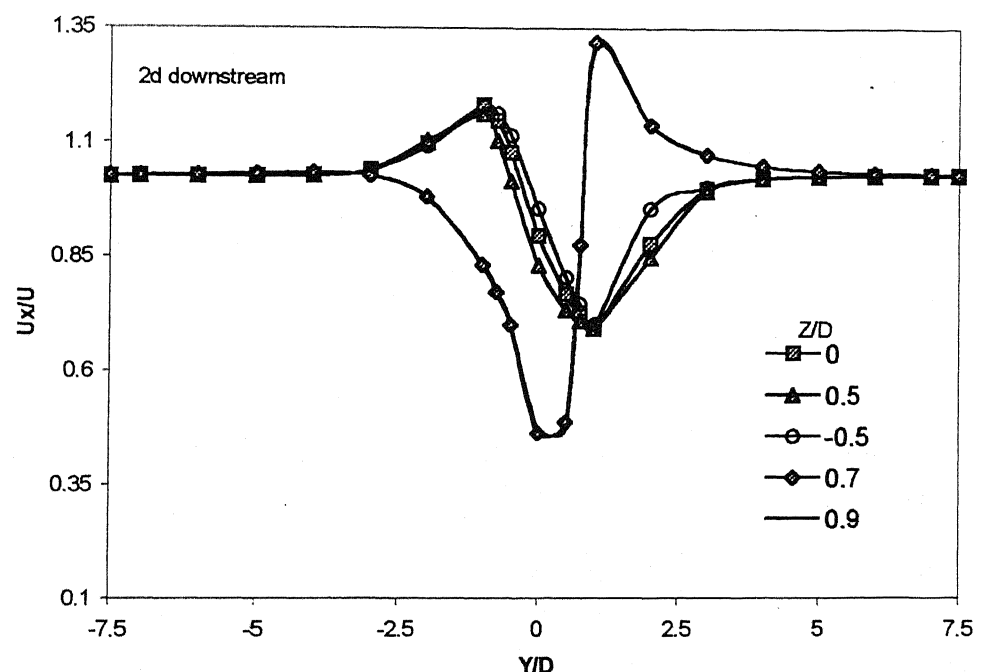


**Figure 6.38: Normalized velocity plots at  $Re = 300$  along the span of the cylinder at  $2d$ ,  $5d$  downstream locations**

## CHAPTER 7

### CONCLUSIONS AND SCOPE FOR THE FUTURE STUDY

#### 7.1 Conclusions

The 2-D unsteady momentum and heat transfer from an asymmetrically confined circular cylinder in a plane channel was studied numerically. In addition, 3-D unsteady flow past a circular cylinder in unbounded domain was studied to characterize three-dimensional transition in the wake of the circular cylinder. The equations of continuity, momentum and energy equations were solved using FLUENT, a flow modeling software that uses a finite volume based numerical method. First, the numerical simulations were carried out for flow past a circular cylinder in unbounded domain in steady and unsteady flow range and the simulation results were compared with the published work. In particular, the transition of the flow from steady to unsteady is studied with the aid of various momentum upwinding schemes available in FLUENT. The global parameters like;  $\bar{C}_D$ ,  $\bar{Nu}_w$  and  $St$  obtained using various upwinding schemes were compared. Simulations were also carried out for the flow past a symmetrically confined cylinder in a plane channel. In the case of cylinder confined symmetrically in a plane channel the transition of flow from steady to unsteady was studied. The critical  $Re$  at the flow transition takes place was determined for various blockage ratios ( $0.1 < \beta < 0.4$ ). The results were compared with the published work and were found to be in good agreement.

The simulations were then extended to study the momentum and heat transfer from an asymmetrically confined circular cylinder in a plane channel in the range of  $Re$  from 10 to 1000 and  $0.1 < \beta < 0.4$ . In this case, the transition of flow from steady to unsteady is determined as a function of  $\beta$  and  $\gamma$ . The effect of  $\beta$  and  $\gamma$  on  $\bar{C}_D$ ,  $\bar{Nu}_w$  and  $St$  is studied. It is observed that for a symmetrically confined cylinder the critical  $Re$  increased with increase in  $\beta$ . For fixed  $Re$ ,  $\bar{C}_D$  and  $St$  increased with increase in  $\beta$ . The effect of  $\beta$  on  $\bar{Nu}_w$  was found to be negligible for  $\beta < 0.3$ . For a cylinder confined asymmetrically in a plane channel, the critical  $Re$  at which the flow transition takes place was found to increase with decrease in gap ratio ( $\gamma$ ), for fixed  $\beta$ , i.e. the vortex shedding from the cylinder is suppressed as the cylinder approaches one of the confining walls.

The critical  $Re$  was also found to increase with increase in  $\beta$  for fixed  $\gamma$ . For fixed  $Re$ ,  $\bar{C}_D$  was found to increase with decrease in  $\gamma$  i.e. the drag force exerted on the cylinder increases as the cylinder approaches closer to the wall. The increase in drag coefficient was more pronounced at low  $Re$ .  $St$  was found to increase with increase in  $Re$  for fixed  $\beta$  and  $\gamma$ . It was also found that, for fixed  $Re$   $St$  increases with decrease in  $\gamma$ . When the cylinder is confined symmetrically in a plane channel, the structure of vortices shed from the cylinder is well defined with double row of vortices placed regularly. The double row becomes a single row of vortices that are shed from the top of the cylinder as the vortex shedding from the bottom of the cylinder is suppressed due to the interference of the vortices shed from the bottom wall. The vortex shedding from the cylinder is completely suppressed when the cylinder is present very close to the cylinder. For fixed  $Re$ , the amplitude of the oscillations in the lift coefficient decreases as  $\beta$  increases. For fixed  $Re$  and  $\beta$ , the oscillation in the lift coefficient increases in the negative direction as  $\gamma$  decreases. The trend is reversed when the cylinder is present sufficiently close to the cylinder i.e.  $\bar{C}_L$  is positive when the cylinder is present very close to the cylinder. The effect of decrease in  $\gamma$  on  $\bar{Nu}_w$  was found to be negligible for all blockage ratios. However, some distortion was found in the distribution of local  $Nu_w$  on the surface of the cylinder as the cylinder moves closer to the wall.

### 7.1 Scope for the future study

- (i) The present study was carried out assuming laminar flow conditions. However, turbulent flow may also be simulated for high range of  $Re$ .
- (ii) In the case of flow past an asymmetrically confined cylinder, constant wall temperature boundary condition was assumed. Constant wall flux boundary may be used to find the effect of asymmetry on the heat transfer from the cylinder.
- (iii) In the present work, an incompressible Newtonian fluid was considered. Therefore, the simulations may be carried out using non-Newtonian fluid as well.
- (iv) In the present work, cross flow situation was considered. This may be extended to parallel flow past a cylinder in unbounded and bounded domains.

## References:

- [1]. Thom, A., *Proc. Roy. Soc (London) A* **141** (1933) 651.
- [2]. Kawaguti, M., Numerical simulation of the Navier-Stokes equations for the flow around a circular cylinder at Reynolds number 40, *J. Phys. Soc. Jpn.* **8** (1953) 747.
- [3]. Apelt, C. J., A. R. C. Tech. Rep., R. & M. No.3175 (1961).
- [4]. Payne, R.B., Calculations of unsteady viscous flow past a circular cylinder, *J. Fluid Mech.*, **4** (1958) 81.
- [5]. Ingham, D. B., Note on the numerical solution for unsteady viscous flow past a circular cylinder, *J. Fluid Mech.*, **31** (1968) 815.
- [6] Kawaguti, M. and Jain, P., Numerical study of a viscous fluid flow past a circular cylinder, *J. Phys. Soc. Jpn.* **21** (1966) 2055
- [7]. Hamielec, A. E. and Raal, J. D., Numerical studies of viscous flow around cylinders, *Phys. Fluids*, **12** (1969) 11.
- [8]. Thoman, D. C. and Szewczyk, A. A., Time dependent viscous flow over a circular cylinder. *Phy. Fluids Suppl.* **II** (1969) 76.
- [9]. Takami, H. and Keller, H. B., Steady two-dimensional viscous flow of an incompressible fluid past a circular cylinder, *Phy. Fluids Suppl.* **II** (1969) 51
- [10]. Imai, I., On the asymptotic behavior of viscous fluid at a great distance from cylindrical body, with special reference to Filon's paradox. *Proc. Roy. Soc A* **208** (1951) 487
- [11]. Dennis S. C. R. and Chang G. Z., Numerical solutions for steady flow past a circular cylinder at Reynolds numbers up to 100. *J. Fluid Mech.*, **42** (1970) 471.
- [12]. Fornberg, Bengt., A numerical study of steady viscous flow past a circular cylinder. *J. Fluid Mech.*, **98** (1980) 819.
- [13]. D' Alessio, S. J. D. and Dennis S. C. R., A vorticity model for viscous flow past a circular cylinder. *Computer Fluids*, **23** (1994) 279
- [14]. Coutanceau, M. and Bourd, R., Experimental determination of the main features of the viscous flow in the wake of a circular cylinder in uniform translation. Part 1. Steady flow. *J. Fluid Mech.*, **79**(1977) 231.
- [15]. Collins, W. M. and Dennis S. C. R., Flow past an impulsively started circular cylinder. *J. Fluid Mech.*, **60** (1973) 105.

[16]. Patel, V. A., Time-dependent solutions of the viscous incompressible flow past a circular cylinder by the method of series truncation. *Computers and fluids.*, 4 (1976) 13.

[17]. Braza, M., Chasaing, P., and Ha Minh. H., Numerical study and physical analysis of the pressure and velocity fields in the near wake of a circular cylinder., *J. Fluid Mech.*, 165 (1986) 79.

[18]. Jackson, J. P., A finite-element study of the onset of vortex shedding in flow past variously shaped bodies. *J. Fluid Mech.*, 182 (1987) 23.

[19]. Mathis, C., Provansal, M., and Boyer, L., The Benard-von Karman instability: an experimental study near the threshold. *J. Phys. Paris lett.* 45 (1984) 483.

[20]. Nishioka, M. and Sato, H., Measurements of velocity distribution in the wake of a circular cylinder at low Reynolds numbers. *J. Fluid Mech.*, 65 (1974) 97.

[21]. Gresho, P. M., Chan, S. T., Lee, R. L. and Upson, C. D., A modified finite element method for solving the time dependent incompressible Navier-Stokes equations. Part 2 Applications. *Intl J. Numer. Meth. Fluids.* 4 (1984) 619.

[22]. Franke, R., Rodi, W., and Schonug, B., Numerical calculation of laminar vortex shedding flow past cylinders, *J. Wind Eng. Ind. Aero.*, 35 (1990) 237.

[23]. Chen, J. H., Pritchard, W. G., S. J. Tavener, S. J., Bifurcation of flow past a cylinder between parallel plates, *J. Fluid Mech.*, 284 (1995) 23.

[24]. Zavotto, L., and Pedrizzetti., G. Flow about a circular cylinder between parallel walls, *J. Fluid Mech.*, 440(2001) 1.

[25]. Dennis, S.C.R., Hudson J.D., Smith, N., Steady laminar forced convection from a circular cylinder at low Reynolds numbers. *Phys. Fluids* 11 (1968) 933.

[26]. Collis, D.C., Williams, M.J., Two-dimensional convection from heated wires at low Reynolds numbers. *J. Fluid Mech.* 6 (1959) 357

[27]. Hsichin M. Hua, Paul S.Lykoudis., Heat transfer from a constant temperature circular cylinder in cross flow. *Int. J. Heat Mass Transfer.* 19 (1976) 698.

[28]. J. Cole and A. Roshko., In *Proceedings of Heat Transfer and Fluid Mechanics Institute* (Stanford University Press, Stanford, California), (1954) P.13

[29]. George Em Karniadakis., Numerical simulation of forced convection heat transfer from a cylinder in cross flow. *Int. J. Heat Mass Transfer.* 31 (1988) 107.

[30]. Figueiredo, A.R., Viegas, D.X., External forced convection around a circular cylinder near a plane boundary. *Int. J. Heat Mass Transfer.* 31 (1988) 47.

[31]. Shin-H.K., Ki-H.K., Sangken K., A unified correlation for laminar convective heat transfer from hot and cold circular cylinders in a uniform airflow.  
*Int. J. Heat Mass Transfer.* **38** (1995) 752.

[32]. C.F Lange, F. Durst, M. Breuer., Momentum and heat transfer from cylinders in laminar flow at  $10^4 \leq Re \leq 200$ , *Int. J. Heat Mass Transfer.* **41**(1998) 3409. .

[33]. J. -M. Shi, D. Gerlach, M. Breuer., G. Biswas, F. Durst, Heating effect on steady and unsteady horizontal laminar flow of air past a circular cylinder. *Phys. Fluids* **16** (2004), 4331.

[34]. C.F Lange, F. Durst, M. Breuer., Wall effects on heat losses from hot wires, *Int. J. Heat Fluid Flow.* **20** (1999) 34.

[35]. J. -M. Shi, M. Breuer, F. Durst., Wall effect on heat transfer from a micro cylinder in near wall shear flow, *Int. J. Heat Mass Transfer.* **45** (2002) 1309.

[36]. Hajime Nalamura, Tamotsu Igarashi., Variation of Nusselt number with flow regimes behind a circular cylinder for Reynolds numbers from 70 to 30000. *Int. J. Heat Mass Transfer.* **47** (2004) 5169.

[37]. S.Santjai, R.J. Goldstein., Forced convection heat transfer from a circular cylinder in a cross flow to air and liquids. *Int. J. Heat Mass Transfer.* **47** (2004) 4795.

[38]. G. Refai Ahmed and M. M. Yovanovich., Analytical method for forced convection from flat plates, circular cylinders, and spheres. *Journal of Thermophysics and Heat transfer.* **9** (1995) 516.

[39]. W. A. Khan, J. R. Culham, and M. M. Yovanovich., Fluid flow and heat transfer from a cylinder between parallel planes, *Journal of Thermophysics and Heat transfer.* **18** (2004) 395.

[40]. Ronald D. Henderson., Details of the drag curve near the onset of vortex shedding. *Phys. Fluids* **7** (1995) 2102

[41]. Huang, P. Y and J. Feng., Wall effects on the flow of viscoelastic fluids around a circular cylinder. *J. Non-Newtonian Fluid Mech.* **60** (1995) 179.

[42]. Sucker, D. und Brauer, H., Fluideodynamik bei quer angestromten Zylindern, *Wärme und Stoffübertragung.* **8** (1975) 149

[43]. Saiki, E.M. and Birngen, S., Numerical simulation of a cylinder in uniform flow: Application of a virtual boundary method. *J. Compt. Phys.* **123** (1996) 450.

[44]. R. Clift, J. Grace, M.E. Weber, *Bubbles, Drops and Particles*, (Academic

Press, New York, 1978). P.154.

- [45]. A. Rosko., NACA Technical Note. 1953, P.2913
- [46]. Berger, E and Wille, R., *Annu. Rev. Fluid Mech.* **49** (1972) 313.
- [47]. Kim, J. Kim, D. Choi, H., An immersed boundary finite-volume method for simulation of flow in complex geometries. *J. Compt. Phys.* **171** (2001) 132.
- [48]. Wandeley, J. B. and Levi, C. A., Validation of a finite difference method for the simulation of vortex induced vibration on a circular cylinder. *Ocean. Engg.* **29** (2002) 445.
- [49]. Rengel, J. E. and Sphaier, S. H., A projection method for unsteady N-S equations with finite volume method and collocated grid. *Hybrid methods in Heat and Mass transfer.* **1** (1998) 4.
- [50]. Williamson, C. H. K., Defining a universal and continuous Strouhal-Reynolds number relationship for the laminar vortex shedding of a circular cylinder *Phys. Fluids* **31** (1988), 2742.
- [51]. Williamson, C. H. K., The existence of two stages in the transition to three-dimensionality of a cylinder wake, *Phys. Fluids* **31** (1988), 3165.
- [53]. Prasad, A. and Williamson, C. H. K., Three-dimensional effects in turbulent bluff-body wakes, *J. Fluid Mech.* **343** (1997) 235.
- [54]. Persillon, H. and Braza, M., Physical analysis of the transition to turbulence in the wake of a circular cylinder by three-dimensional Navier-Stokes simulation. *J. Fluid Mech.* **365** (1998) 23.
- [55]. Jyoti Chakraborty, Nishith Verma and R. P. Chhabra, Wall effects in flow past a circular cylinder in a plane channel: a numerical study. *Chemical Engineering and Processing*, **43** (2004) 1529.

## APPENDIX

This section presents the procedural steps needed to be followed in order to solve a particular type of flow problem using the flow modeling software, **FLUENT**.

1. In a UNIX environment, one has to type **gambit**, followed by a session name (for example **model1**) in the console panel. Then **GAMBIT** is opened and **model1** is started.
2. The desired geometry (2D or 3D) is created using face/volume creation panel.
3. The flow domain consisting of that particular geometry is now required to be meshed. A 2D geometry can be meshed using triangular or quadrilateral elements. However, for a 3D geometry, meshing can be achieved by using hexahedral, wedge-shaped or tetrahedral elements. It may be pointed out that each element in **GAMBIT** is associated with a set of *type* options. **Map**, **submap**, and **pave** are a few examples of available *type* options. For example, meshing with triangular elements can be achieved by the *type* **pave**, which allows for unstructured meshing throughout the domain.
4. Once the meshing is completed, proper boundaries are to be specified from the boundaries specification panel for each edge/face; and continuum type (fluid or solid) is also specified for face (2D) or volume (3D).
5. Then the existing file is saved as a mesh file using **File/Save...** menu item.
6. This saved file is then exported to **FLUENT** using **File/Export...** option.
7. Afterwards **FLUENT** is opened by typing **fluent** in the console panel. In the fluent panel proper solver version (2D or 3D etc.) has to be specified in the command line. Then from the **File/Read...** menu the saved mesh file is being read.
8. At this point it is necessary to check the grid from **Grid/Check...** option. An error occurs for an improper or incomplete meshing. In such a situation the grid check fails.
9. **Fluent** provides three different solver formulations: (i) segregated, (ii) coupled implicit, and (iii) coupled explicit. From **Define/Model/Solver...** panel a suitable solver formulation is selected. From the same panel steady or unsteady condition is selected considering the time-dependence of the problem to be solved.
10. The **Define/Materials...** panel is then opened and properties of the chosen material are inserted manually or selected from the materials drop-down list.

11. Afterwards the reference values panel is opened from the Define/Reference Values...item and the reference pressure location is selected. If gravity is important in the problem, the magnitude and direction of the gravitational acceleration are being inserted into this panel.
12. The specification of boundary conditions remains a very important aspect in the simulation studies. From the Define/Boundary Conditions...panel, proper boundary types are selected and corresponding boundary conditions are being set.
13. Now, from the Solve/Controls/Solutions...panel, proper discretization schemes for pressure, pressure-velocity coupling and momentum are selected and under-relaxation factors are adjusted.
14. At this point the convergence criteria for the residuals of momentum and velocity components (for isothermal and laminar flow situations) are set using the Solve/Monitors/Residual...panel. The plot option is also activated in order for the convergence history to be visible while iterations are going on.
15. Then it is necessary to store all the input parameters in a case file (for example modell.cas) in order for the information to be available in a next **FLUENT** session. It is done from the File/Write/Case...menu item.
16. The solution initialization is another important step that is to be completed before start of the iterations. This initialization is achieved from the Solve/Initialization...panel where one can retain default values for velocity and pressure (which are zero) or select a zone from the Compute From...drop down list; and can specify the values of the pertinent variables.
17. From the Solve/Iterate... panel the computations are now started by specifying the number of iterations and clicking on Iterate. However, if unsteady problem is to be solved then in the iterate panel another two important parameters need to be specified also. These are the time step size and the number of time steps. Here, instead of mentioning the number of iterations, one has to input the maximum number of iterations per time step.
18. When the computations are being carried out, the values of the residuals of momentum and velocity components are observed to decrease if all the input parameters are set properly and a realistic model being chosen. The iterations are

observed to converge after a certain time when the convergence criteria are being satisfied.

19. After convergence is achieved, it is necessary to save the information for further processing. This is achieved by File/Write/Data...option and the data file named model1.dat is being created.

20. The converged solution enables one to obtain the values of many important parameters and produce graphical representations of various functions.

21. As a representative case one might compute the value of the total drag coefficient,  $C_D$ , which is an important engineering parameter in the study of flow past submerged objects. This can be achieved from the Report/Reference Values...panel where one has to specify the velocity, density and the projected area for the computation of  $C_D$ . Now the Report/Forces...panel is to be opened and the proper zones are to be selected. Afterwards clicking on the Compute...button will give the drag force components and the drag coefficient.

22. It is also important to study the vectors of velocity, contours of stream function, etc., to properly understand the flow behavior. This can be achieved from the Display/Velocity Vectors...or Display/Contours...panel, respectively. The surface vorticity is another important parameter, which helps to compute the angle of separation (the angle at which the flow separation occurs from the surface of any submerged object). This can be achieved from the XY Plot...option where the surface vorticity may be plotted as a function of curve length.

The above section briefly discussed several steps which are to be followed to simulate a standard problem of fluid dynamics using a very sophisticated flow modeling software, **FLUENT**. The readers are requested to consult the manuals for a better understanding of different features available in this package